Phenomenology of QCD and electroweak processes

Ahmed Cassim Bawa

Phenomenology of QCD and Electroweak Processes

Ahmed Cassim Bawa

October 1989

A thesis submitted for the degree of Doctor of Philosophy
in the Department of Physics,
University of Durham.

CONTENTS

Abstract i

Acknowledgements ii

Chapter 1. Introduction: The Standard Model, Beyond the Standard Model and Collider Physics 1

Chapter 2. W,Z Production at Large Transverse Momentum at $p\bar{p}$ colliders.

2.1 Introduction 7

2.2 Factorisation and Structure Function Definitions 9

2.3 Notation and Matrix Elements 25

2.4 Kinematics and Integration Techniques 38

2.5 The MRS Structure Functions 41

2.6 'Optimisation' Procedures with respect to the Choice of Scales 42

2.7 Numerical Calculations - nonsinglet $O(\alpha_s^2)$ calculation 46

2.8 Numerical Calculations - complete $O(\alpha_s^2)$ calculation 54

2.9 Conclusions 65

Chapter 3. A study of the Equivalent Photon Approximation at HERA

3.1 Introduction 71

3.2 Derivation of the Electron Structure Function 74

3.3 The Helicity Amplitude Calculation 78

3.4 The Phase Space Integrals 84

3.5 Calculations and Comparisons 89

3.6 Conclusions 96

Chapter 4. Photoproduction of Large Transverse Momentum Photons at HERA.

4.1 Introduction 100

4.2 The Photon Structure Function 105

4.3 The Kinematics 107

4.4 The Matrix Elements 114

4.5 The Numerical Results 121

4.6 Conclusions 128

Chapter 5. Production of Charged Higgs Bosons at the Tevatron and SSC.

5.1 Introduction 132

5.2 The Non-minimal Higgs Model 134

5.3 The Process $A + B \rightarrow H^{\pm} + X$ 140

5.4 The Generic Process: $g + b \rightarrow t + \bar{t} + b$ 147

5.5 Conclusions 158

ABSTRACT

A phenomenological study is made of several aspects of the standard model (and beyond) in the context of collider physics. These calculations are performed in the framework of Quantum Chromodynamics (QCD) and the standard Electroweak theory in an attempt to understand the underlying gauge theory more fully.

In chapter 2, a precision QCD and electroweak calculation is performed to predict the high transverse-momentum distribution of the intermediate vector bosons produced in $p\bar{p}$ collisions. Calculated cross-sections are compared with data from the CERN collider and predictions are made for the Tevatron, LHC and SSC. Theoretical uncertainties, due to scale and structure function ambiguities, are estimated.

In chapter 3, the equivalent photon approximation (or EPA) is studied at high energies to determine the accuracy of the approximation. An exact calculation of the process $e + q \rightarrow e + q + \gamma$ is performed and compared with an approximate calculation of the process $\gamma + q \rightarrow \gamma + q$, where the initial-state photon is produced (using the EPA) from an initial-state electron. The test is carried out for the cases where the final-state electron are tagged and untagged. At high energies, the approximation is accurate to within 10%.

In chapter 4, deep inelastic Compton scattering is investigated at energies of the HERA *ep* collider. A study of the production rate is made to determine the feasibility of measurement at HERA and it is clear that for $p_T^\gamma < 50\ GeV/c$ the cross-section will be measurable. In addition, studies are made to determine the efficiency of this process as a probe of the proton structure functions. The cross-section is only weakly dependent on the structure functions.

In chapter 5, the production of charged Higgs scalars is considered at hadron colliders. The fully inclusive cross-section for charged Higgs scalars is calculated and compared with the associated W boson cross-section. The generic process $g + b \rightarrow b + t + \bar{t}$, which may proceed through an intermediate charged Higgs (or W) or through QCD processes, is studied and the Higgs cross-sections are compared with the W and QCD cross-sections.

ACKNOWLEDGEMENTS

The progress that I made in the last three years towards this Doctor of Philosophy degree would have been impossible without the help, encouragement and dedication of several people whom I hold in great respect and affection. The pleasure of working in such a warm and wholesome environment made for a wonderful experience in Physics and in human interaction.

To my supervisor, Dr James Stirling, I will always be indebted for his excellent supervision and for his constant trust and belief in me. I arrived here in the United Kingdom with very little knowledge of this subject and he, very patiently, guided me through the research and computing. He was happy to allow me to work with other senior physicists with whom he collaborates and this was much appreciated. His concern for the well-being of our family will be greatly appreciated.

I am grateful to the other members of the group for the stimulating and vibrant atmosphere. I felt comfortable in turning to Professor Alan Martin, Dr Peter Collins, Dr Chris Maxwell, Dr Mike Pennington and Dr Mike Whalley for help. I appreciate the embarassingly large number of reference letters written on my behalf by Alan Martin, Mike Pennington and James Stirling. I must also thank Phillip Tuckey, Cho Ng, Frank Cuypers and Choong-Sun Kim for fruitful discussions. To Iain Maclaren, I offer my continued friendship. It was a wonderful pleasure spending many hours in discussion about the role that we could play in society.

To the student members of the group, I extend my warmest affection and gratitude. To my room-mates, Jenny Nicholls, David Pentney and Peter Harriman I owe special thanks. I am extremely grateful to David Pentney, Peter Harriman and Mike Wade for suffering through a reading of this thesis and to Nick Brown, Yanos Michopolous, Simon Webb, Mohamed Gomshy-Nobarry, Muhammed Hussein, Dominic Walsh, Duncan Curtis, Paul Murphy and Neil Shaban, all of whom played a part in providing a wonderful atmosphere.

None of this research would have been possible without the financial support that I received from several sources. I am greatly indebted to the World University Service (U.K.) for making the study possible in the first place. After the first year we were supported by the United Nations Education and Training Programme for Southern Africa and I hope that on my return to South Africa I will be able to fulfil the expectations that these two organisations have of me. We were fortunate to receive some help from the Foundation for Research Development and this helped us tremendously.

To my parents and extended family, I am grateful for an unswerving committment to my education amidst tremendous financial and social turmoil. My parents have constantly placed the education of their children above all else and to them I owe my love for knowledge. All parents should be like them.

To Rookaya and our daughters, Nadya and Mishal, no gratitude will suffice. They have always been patient and supportive. Rookaya is constantly the pillar around which this family hangs and never once has that pillar shaken. Her dedication to the family goes well beyond the call of duty and it is impossible to describe my appreciation.

And finally it is to the people of South Africa that I dedicate this work and all the work that flows from it. My perceptions of society and of social change, and of my role in society are shaped by the courage and commitment of the people in their struggle for new and democratic South Africa.

1. Introduction: The Standard Model, Beyond the Standard Model and Collider Physics

The standard model of particle physics, which describes the fundamental constituents of nature and the interactions between them, is both simple and beautiful. This model provides us with a framework within which the universe may be understood, though at the present time this understanding can in no way be deemed complete. The strength of this model is that it provides a deep and consistent phenomenological probe of our present ideas, leading to an increased sophistication of our knowledge of the universe.

In the present model, all matter comprises of two types of particles, quarks and leptons. Both of these are point-like and have spin-1/2. There are four known interactions between these fundamental particles: the weak nuclear force, the electromagnetic force, the strong nuclear force and finally, the force of gravity. The last of these is a negligible perturbation at the energies that are presently available to us for investigation. The remaining three interactions are described by gauge theories and are mediated by spin-1 gauge bosons. Quarks experience all three of these interactions while leptons experience only the weak and electromagnetic interactions. Following constraints from charged-current weak interactions, it seems natural to group the quarks and leptons into 3 families: (ν_e, e^-), (ν_μ, μ^-), (ν_τ, τ^-) for the leptons and (u, d'), (c, s') and (t, b') for the quarks. The primes indicate Kobayashi-Maskawa mixing and this phenomenon is absent from the lepton sector because the ν's are presently considered massless. The quarks appear in three different colours, which may be considered the charges of the strong interactions. Of these particles, the top quark, t, has yet to be discovered. Present limits on its mass indicate that it lies in the region $76\ GeV/c^2 \leq m_t \leq 180\ GeV/c^2$.

The weak and electromagnetic interactions are unified [1] partially within the gauge group

$$SU(2)_L \otimes U(1)_Y.$$

To generate large masses for the intermediate vector bosons, this gauge theory

is spontaneously broken - via the Higgs mechanism in the case of the standard model. Whilst this mechanism produces masses for the weak bosons it leaves the photon massless. This unified picture of the electromagnetic and weak nuclear interactions has been very successful in making a connection between theory and experiment. However, it must be said that this unification is incomplete. in that, at presently available energies, the coupling constants for the weak and electromagnetic interactions are different.

The popular theory for strong interactions at the present time is Quantum Chromodynamics [2]. The strong nuclear force is based on an exact local gauge symmetry, $SU(3)_C$ which is a non-Abelian lie group. This strong interaction is mediated by an $SU(3)$ octet of coloured gauge bosons, the so-called gluons. Since this is an exact gauge symmetry the gluons are massless. It is generally believed at the present time (though no rigorous proof exists) that the quarks and gluons are confined within colourless hadrons. This property of QCD means that coloured quarks or gluons are never directly observed in experiments. An important property of non-Abelian gauge theories is that of asymptotic freedom. which implies that quarks behave as free particles at high energies [3].

The successes of the electroweak unification led to an increase in the size of the standard model gauge group to incorporate Quantum Chromodynamics (QCD), which is the only consistent theory (at the present time) for the strong nuclear interaction. This extended gauge group is

$$SU(3)_C \otimes SU(2)_L \otimes U(1)_Y. \tag{1.1}$$

Attempts to unify these three interactions have been made [4] but no entirely satisfactory model has yet been found.

Although the standard model has withstood stringent tests in the past, there is a general consensus that the standard model is a window to some more unifying theory. In addition, the completion of the standard model picture requires the discovery of the masses of the top quark and the Higgs scalar. Of these two the observation of the latter is extremely important, to clarify ideas on how spontaneous symmetry breaking occurs. Indeed this ranks as *the* major project in

particle physics at present. Other problems that must be answered are the fine-tuning problem, the unification problem and the role of gravity. These however, are long term problems. Another indication that our understanding is incomplete has to do with the fact that in the minimal version of the standard model, (with three generations of quarks and leptons and one Higgs doublet) there are 18 arbitrary parameters [5]. Except for the couplings in (1) below, the other arbitrary parameters in the standard model are linked in some way with the Higgs sector and with the mechanism of spontaneous symmetry breaking. Any extension of the minimal standard model increases the number of *a priori* unknown parameters. In a minimal model these parameters are:

(1) The gauge couplings - one for each interaction. (3)

(2) The Higgs sector parameters - m_W and m_H. (2)

(3) Masses in the fermion sector - 6 quarks, 3 leptons. (9)

(4) The Cabbibo-Kobayashi-Maskawa matrix elements for the quark sector. (4)

Several theoretical scenarios have been developed in recent years to overcome some or all of the above problems with the standard model. One common requirement for all of them is that they must reproduce the standard model at energies of the order of the mass of the electroweak intermediate vector bosons. Another feature of these theories is that they all have some new fundamental underlying theory which is valid at some higher energy scale (between 1 TeV and M_{planck}). This means that experimental investigation of these theories must wait at least until the Superconducting Supercollider (SSC) is built.

The dramatic progress made by particle physics in the last 2 or 3 decades has resulted from the building and running of particle accelerators. The progress in accelerator design has resulted in higher energies, higher luminosities and high precision detectors. The challenge that faces experimentalists is to continue this trend. In the last decade or two, the technological leap from the fixed target experiments to the collider experiments led to the discovery of the intermediate vector bosons and a host of other crucial pieces of evidence that make the standard model so successful. LEP, the new electron-positron collider at CERN, is already producing results. The proton-antiproton collider at Fermilab has had

an extremely successful run and results are beginning to surface after analysis. Several other lower energy colliders are presently producing precision data. In the near future, the proposed building of the SSC, LHC (Large Hadron Collider) and UNK (in the Soviet Union) will permit even more exploration.

It seems then that the task that awaits theoretical particle physics is two-fold. On the one hand the availability of new precision data permits more stringent testing of the electroweak theory and of perturbative QCD. In the electroweak sector theorists are presently producing very refined quantitative tests that will be compared with the extremely precise data that will become available from LEP. Hopefully this will help to probe the Higgs sector. In perturbative QCD the theoretical uncertainty in calculations is still large, and it seems that the most precise calculations have a systematic uncertainty of at least 20%. The challenge that faces theorists in this case is to extend the calculations to higher orders in α_s and to pin down the uncertainties in the structure functions of the hadrons and the fragmentation functions. On the other hand, a second task is to extend the standard model in a way that will lead the subject forward but will still allow it to be tested by experiment, either presently or in the near future. An example of this is the minimal extension of the standard model (ie. extending the Higgs sector to two complex doublets), which happens to have the same Higgs structure as the minimal version of supersymmetry. The 1 TeV scale is important in a discussion of this type. If the mass of the Higgs boson is larger than 1 TeV then the weak interactions become strong on the TeV scale. This is the most compelling argument to suggest that some new physics must appear at the TeV scale.

The topics studied in this thesis are all concerned with Collider Physics. In chapter 2, attempts are made to perform precision calculations in perturbative QCD to predict (up to $O(\alpha_s^2)$) the production of the intermediate vector bosons, at large transverse momentum, in hadron colliders. First, it is shown that there is reasonable agreement between theory and experiment at $\sqrt{S} = 630GeV$ and second, predictions are made for the Fermilab collider and the SSC, UNK and LHC. In chapter 3, the equivalent photon approximation is tested for the new e-p collider (HERA) in Hamburg. This test arose out of need, since a significant

fraction of the experiments at HERA will involve almost real photons in the initial channel. Thus HERA can also be considered as a very high energy photon-proton collider. In chapter 3, one such process is considered at HERA. An investigation of deep inelastic Compton scattering is made to determine the size of the expected cross-section and whether this will be a feasible project for the experimentalists. Cross-section measurements of this process can, in principle provide a probe of the hadronic component of the photon. This is a very clean process experimentally, and in fact the only limitations are the statistical errors from the smallness of the cross-sections. Finally in chapter 4, charged Higgs production is considered at the SSC and Tevatron. This is done as part of a larger project which is underway.

REFERENCES

1. S.L. Glashow, Nucl. Phys. **22** (1961) 579; S. Weinberg, Phys. Rev. Lett. **19** (1967) 1264; A. Salam, in Elementary Particle Physics: Relativistic Groups and Analyticity (Nobel Symposium No. 8), edited by N. Svartholm, Almqvist and Wiksell, Stockholm (1968) p. 367.

2. W.A. Bardeen, H. Fritzsch and M. Gell-Mann, in Scale and Conformal Symmetry in Hadron Physics, edited by R. Gatto, Wiley, New York, (1973); D.J. Gross and F. Wilczek, Phys. Rev. **D8** (1973) 3633; S. Weinberg, Phys. Rev. Lett. **31** (1973) 494.

3. D.J. Gross and F. Wilczek, Phys. Rev. Lett. **30** (1973) 1343; H.D. Politzer, Phys. Rev. Lett. **30** (1973) 1346.

4. H. Georgi and S.L. Glashow, Phys. Rev. Lett. **32** (1974) 438; J.C. Pati and A. Salam, Phys. Rev. **D10** (1974) 275.

5. H. Harari, SLAC-PUB-4223, 1987.

2. W,Z Production at Large Transverse Momentum at $p\bar{p}$ Colliders

2.1 Introduction

In the early 1970's, the Drell-Yan process in the parton model [1] was successful in producing descriptions of the invariant mass and longitudinal distributions of large-mass leptonic pairs produced at fixed-target hadronic colliders. However, it was unsuccessful in describing the large tail of the high transverse momentum distributions which were observed experimentally. In the naive parton model, the only source of transverse momentum in the final state is the intrinsic transverse momentum of the partons within the hadrons. Early work on a QCD-improved Drell-Yan process performed by Altarelli *et al.* [2,3], and others [4] suggested that the large tail at high transverse momentum could arise from higher-order processes in Quantum Chromodynamics (or QCD), such as quark-gluon scattering and gluon emission. These calculations were based on the theory developed by Politzer *et al.* [5], Sachrajda *et al.* [6] and Amati *et al.* [7].

The production of the intermediate-mass vector bosons at $p\bar{p}$ colliders tests the Drell-Yan process in the high energy regime. As in the case for large-mass lepton pairs mentioned above, the QCD-improved Drell-Yan process is successful in predicting the total cross-section and the differential cross-section, $d\sigma/dp_T^2$, in the high p_T region for vector boson production as an expansion in α_s, the strong coupling constant. The extension of these theoretical calculations to $O(\alpha_s)$ introduced large corrections to the naive parton model predictions, especially at fixed target energies where it became necessary to employ resummation techniques.

The theoretical prediction of the boson p_T-distribution has a further complication. If the p_T of the boson is $O(m_W)$, then renormalisation group-improved perturbation theory is valid. The large p_T tail of the p_T-distribution is already predicted at the $O(\alpha_s)$ level. However, if $\Lambda_{QCD} \ll p_T \ll m_W$, then a new scale enters the problem and large terms of the form

$$\frac{1}{p_T^2}\alpha_s^{(n)} \ln^{(m)}(\frac{m_W^2}{p_T^2}), \qquad m \leq 2n-1 \tag{2.1}$$

force the consideration of terms to all orders. These terms, which are character-

istic of a theory with massless vector bosons (or gluons), have to be resummed. The large logarithms arise from the emission of soft gluons.

The UA1 and UA2 collaborations at the CERN $Sp\bar{p}S$ Collider have published data on the high transverse momentum distribution of the weak vector bosons produced in $p\bar{p}$ collisions [8,9]. The data is being augmented by recent experimental runs at CERN and at the Tevatron. The availability of this data provides the opportunity to perform theoretical tests of perturbative QCD in the high p_T regime. This is particularly important for positive q^2 processes such as the Drell-Yan process because these have large $O(\alpha_s)$ corrections to the leading order cross-sections. As more data becomes available and as the experiments become more sophisticated the statistical and systematic errors will decrease allowing this process to be used to increase our understanding of α_s, Λ_{QCD}, and the parton distributions of hadrons. Improved data would also permit a general test of the standard model. If the theoretical predictions for these p_T-distributions differ significantly from the experimental curves, this would have to lead to a re-examination of the theory upon which the calculation is based.

The search for as yet outstanding standard model physics and for new physics at the existing colliders and at the proposed colliders and supercolliders depends on a thorough understanding of the background to such processes. For example, one may consider the search for a heavy top quark, with $m_t > m_W + m_b$, which decays by

$$t \to b + W^+ \to b + e^+ + \nu_e. \tag{2.2}$$

This search will require a good knowledge of the vector boson background. Similar considerationsalso apply to 'new physics'. In the minimally-extended standard model, for example, the Higgs sector comprises two complex doublets, instead of one. The phenomenological implication of this expanded Higgs sector is that the spectrum of scalars increases from one to five; two neutral scalar Higgses, a pair of charged scalar Higgses, H^+ and H^-, and a neutral pseudoscalar Higgs. The charged Higgses have identical decay modes to those of the weak vector bosons and any hope of discovering these at the hadron colliders will demand a very sharp analysis of W boson production, from which charged Higgs production will

have to be distinguished.

Discussions of the factorisation theorem and structure function definitions are presented in section 2.2, together with a description of what Ellis *et al.* [10] call the operational procedure. In section 2.3, a review of the matrix element calculations is given. Initially, the calculation was performed with the $O(\alpha_s^2)$ matrix elements of reference [10], which covered only the non-singlet sector. Later, when the full second-order calculation of Arnold and Reno [11] became available, the calculation was repeated to provide a full second-order prediction. In section 2.4, the kinematics and techniques of integration are described. One source of uncertainty in these calculations is the choice of structure functions. A description of the MRS structure functions [12] is presented in section 2.5. Another theoretical uncertainty that appears in QCD calculations is the choice of scales. Two arbitrary scales appear in calculations that involve hadrons. One is related to the choice of renormalisation scheme and the other to the choice of factorisation scheme. In section 2.6 the procedure of 'optimisation' is described, in which some arbitrariness in the choice of the scales is removed. In section 2.7 the theoretical predictions for the production of W and Z bosons at high p_T are presented for the energies at which the CERN collider and the Tevatron operate and at the energies at which UNK, the LHC and the SSC will operate if they are built. In section 2.8, a discussion is presented of the uses of this calculation together with an estimate of the theoretical uncertainty.

2.2 Factorisation, Structure Function Definitions and Operational Procedure

The calculation of higher-order processes in QCD is of paramount importance in determining the validity of perturbative QCD. This is particularly true for interactions such as the Drell-Yan process, which have a large $O(\alpha_s)$ correction to the leading order result. The procedure for calculating these processes is presented here in a very qualitative fashion. The higher-order processes are computed in perturbation theory in the QCD-improved parton model. If a calculation is performed naively in perturbation theory as a perturbation series of

Feynman graphs, it has infrared and mass singularities. Politzer [13] suggested that these divergences could be factored out of the parton cross-section and absorbed into the structure functions via convolution integrals over the x_i. In this prescription the part of the parton cross-section that remains is well-behaved and can be calculated in perturbation theory. The procedure then is completed by convoluting the bare structure functions with the singular factors to produce the dressed structure functions which are finite and physically measurable. Ellis *et al.* [14] show that this separation of infrared and mass divergences occurs to all orders in perturbation theory.

Therefore, there are two ingredients in the calculation of cross-sections of hadronic interactions. First, there is the set of structure functions that describe the momentum distribution of the constituents within the hadrons and the set of fragmentation functions that describe the decay of scattered partons into hadrons. In inclusive processes, such as the present one being studied, it is only the former that is relevant. These ingredients cannot be calculated and have to be extracted from experiment, usually from deep inelastic scattering. Second, there are the matrix elements which are calculated in perturbation theory from the underlying field theory. The inclusive hadronic cross-section is obtained by convoluting the matrix elements with the structure functions, summing over all parton types. The structure functions represent the long-distance aspect of QCD while the hard process cross-section represents the short-distance aspect. This separation of long- and short-range effects survive to all orders in α_s. This is the factorisation theorem.

The parton distribution functions are process independent but enter different processes in specific and well-defined ways. This means that if parton distributions are determined from deep inelastic scattering then the cross-sections for other processes, for instance the Drell-Yan process, can be predicted.

The extraction of structure functions from experiment relies very heavily on data produced in deep inelastic scattering experiments (see figure 2.1). The structure function determination for the Drell-Yan process is somewhat more complicated and the connection between the Drell-Yan and deep inelastic scattering structure functions will be demonstrated below. In the naive parton model

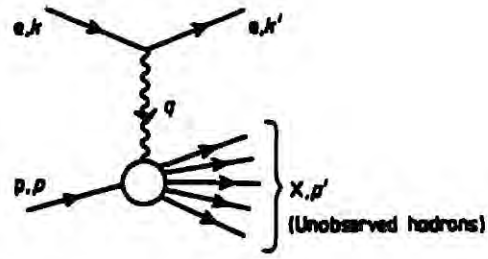

Figure 2.1 Deep inelastic scattering: lepton + proton → lepton + X.

(when terms of the $O(1/Q^2)$ are neglected) a structure function, such as F_1, is defined as a convolution of the probability density of a quark (with momentum fraction y) in a hadron with the pointlike cross-section of the process under investigation. In general

$$2F_1 \sim \int \frac{dy}{y} q_0(y)\hat{\sigma}(yP+q) + O(1/Q^2), \tag{2.3}$$

where P is the momentum of the hadron and q the momentum of the current. The validity of this expression depends on the $1/Q^2$ approximation, in which all terms of $O(k^2/Q^2)$ and $O(k_T^2/Q^2)$ (where $\sqrt{k^2}$ is the virtual mass and k_T is the intrinsic transverse momentum of the quark within a hadron) are neglected. This forces the final-state parton to be quasi-real and collinear. It is clear that in this approximation (2.3) factorises into two real processes, the probability density of finding one given quark in the hadron and the hard-process, pointlike cross-section.

In the deep inelastic limit the structure functions F_1 and F_2 are related to the $\gamma^* p$ cross-sections by the following [15] in the deep inelastic limit,

$$\begin{aligned} 2F_1 &= \frac{\sigma_T}{\sigma_0}, \\ \frac{F_2}{x} &= \frac{\sigma_T + \sigma_L}{\sigma_0}, \end{aligned} \tag{2.4}$$

where σ_T and σ_L are the photon-proton cross-sections for transverse and longi-

tudinal virtual photons respectively. For deep inelastic scattering

$$\sigma_0 = 4\pi^2\alpha/s. \tag{2.5}$$

Explicit expressions for σ_T and σ_L are given in reference [15]. If $x \equiv Q^2/2p.q$ the structure function F_1 may be written in terms of the partonic variables as

$$\begin{aligned} 2F_1 &= \left(\frac{\sigma_T}{\sigma_0}(x,Q^2)\right)_{\gamma^* p} \\ &= \sum_i \int_x^1 \frac{dy}{y} q_{0i}(y)\left(\frac{\hat{\sigma}_T}{\hat{\sigma}_0}(x/y,Q^2)\right)_{\gamma^* i} \end{aligned} \tag{2.6}$$

In (2.6) $\hat{\sigma}_0$, $\hat{\sigma}_T$ and $\hat{\sigma}_L$ are the corresponding $\gamma^* q$ cross-sections.

A useful definition of the structure functions F_1, F_2, and F_3 is [3]

$$(\mathcal{F}_1, \mathcal{F}_2, \mathcal{F}_3) = (2F_1, F_2/x, F_3). \tag{2.7}$$

The naive parton model cross-section for the process $\gamma^* + q_i \rightarrow q_i$ (see figure 2.2) is given simply by

$$\frac{1}{\hat{\sigma}_0}(\hat{\sigma}_T + \hat{\sigma}_L) = e_i^2 \delta(1-z), \tag{2.8}$$

where $z \equiv Q^2/2p_i.q$ and p_i is the momentum of the q_i. Inserting this in the $\mathcal{F}_2$ analogue of (2.6), the parton model expression for the structure function $\mathcal{F}_2$ may be obtained:

$$\mathcal{F}_2 = \sum_i e_i^2 \int_x^1 \frac{dy}{y} q_{0i}(y)\delta(1-\frac{x}{y}) = \sum_i e_i^2 q_{0i}(x), \tag{2.9}$$

where $q_0(x)$ is the "bare" quark distribution in the hadron.

In QCD however, the factorisation theorem requires that the partonic cross-section be calculated to higher orders in α_s. Up to $O(\alpha_s)$ the structure function

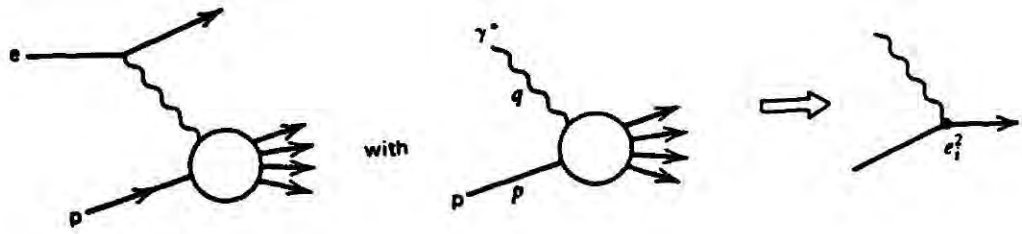

Figure 2.2 Lowest-order parton level graph: $\gamma^* + quark \rightarrow quark$.

may be written as

$$2F_1(x,Q^2) \simeq \int_x^1 \frac{dy}{y} q_0(y)[e^2\delta(x/y-1) + \sigma_{\alpha_s}(x/y,Q^2) + \cdots]. \tag{2.10}$$

The coupling constant α_s used above is the running coupling constant and is described in more detail in the next section. The diagrams of figure 2.3 have to be calculated to obtain an expression for the cross-section at $O(\alpha_s)$. This next-to-leading correction includes real processes

$$\begin{aligned} q + \gamma^* &\rightarrow q + g, \\ g + \gamma^* &\rightarrow q + \bar{q}, \end{aligned} \tag{2.11},$$

(where g represents a gluon) and virtual diagrams which interfere with the zeroth-order graph.

To derive an expression for the total cross-section for the first process in (2.11), consider a general $A + B \rightarrow C + D$ process. The differential cross-section is given by

$$\left.\frac{d\sigma}{d\Omega}\right|_{cm} = \frac{1}{64\pi^2 s}\frac{p_f}{p_i}|\mathcal{M}|^2, \tag{2.12}$$

where $d\Omega$ is an element of the solid angle about $\mathbf{p}_C$, $s = (\mathbf{p}_A + \mathbf{p}_B)^2$, $|\mathbf{p}_A| = |\mathbf{p}_B| = p_i$ and $|\mathbf{p}_C| = |\mathbf{p}_D| = p_f$. The matrix element squared for the process $\gamma^* + q \rightarrow q + g$ is

$$|\bar{\mathcal{M}}|^2 = 32\pi^2(e_i^2\alpha\alpha_s)\frac{4}{3}\left(-\frac{t}{s} - \frac{s}{t} + \frac{2uQ^2}{st}\right), \tag{2.13}$$

where s, u and t are the usual Mandelstam variables. It peaks in the $-t \rightarrow 0$

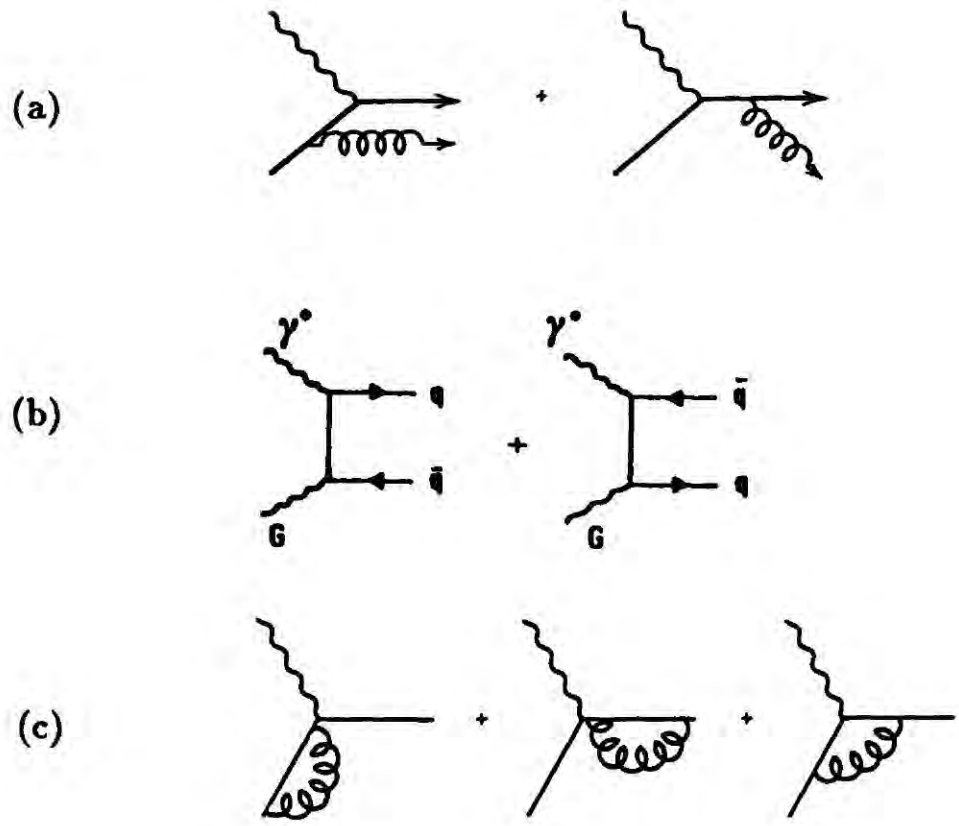

Figure 2.3 The next-to-leading order parton level graphs. (a) gluon emission, (b) gluon scattering and (c) virtual corrections to the leading order diagrams.

region which is indicative of peaking in the forward region. In terms of the partonic variables, the transverse momentum p_T is given by

$$p_T^2 = \frac{stu}{(s+Q^2)^2}, \tag{2.14}$$

and in the small scattering angle case this reduces to

$$p_T^2 = \frac{s(-t)}{s+Q^2}. \tag{2.15}$$

This step allows the solid angle element in (2.12) to be expressed in terms of p_T in the small scattering angle case as

$$d\Omega = \frac{4\pi}{s} dp_T^2. \tag{2.16}$$

And so the general expression for a $2 \rightarrow 2$ process for small scattering angles is

$$\frac{d\sigma}{dp_T^2} \simeq \frac{1}{16\pi s^2} \overline{|\mathcal{M}|^2}. \tag{2.17}$$

Finally, the expression for the matrix element can be rewritten to exhibit its p_T

dependence as

$$\frac{d\sigma}{dp_T^2} \simeq e_i^2 \hat{\sigma}_0 \frac{1}{p_T^2} \frac{\alpha_s}{2\pi} P_{qq}(z), \tag{2.18}$$

where $z = Q^2/(s+Q^2)$ and

$$P_{qq}(z) = \frac{4}{3}\Big(1 + z^2/(1-z)\Big).$$

$P_{qq}(z)$ is the usual Altarelli-Parisi splitting function that describes the probability of a quark radiating a gluon and downgrading its momentum by a fraction z.

The total cross-section for the process is then

$$\hat{\sigma}(\gamma^* q \to qg) = \int_{\mu^2}^{(p_T^2)_{max}} dp_T^2 \frac{d\sigma}{dp_T^2}. \tag{2.19}$$

The upper limit of the p_T^2-integration is given by

$$(p_T^2)_{max} = s^2/4 = Q^2(1-z)/4z \tag{2.20}$$

and then

$$\sigma(\gamma^* q \to qg) \simeq e_i^2 \sigma_0 (\frac{\alpha_s}{2\pi}) P_{qq}(z) \ln(\frac{Q^2}{\mu^2}). \tag{2.21}$$

The constant μ^2 is introduced as a lower cutoff to regularise the divergence when $p_T^2 \to 0$. The dependence of this expression on Q^2 indicates a scaling violation and enters the formalism as a result of gluon emission.

This additional $O(\alpha_s)$ contribution may be added into (2.9) to produce a partly corrected expression for $\mathcal{F}_2$:

$$\mathcal{F}_2(x, Q^2) = \sum_i e_i^2 \int_x^1 \frac{dy}{y} q_{0i} \left[\delta\big(1 - \frac{x}{y}\big) + \frac{\alpha_s}{2\pi} P_{qq}(z) \ln \frac{Q^2}{\mu^2}\right]. \tag{2.22}$$

The change in the structure functions $\mathcal{F}_i$ due to modification by QCD is now shown more explicitly. The programme is to define the parton densities beyond

the leading order in QCD so as to preserve the form of the $\mathcal{F}$'s. (2.22) represents only one part of the $O(\alpha_s)$ corrections. When the remaining $O(\alpha_s)$ corrections are added in the full $O(\alpha_s)$ contribution to the total cross-section produces

$$\mathcal{F}_i(x,t) = \int_x^1 \frac{dy}{y}\Big[\sum_l a_l^i\Big(\delta(1-\frac{x}{y}) + \frac{\alpha_s}{2\pi}tP_{qq}(\frac{x}{y}) + \alpha_s f_{q,i}(\frac{x}{y})\Big)q_{0l}(y) + (\sum_l a_l^i)\Big(\frac{\alpha_s}{2\pi}tP_{qg}(\frac{x}{y}) + \alpha_s f_{g,i}(\frac{x}{y})\Big)g_0(y)\Big]. \tag{2.23}$$

Here l runs over the quarks and antiquarks and the a_l^i are the appropriate coupling factors (including colour factors), $t = \ln Q^2/\mu^2$ and the functions f are $O(\alpha_s)$ process-dependent pieces.

Unfortunately $\alpha_s(Q^2)\ln(Q^2/\mu^2)$ does not vanish at large Q^2 and so the expressions for the $\mathcal{F}'s$ are not very useful in a perturbation series in α_s. However, this type of terms may be factored out and reabsorbed in the definition of the parton densities:

$$q_k(x,t) = q_{0k}(x) + \int_x^1 \frac{dy}{y}\Big[\Big(\frac{\alpha_s}{2\pi}tP_{qq}(\frac{x}{y}) + \alpha_s f_{q,2}(\frac{x}{y})\Big)q_{ok}(y) + \Big(\frac{\alpha_s}{2\pi}tP_{qg}(\frac{x}{y}) + \alpha_s f_{g,2}(\frac{x}{y})\Big)g_o(y)\Big]. \tag{2.24}$$

Note that $q(x,t)$ is defined in terms of $\mathcal{F}_2$. The reason for this is that the largest fraction of the data available for the construction of structure functions is $\mathcal{F}_2$ data from deep inelastic scattering. This has to be taken into account if expressions for the other structure functions are required. For instance, the expression for $\mathcal{F}_1$ is

$$\mathcal{F}_1(x,t) = \int_x^1 \Big[\sum_l e_l^2\Big(\delta(\frac{x}{y}-1) + \alpha_s(t)[f_{q,1}(\frac{x}{y}) - f_{q,2}(\frac{x}{y})]\Big)q_l(y,t) + (\sum_l e_l^2)\alpha_s(t)[f_{g,1}(\frac{x}{y}) - f_{g,2}(\frac{x}{y})]g(y,t)\Big]. \tag{2.25}$$

The connection between this and the Drell-Yan process is now considered. In the naive parton model the differential cross-section with respect to the invariant

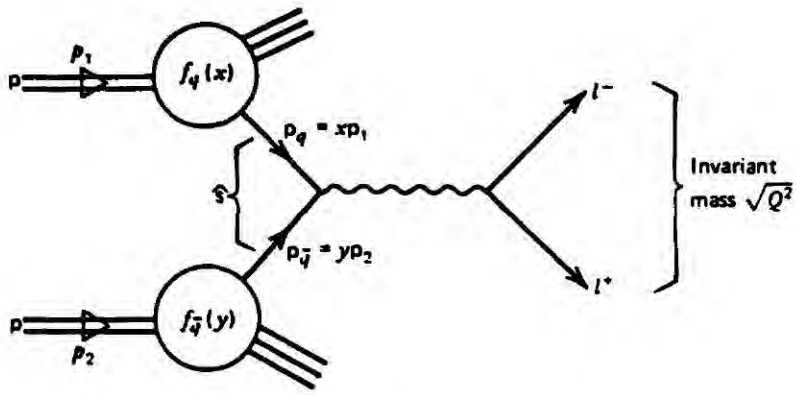

Figure 2.4 Lowest-order Drell-Yan process.

mass squared of the leptons of the Drell-Yan process (see figure 2.4) is simply

$$\frac{d\sigma^{DY}}{dQ^2} = \frac{4\pi\alpha^2}{9sQ^2}\int \frac{dx_1}{x_1}\frac{dx_2}{x_2}\left[\sum_f e_f^2 q_{0f}^{(1)}(x_1)\bar{q}_{0f}^{(2)}(x_2)+(1\leftrightarrow 2)\right]\delta\left(1-\frac{\tau}{x_1x_2}\right). \quad (2.26)$$

In this equation, $\sqrt{s}$ is the incoming partonic energy, $\tau = Q^2/s$, and f runs over the quarks only. (1) and (2) refer to the parent hadrons.

The $O(\alpha_s)$ contributions to the cross-section are from (see figure 2.5)

$$\begin{aligned} g + q(\bar{q}) &\rightarrow \gamma^* + q(\bar{q}) \\ q + \bar{q} &\rightarrow \gamma^* + g, \end{aligned} \quad (2.27)$$

together with the inteference between the zeroth-order diagram and the virtual gluon corrections to the zeroth-order diagram. The Drell-Yan cross-section to $O(\alpha_s)$ may be written as

$$\begin{aligned} \frac{d\sigma^{DY}}{dQ^2} = \frac{4\pi\alpha^2}{9sQ^2}\int_0^1 \frac{dx_1}{x_1}\int_0^1 \frac{dx_2}{x_2}\Bigg[&\left(\sum_f e_f^2 q_0^{(1)}(x_1)q_0^{(2)}(x_2)+(1\leftrightarrow 2)\right) \\ &\times\left(\delta(1-z)+\theta(1-z)\left(\frac{\alpha_s}{2\pi}P_{qq}^{DY}(z)t+\alpha_s f_q^{DY}(z)\right)\right) \\ &+\left(\left(q_0^{(1)}(x_1)+q_0^{(1)}(x_2)\right)g_0(x_2)+(1\leftrightarrow 2)\right) \\ &\times\left(\delta(1-z)+\theta(1-z)\left(\frac{\alpha_s}{2\pi}P_{qg}^{DY}(z)t+\alpha_s f_g^{DY}(z)\right)\right)\Bigg] \end{aligned} \quad (2.28)$$

where as usual $z = Q^2/s$.

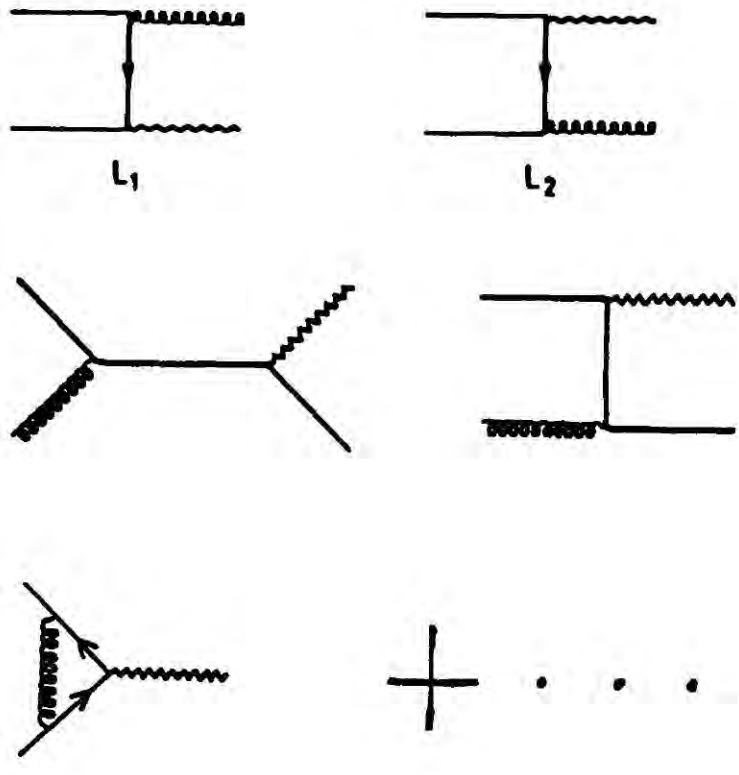

Figure 2.5 $O(\alpha_s)$ corrections to the Drell-Yan process. (a) Gluon emission, (b) Gluon scattering and (c) Virtual corrections to the zeroth-order graph.

(2.28) must be compared with the expression for $\mathcal{F}_2$ which defines the QCD-improved parton density, that is, $q(x,t) + \bar{q}(x,t) = \mathcal{F}_2(x,t)$. The equivalence of the splitting functions in this equation and in (2.23) has been checked [16] and so

$$\begin{aligned} P_{qq}^{DY}(z) &= P_{qq}(z), \\ P_{qg}^{DY}(z) &= P_{qg}(z). \end{aligned} \tag{2.29}$$

The expression for the Drell-Yan cross-section includes the process-dependent quantities f_q^{DY} and f_g^{DY}. However, to non-leading-order parton densities in the hadron are defined in terms of $f_q^{(2)}$ and $f_g^{(2)}$, which, as seen earlier, are closely related to the deep inelastic scattering data that are available. The expression for the Drell-Yan cross-section must be corrected for this, giving

$$\frac{d\sigma^{DY}}{dQ^2} = \frac{4\pi\alpha^2}{9sQ^2}\int_0^1 \frac{dx_1}{x_1}\int_0^1 \frac{dx_2}{x_2}\Big[\Big(\sum_f e_f^2 q_f^{(1)}(x_1,t)\bar{q}_f^{(2)}(x_2,t) + (1 \leftrightarrow 2)\Big)$$
$$\times \big(\delta(1-z) + \alpha_s(t)\theta(1-z)[f_q^{DY}(z) - 2f_q^{(2)}(z)]\big)$$
$$+ \big(\mathcal{F}_2^{(1)}(x_1,t)G^{(2)}(x_2,t) + (1 \leftrightarrow 2)\big)\alpha_s(t)\theta(1-z)[f_g^{DY}(z) - f_g^{(2)}(z)]\Big]. \tag{2.30}$$

The calculation of the cross-section to $O(\alpha_s)$ reduces to the calculation of the two terms $f_q^{DY}(z) - 2f_q^{(2)}(z)$ and $f_g^{DY}(z) - f_g^{(2)}(z)$. They are independent of any infrared singularities and of the method of regularisation. Their derivation to $O(\alpha_s)$ is performed by Altarelli *et al.* [3] and expressions for the various terms are presented in that paper.

To establish connection between the above discussion and the operational procedure in the work of Ellis *et al.* [10] and Arnold and Reno [11], the procedure of Altarelli *et al.* [3] is presented here. Consider again the case of photon-parton scattering. If 4-momentum of the parton is p and that of the photon q, then the absorptive part of the forward scattering amplitude may be expanded in the usual way:

$$W^{\mu\nu} = W_1\left(-g^{\mu\nu} + \frac{q^\mu q^\nu}{q^2}\right) + W_2\left(p^\mu - \frac{p.q}{q^2}q^\mu\right)\left(p^\nu - \frac{p.q}{q^2}q^\nu\right), \tag{2.31}$$

where only two of the four inelastic structure functions in the most general expression for this tensor are independent. In the large Q^2 case when virtual photons can resolve the constituents within the hadron, then

$$\begin{aligned}\mathcal{F}_2(z,Q^2) &= \frac{p.qW_2}{z}\\ \mathcal{F}_1(z,Q^2) &= 2W_1.\end{aligned} \tag{2.32}$$

By saturating the indices within these expressions with the tensors $-g^{\mu\nu}$ and $p^\mu p^\nu$ in n-dimensions the following expressions are obtained:

$$\begin{aligned}-g^{\mu\nu}W_{\mu\nu} &= (1-\epsilon)\mathcal{F}_2(z,Q^2) - (\frac{3}{2} - \epsilon)(\mathcal{F}_2(z,Q^2) - \mathcal{F}_1(z,Q^2)),\\ p^\mu p^\nu W_{\mu\nu} &= \frac{Q^2}{8z^2}(\mathcal{F}_2(z,Q^2) - \mathcal{F}_1(z,Q^2)).\end{aligned} \tag{2.33}$$

The second of these is proportional to the longitudinal cross-section σ_L which

has been calculated by Zee *et al.* [17]

$$\sigma_L = \alpha_s[f_q^{(2)}(z) - f_q^{(1)}(z)] = \frac{\alpha_s}{2\pi} C_F 2z. \tag{2.34}$$

Hence to obtain an expression for $\mathcal{F}_2$ it is necessary to calculate the first equation in (2.33) from the relevant Feynman graphs.

As has already been seen, the first graph to consider is just the basic $\gamma^* + q \rightarrow q$ (see figure 2.2) which is given by

$$\mathcal{F}_2 = \delta(1-z), \tag{2.35}$$

and which defines the normalisation of the partonic cross-section. To the next order in α_s there are two contributions with quarks in the initial channel, firstly

$$\gamma^* + q \rightarrow q + g \tag{2.36}$$

and secondly, the interference terms between the lowest order graph and the virtual corrections to the lowest order (sce figure 2.3). In n-dimensions it is necessary to make the replacement $\alpha_s \rightarrow \alpha_s(\mu^2)^\epsilon$, where μ has dimensions of mass so as to maintain the correct dimensionality of the matrix element squared. In n-dimensions the matrix element squared for real gluon emission is

$$|\mathcal{M}|^2 = 4\alpha_s \frac{4}{3}(1-\epsilon)(\mu^2)^\epsilon[(1-\epsilon)(-\frac{\hat{s}}{\hat{t}} - \frac{\hat{t}}{\hat{s}}) - \frac{2\hat{u}q^2}{\hat{s}\hat{t}} + 2\epsilon] \tag{2.37}$$

The general expression for two particle phase space in n-dimensions for the production of two on-shell massless particles is

$$PS = \int \frac{d^n p_3}{(2\pi)^{n-1}} \int \frac{d^n p_4}{(2\pi)^{n-1}} (2\pi)^n \delta^{(n)}(p_1 + p_2 - p_3 - p_4)\delta(p_3^2)\delta(p_4^2), \tag{2.38}$$

where the initial state particles have momentum $p_{1,2}$ and the final state particles have momentum $p_{3,4}$. If the initial particles are directed along the $(n-1)$th

direction then in the centre-of-mass system of the final state particles p_4 may be written:

$$p_4 = (|p_4|, \cdots, |p_4|cos\theta), \tag{2.39}$$

where the dots represent $n-2$ unspecified momenta. In this frame the $n-2$ angular integrals can be done so that (2.38) may be written as

$$PS = \frac{1}{4\pi}\frac{(4\pi)^\epsilon}{\Gamma(1-\epsilon)}\int_0^\infty d|p_4||p_4|^{1-2\epsilon}\int_{-1}^{1} d(cos\theta)(1-cos^2\theta)^{-\epsilon}\delta(s-2\sqrt{s}|p_4|). \tag{2.40}$$

The $|p_4|$ integral is trivially done with the δ function. By setting $y = \frac{1}{2}(1+cos\theta)$, this reduces to

$$PS = \frac{1}{8\pi}\left(\frac{4\pi}{s}\right)^\epsilon \frac{1}{\Gamma(1-\epsilon)}\int_0^1 dy(y(1-y))^{-\epsilon}. \tag{2.41}$$

In the centre-of-mass frame we have

$$\begin{aligned} s &= \frac{Q^2(1-z)}{z} \\ t &= \frac{-Q^2}{z}(1-y) \\ u &= \frac{Q^2}{z}y. \end{aligned} \tag{2.42}$$

Using (2.42) and (2.34) in the first equation in (2.33) and integrating over y, an expression for $\mathcal{F}_2(z,Q^2)|_{real}$ is obtained:

$$\mathcal{F}_2(z,Q^2)|_{real} = \frac{\alpha_s}{2\pi}C_F\left(\frac{4\pi\mu^2}{Q^2}\right)^\epsilon \frac{\Gamma(1-\epsilon)}{\Gamma(1-2\epsilon)}X(z,\epsilon), \tag{2.43}$$

where X is obtained by incorporating the matrix element squared for the $O(\alpha_s)$ process for the real gluon emission into the longitudinal cross-section discussed

above. Finally, by adding in the virtual corrections the final result for the structure function $\mathcal{F}_2$ is

$$\begin{aligned}\mathcal{F}_2 = \delta(1-z) - \frac{1}{\epsilon}\frac{\alpha_s}{2\pi}C_F P_{qq}(z)\left(\frac{4\pi\mu^2}{Q^2}\right)^{\epsilon}\frac{\Gamma(1-\epsilon)}{\Gamma(1-2\epsilon)} \\ + \frac{\alpha_s}{2\pi}C_F\left[(1+z^2)\left(\frac{\ln(1-z)}{1-z}\right)_+ - \frac{3}{2}\frac{1}{(1-z)_+} - \frac{1+z^2}{(1-z)}\ln z\right. \\ \left. + 3 + 2z - (\frac{9}{2}+\frac{\pi^2}{3})\delta(1-z)\right].\end{aligned} \tag{2.44}$$

If this calculation is done explicitly, a double pole in ϵ cancels between the virtual and real contributions. From this expression the function $f_q^{(2)}$ may be obtained [3]

$$\begin{aligned}\alpha_s f_q^{(2)} = \frac{\alpha_s}{2\pi}C_F\left[(1+z^2)\left(\frac{\ln(1-z)}{1-z}\right)_+ - \frac{3}{2}\frac{1}{(1-z)_+} - \frac{1+z^2}{(1-z)}\ln z\right. \\ \left. + 3 + 2z - (\frac{9}{2}+\frac{\pi^2}{3})\delta(1-z) + P_{qq}(z)\left(-\frac{1}{\epsilon} + \gamma_E - \ln 4\pi + \ln\frac{\mu^2}{Q^2}\right)\right].\end{aligned} \tag{2.45}$$

The term proportional to

$$\left(-\frac{1}{\epsilon} + \gamma_E - \ln 4\pi\right) \tag{2.46}$$

in the above contains the relevant Altarelli-Parisi splitting functions. In the MS-scheme (following the prescription of 't Hooft[18]), the $1/\epsilon$ term is subtracted out. Bardeen *et al.* [19] later noted that this divergent term always appears together with γ_E and $\ln 4\pi$. Eliminating the divergences by the subtraction of the $1/\epsilon$ term introduces the transcendentals γ_E and $\ln 4\pi$, which enter the result because of the specific way in which the calculation was continued to $n \neq 4$ dimensions. They are not present in the physical predictions of the theory. In the $\overline{MS}$-scheme all three terms are subtracted out. The γ_E term is the Euler-Mascheroni constant.

Comparison between the definition of $f_q^{(2)}$ above and the expression for the structure functions given by Arnold and Reno [11] and Ellis *et al.* [10] shows a full connection between the two. The MRS structure functions that have been used in this study, like the Diemoz *et al.* set [20] used by Arnold and Reno, have quark

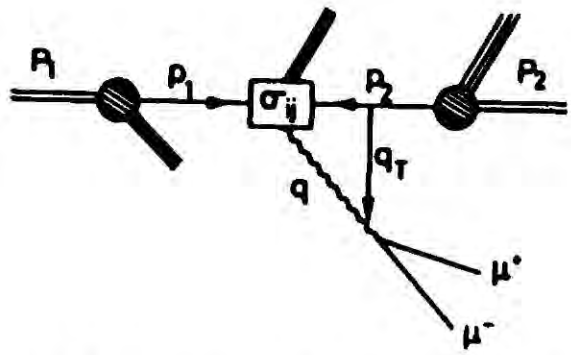

Figure 2.6 The hadronic production of vector bosons.

distributions obtained from deep inelastic scattering data. The entire calculation has been performed in the $\overline{MS}$-scheme and this entails the subtraction of the anomalous dimension term described above and the setting of the $f_q^{(2)}$ and $f_g^{(2)}$ terms to zero since these are absorbed into the structure functions.

For this next section of the discussion the notation of Arnold and Reno [11] is used. The generic process that is studied is shown schematically in figure 2.6 and the cross-section that corresponds to this process may be expressed as

$$\frac{d\sigma}{dpt^{W2}dy^W} = \sum_{i,j} \int dx_1 dx_2 \frac{d\tilde{\sigma}_{ij}}{dtdu}(\alpha_s(\mu^2), p_1, p_2)\, G_i^A(x_1, M^2) G_j^B(x_2, M^2), \quad (2.47)$$

where μ^2 and M^2 are the renormalisation and factorisation scales respectively, and $d\tilde{\sigma}_{ij}/dtdu$ is the QCD-improved constituent cross-section, which is a function of the partonic variables of the initial state partons and the strong coupling constant (see section 2.4). A and B are hadron labels, i and j run through the partonic constituents of the hadrons and the G_i^A refers to the distribution of parton i in hadron A. This differential form of the cross-section is connected to the usual expression for cross-sections via a constant factor

$$\frac{d\sigma}{dp_T^{W2}dy^W} = \pi \frac{E^W d\sigma}{d^3p^W}. \quad (2.48)$$

$d\tilde{\sigma}_{ij}/dtdu$ is convoluted with the structure functions to produce the hadronic cross-section.

The first step is to calculate in perturbation theory the bare result for the Feynman diagrams. The calculation of Arnold and Reno [11] is described in some detail in section 2.3. The QCD-improved hard-process cross-section is given by

$$\frac{s\,d\tilde{\sigma}_{ij}}{dt\,du} = \frac{sd\sigma_{ij}^{(1)}}{dt}\delta(s+t+u-m_W^2) + \frac{sd\tilde{\sigma}_{ij}^{(2)}}{dt\,du}\theta(s+t+u-m_W^2). \qquad (2.49)$$

The superscripts indicate the order in α_s. The relationship between this finite hard-process cross-section and that calculated in perturbation theory is defined by the relationship between the bare and factorisation scheme dependent structure functions. The convention adopted by Arnold and Reno is

$$\begin{aligned}\frac{s\,d\tilde{\sigma}}{dt\,du} =& \frac{sd\sigma^{(1)}}{dt}\delta(s+t+u-m_W^2) \\ &- \frac{\alpha_s}{2\pi}\int_0^1 dx_1 R(x_1,M^2)\frac{sd\sigma^{(1)}}{dt}\Big|_{p_1\to x_1 p_1}\delta(x_1(s+t-m_W^2)+u) \\ &- \frac{\alpha_s}{2\pi}\int_0^1 dx_2 R(x_2,M^2)\frac{sd\sigma^{(1)}}{dt}\Big|_{p_2\to x_2 p_2}\delta(x_2(s+u-m_W^2)+t).\end{aligned} \qquad (2.50)$$

The functions R that appear in (2.50) are obtained from (2.45) and are given by

$$R(z,M^2) = \left[C_f P_{qq}(z)\left(-\frac{1}{\epsilon} - \ln 4\pi + \gamma_E + \ln\frac{M^2}{\mu^2}\right)\right] + f_{qq}(z). \qquad (2.51)$$

These have been generalised in the Arnold and Reno paper to

$$R_{i\leftarrow j}(z,M^2) = \left[C_f P_{qq}(z)\left(-\frac{1}{\epsilon} - \ln 4\pi + \gamma_E + \ln\frac{M^2}{\mu^2}\right)\right] + C_{i\leftarrow j}(z). \qquad (2.52)$$

The C functions are immediately identifiable with the process-dependent functions $f_{q,g}$ obtained earlier. The relationship between the renormalised and bare structure functions can now be obtained explicitly as

$$G_{i/A}(x,M^2) = \int_x^1 \frac{dz}{z}\left[\delta_{i,j}\delta(z-1) + \frac{\alpha_s}{2\pi}R_{i\leftarrow j}(z,M^2)\right]G_{j/A}^{bare}\left(\frac{x}{z}\right). \qquad (2.53)$$

The x_1 and x_2 integrals in (2.50) are trivially done,

$$\begin{aligned}\frac{s\,d\tilde{\sigma}}{dt\,du} =& \frac{s d\sigma^{(1)}}{dt}\delta(s+t+u-m_W^2) \\ &- \frac{\alpha_s}{2\pi}\frac{1}{s+t-m_W^2}C_{k\leftarrow i}\left(\frac{-u}{s+t-m_W^2}, M^2\right)\frac{s d\sigma^{(1)}}{dt}\bigg|_{p_1\to -up_1/(s+t-m_W^2)} \\ &- \frac{\alpha_s}{2\pi}\frac{1}{s+u-m_W^2}C_{k\leftarrow j}\left(\frac{-t}{s+u-m_W^2}, M^2\right)\frac{s d\sigma^{(1)}}{dt}\bigg|_{p_2\to -tp_2/(s+u-m_W^2)}.\end{aligned} \tag{2.54}$$

These definitions fix the conventions and procedure for the rest of the calculation. As has already been discussed, in the $\overline{MS}$ scheme the term proportional to $-1/\epsilon - \ln 4\pi + \gamma_E$ is subtracted out and the functions $C_{i\leftarrow j}^{\overline{MS}} = 0$. Finally, in this study the factorisation scale, M^2, is set equal to the renormalisation scale, μ^2 and so the term $\ln M^2/\mu^2 = 0$ in (2.52).

2.3 Notation and Matrix Elements

Consider a proton and an antiproton with 4-momenta P_1 and P_2 respectively, which collide with centre-of-mass energy $\sqrt{S}$ to produce a W or Z boson, with 4-momentum p_W, and anything else. This process is described schematically in figure 2.6, together with a possible decay mode of the vector boson. In the centre-of-mass frame of the colliding hadrons, P_1 and P_2 have components

$$\begin{aligned}P_1 &= \sqrt{S}/2(0,0,1;1) \\ P_2 &= \sqrt{S}/2(0,0,-1;1)\end{aligned} \tag{2.55}$$

and p_W is defined by

$$p_W = (\mathbf{p}_T^W, p_L^W; E^W). \tag{2.56}$$

The hadronic variables in the problem are given by

$$\begin{aligned}S &= (P_1+P_2)^2, \\ T &= (P_1-p_W)^2, \\ U &= (P_2-p_W)^2.\end{aligned} \tag{2.57}$$

The calculation assumes that there is just one active parton per hadron. If x_1

and x_2 are the momentum fractions of the relevant quarks or gluons within the hadrons then we can define the momenta of the partons in the hard interaction as

$$\begin{aligned} p_1 &= x_1 P_1, \\ p_2 &= x_2 P_2 \end{aligned} \tag{2.58}$$

and the partonic variables are

$$\begin{aligned} s &= x_1 x_2 S, \\ t &= x_1 T, \\ u &= x_2 U. \end{aligned} \tag{2.59}$$

In this study it is necessary to consider both the $2 \to 2$ and the $2 \to 3$ cases, corresponding to $W+$ one-jet and to $W+$ two-jets respectively. As this is the study of the fully inclusive cross-section, that is $p + \bar{p} \to W + X$, it is suitable in the latter case to define s_2, the invariant mass of the two-jet system

$$s_2 \equiv s + t + u - m_W^2. \tag{2.60}$$

The QCD Coupling Constant.

In the last section the scale dependence of the renormalised QCD coupling was indicated. This scale dependence of $\alpha_s \equiv g_s^2/4\pi$ is defined by the $\beta-$function:

$$\begin{aligned} \mu^2 \frac{\partial \alpha_s(\mu^2)}{\partial \mu^2} &= -\frac{\alpha_s(\mu^2)}{4\pi}\beta_0 - \left(\frac{\alpha_s(\mu^2)}{4\pi}\right)^2 \beta_1 + \cdots \\ \beta_0 &= 11 - \frac{2}{3} n_f \\ \beta_1 &= 102 - \frac{38}{3} n_f. \end{aligned} \tag{2.61}$$

If the first two terms on the right hand side of this expression are kept and the truncated differential equation is solved for $\alpha_s(\mu^2)$ then

$$\frac{1}{\alpha_s} + \frac{\beta_1}{4\pi\beta_0} \ln\left(\frac{\frac{\beta_1}{4\pi\beta_0}\alpha_s}{1 + \frac{\beta_1}{4\pi\beta_0}\alpha_s}\right) = \frac{\beta_0}{2\pi} \ln\frac{\mu}{\Lambda}. \tag{2.62}$$

A constant of integration, Λ, is introduced in this solution and is forced to be dimensionful. This α_s is called the 'two-loop' coupling constant, and is a function

of the scale μ and the fundamental QCD scale parameter Λ. This solution, which is used in the computations in these projects, is obtained by inverting (2.62) in a short fortran subroutine as a function of the scales mentioned above.

Matrix Elements.

The squared matrix elements presented in references [10] and [11] are given for the standard Drell-Yan process, that is the production of a virtual photon + one jet or two jets, either from quark-antiquark annihilation or quark-gluon scattering and from corrections to these processes. At the end of the discussion the modifications to these formulae for the production of W and Z bosons will be presented.

The leading-order processes that contribute to the large p_T spectrum of bosons produced at $p\bar{p}$ colliders are the $O(\alpha_s)$ processes (see figure 2.5)

$$\begin{aligned} q + \bar{q} &\rightarrow W + g, \\ q(\bar{q}) + g &\rightarrow W + q(\bar{q}). \end{aligned} \tag{2.63}$$

The interference between the zeroth-order $q\bar{q}$ annihilation term and the $O(\alpha_s^2)$ virtual diagram (see figure 2.5) contributes to $O(\alpha_s)$, but the only source of transverse momentum in this contribution (as in the the case of the zeroth-order diagram) is the intrinsic transverse momentum of the partons within the hadrons, which is only relevant in the very small p_T range. In this study calculations are restricted to the region in which finite-order perturbative QCD is valid and this restricts the study to the large-p_T region.

The hard subprocess cross-section for the $O(\alpha_s)$ $q\bar{q}$-annihilation term shown above is given by

$$s\frac{d\sigma^{(1)}}{dtdu} = Ke_f^2\frac{\alpha_s}{s}T_0(Q^2,u,t)\delta(s+t+u-Q^2), \tag{2.64}$$

where e_f is the charge of the quark, $Q^2 = m_W^2$ in the case of W-production, T_0

is the leading-order matrix element squared, given by

$$T_0(Q^2,u,t) = \left[(1-\epsilon)\left(\frac{u}{t}+\frac{t}{u}+\frac{2Q^2(Q^2-u-t)}{ut}\right)-2\epsilon\right] \tag{2.65}$$

and K, which contains the coupling and colour factors *etc.*, is given by

$$K = \frac{2\pi\alpha}{N_c}C_F\frac{1-\epsilon}{\Gamma(1-\epsilon)}\left(\frac{4\pi\mu^2}{Q^2}\right)^{\epsilon}\left(\frac{sQ^2}{ut}\right)^{\epsilon}. \tag{2.66}$$

As has been mentioned earlier, α_s is rescaled to keep it dimensionless in n-dimensions, that is

$$\alpha_s \rightarrow \alpha_s(\mu^2)^{\epsilon}.$$

The $q-g$ interaction that contributes to this order may be obtained by direct crossing of the $q\bar{q}$ interaction to this order, with a suitable adjustment of the colour factors and spin- and colour-averages. The hard subprocess cross-section is given by

$$s\frac{d\sigma^{(1)}}{dtdu} = -K'e_f^2\frac{\alpha_s}{s}S_0(Q^2,u,t)\delta(s+t+u-Q^2), \tag{2.67}$$

where $K' = K/(2C_F)$ and S_0 is obtained by an $s \leftrightarrow u$ crossing of T_0

$$S_0(Q^2,s,t) = \left[(1-\epsilon)\left(\frac{s}{t}+\frac{t}{s}+\frac{2Q^2(Q^2-s-t)}{st}\right)-2\epsilon\right] \tag{2.68}$$

These two processes complete the $O(\alpha_s)$ contribution to the production of a boson and one jet.

The $O(\alpha_s^2)$ contributions to the cross-sections have many origins. As has been mentioned earlier, the Ellis *et al.* [10] paper considers only the non-singlet case, which will be considered first here. The diagrams of figure 2.7 are the virtual corrections to the $O(\alpha_s)$ annihilation process in figure 2.5 These are of $O(\alpha_s^3)$ and so are beyond the order to which this calculation is done, but the interference of these terms with the $O(\alpha_s)$ terms produces an $O(\alpha_s^2)$ contribution. There are two pieces to this part of the squared matrix elements, one of which is proportional

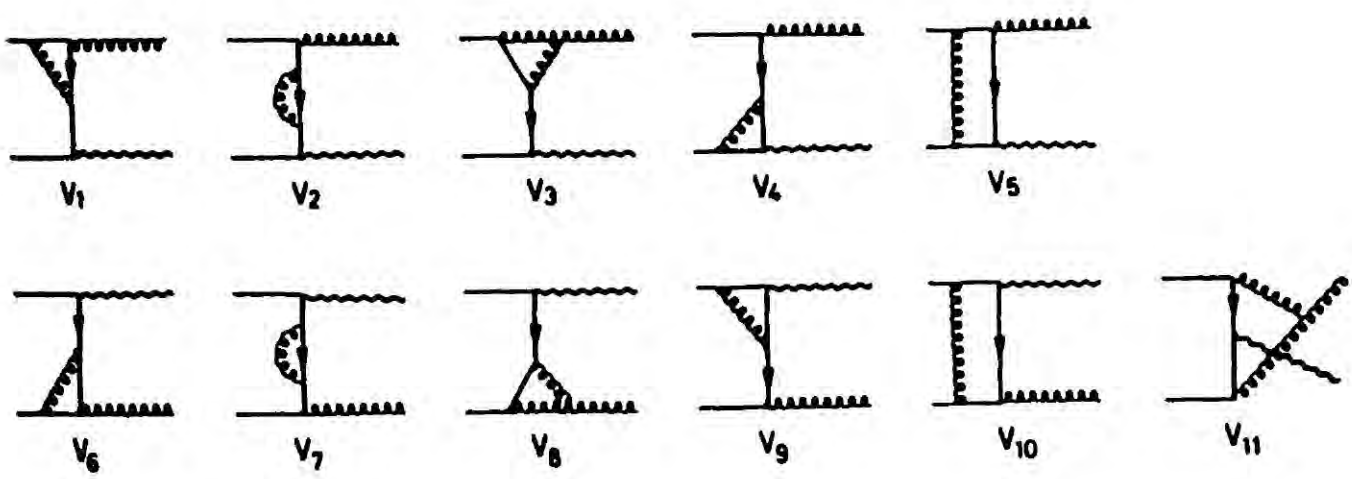

Figure 2.7 Virtual corrections to the leading-order non-singlet graphs.

to the leading order and is ultraviolet renormalised by including the necessary counterterm for the $\overline{MS}$ scheme. This counterterm is given by:

$$s\frac{d\sigma^{CT}}{dt} = e_f^2 K \frac{\alpha_s}{s} T_0(Q^2,u,t)\frac{\alpha_s}{2\pi}\frac{\Gamma(1-\epsilon)}{\Gamma(1-2\epsilon)}(4\pi)^\epsilon(\frac{2}{3}T_R - \frac{11}{6}N_c)\frac{1}{\epsilon}, \qquad (2.69)$$

where, as usual, the coupling constant is replaced by the running coupling constant described above. The remaining piece of this contribution to the $O(\alpha_s^2)$ cross-section is finite in the limit $\epsilon \to 0$ and requires no further renormalisation.

In the non-singlet case there are three identifiable processes that give rise to $O(\alpha_s^2)$ real corrections to leading order. These are

$$\begin{aligned} q + \bar{q} &\to W + g + g \\ q + \bar{q}, &\to W + q + \bar{q}, \\ q + q &\to W + q + q, \end{aligned} \qquad (2.70)$$

and they are shown in figures 2.8-2.10 respectively. With the relevant cuts, it is posssible to ensure that the massive boson is well separated from the beam direction. Then the only infrared and collinear singularities that can exist occur in figure 2.8 and in the square of the matrix element of the first two diagrams of figure 2.9. These singularities appear as poles in ϵ, after integration over

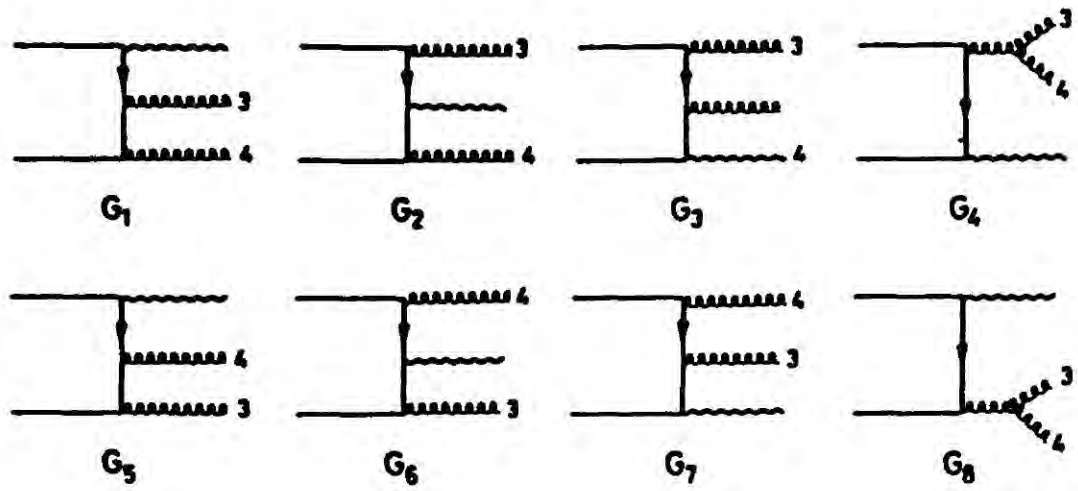

Figure 2.8 $O(\alpha_s^2)$ **diagrams that contribute to the process** $q+\bar{q} \rightarrow W+g+g$.

the phase space of the gluons. The singularities due to soft gluons show up as poles in the already defined variable s_2, the invariant mass of the two-jet system recoiling against the boson. When one of the gluons is soft (as in the leading-order) the singularity appears at $s_2 = 0$. Collinear divergences appear as usual after integration over the angular parameters of the final state gluons. The poles in ϵ in the soft gluon case are highlighted by implementing the identity

$$\frac{1}{(s_2)^{1+\epsilon}} = -\frac{1}{\epsilon}\delta(s_2)[1-\epsilon \ln A+\frac{1}{2}\epsilon^2 \ln^2 A]+\frac{1}{(s_2)_{A+}}-\epsilon\left(\ln s_2\right)_{A+}+O(\epsilon^2), \quad (2.71)$$

where the plus-prescription terms are defined in the usual way as:

$$\begin{aligned}\int_0^A ds_2 \frac{f(s_2)}{(s_2)_{A+}} &= \int_0^A \frac{ds_2}{s_2}[f(s_2)-f(0)], \\ \int_0^A ds_2 \left(\frac{\ln s_2}{(s_2)}\right)_{A+} &= \int_0^A \frac{ds_2}{s_2}[f(s_2)-f(0)]\ln(s_2).\end{aligned} \quad (2.72)$$

The upper limit A in these expressions will be obtained later as a function of the external momenta and the momentum fractions.

Ellis *et al.* [10] divide up these real $O(\alpha_s^2)$ contributions into four parts. The terms that contain mass singularities (described above) are factored into

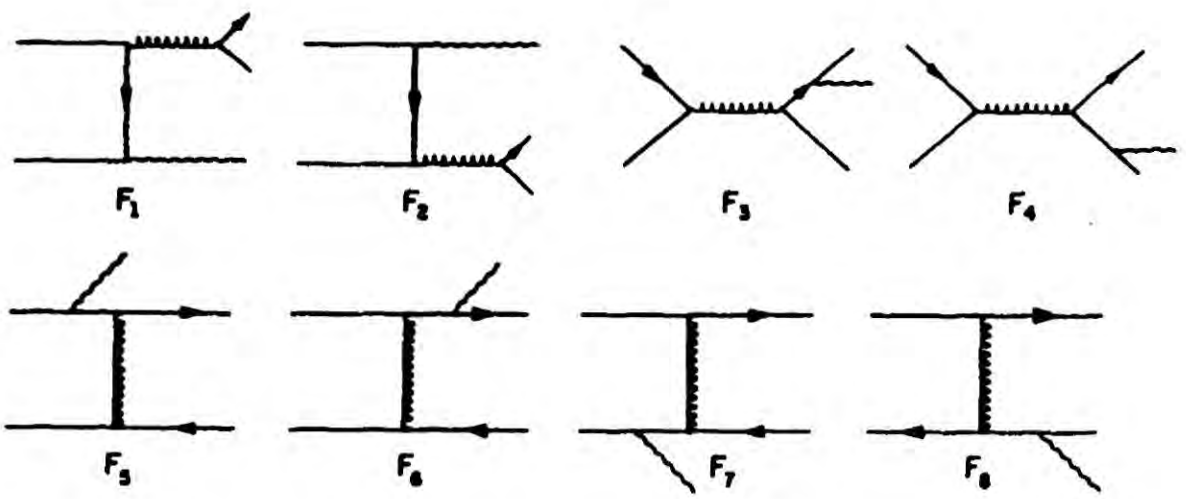

Figure 2.9 $O(\alpha_s^2)$ **diagrams that contribute to the process** $q+\bar{q} \rightarrow W+q+\bar{q}$.

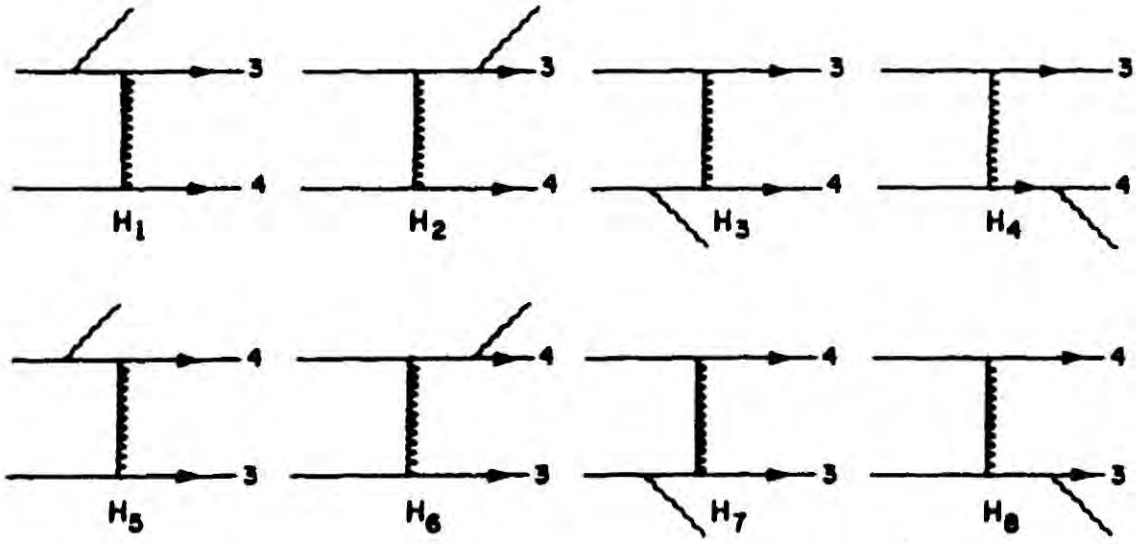

Figure 2.10 $O(\alpha_s^2)$ **diagrams that contribute to the process** $q+q \rightarrow W+q+q$ **in the non-singlet case.**

$sd\sigma_I/dtdu$ and, following the discussion of section 2.2, this piece may be written as

$$s\frac{d\sigma_I}{dtdu} = \frac{\alpha_s}{2\pi}\int dx_1 R(x_1, M^2) s\frac{d\sigma^{(1)}}{dt}\bigg|_{p_1 \to x_1 p_1} \delta(x_1(s+t-Q^2)+u)$$
$$+ \frac{\alpha_s}{2\pi}\int dx_2 R(x_2, M^2) s\frac{d\sigma^{(1)}}{dt}\bigg|_{p_2 \to x_2 p_2} \delta(x_2(s+u-Q^2)+t) + s\frac{d\tilde{\sigma}_I}{dtdu}, \tag{2.73}$$

where the function R has been defined in (2.51). As has already been mentioned this part of the $O(\alpha_s^2)$ correction contains the singularities as $s_2 \to 0$ and these singularities cancel with the singularities in the virtual component of the $O(\alpha_s^2)$ cross-section. These cancellations are manifest in the expressions for the matrix elements in the appendices of references [10,11]. After convolution with parton densities the terms proportional to the $R-$functions in (2.73) will define the scale-dependent parton densities. The other three terms require no factorisation and so $d\sigma_{II} = d\tilde{\sigma}_{II}$, $d\sigma_{III} = d\tilde{\sigma}_{III}$, $d\sigma_{IV} = d\tilde{\sigma}_{IV}$. The non-singlet hard cross-section then is defined by

$$\Delta_{qq'}(x_1, x_2) = s\frac{d\sigma^{virtual}}{dtdu} + s\frac{d\tilde{\sigma}^{real}}{dtdu}. \tag{2.74}$$

The full expression for this non-singlet $O(\alpha_s^2)$ correction to the leading order is given in the appendix to reference [10].

The singlet sector of this $O(\alpha_s^2)$ correction has been dealt with by Arnold and Reno [11]. This contribution to the correction comes from the following real processes:

$$q(\bar{q}) + g \to W + q(\bar{q}) + g$$
$$g + g \to W + q + \bar{q} \tag{2.75}$$
$$q + q \to W + q + q.$$

The $O(\alpha_s^2)$ contributions with a quark and a gluon in the initial channel are obtained by performing an $s \leftrightarrow u$ crossing on the diagrams G_i in figure 2.8, while the contributions with two gluons in the initial channel are likewise obtained with the appropriate relabelling of the momenta in the G_i diagrams of figure 2.8. The quark singlet contributions from the diagrams in figures 2.9 and 2.10 are simply added in.

As in the case of the non-singlet correction, the interference of the virtual diagrams at $O(\alpha_s^3)$ with the leading order diagrams for the process with a gluon

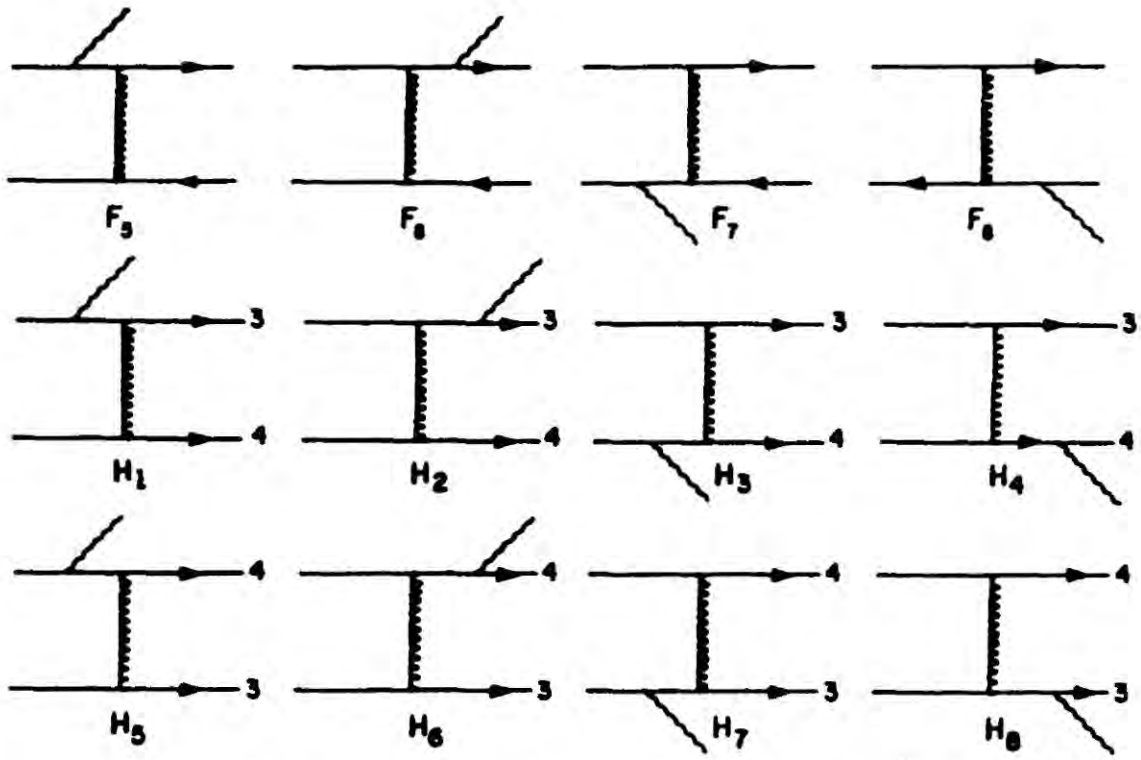

Figure 2.11 The diagrams that make a contribution to the AA- and VV-terms in Z production.

in the initial channel produces an $O(\alpha_s^2)$ contribution. This is obtained from the diagrams V_i in figure 2.7 by suitable crossings. The hard process cross-section is obtained by analytic continuation, where logarithms yield terms proportional to $i\pi$. Arnold and Reno performed the calculation in Euclidean space, where it is real, continued from Euclidean s to Euclidean u and *vice versa*, and finally they continued back to Minkowski space and took the real part.

For the case of W-production, both vectorial and axial contributions must be considered and this requires a treatment of γ_5 in dimensional regularisation. Following Chanowitz *et al.* [21], Arnold and Reno indicate that there exists some ambiguity in this application but demonstrate that this ambiguity is irrelevant for their calculation. The VA-terms vanish when the phase space integrals are performed. In the case of massless fermions, the AA- and VV-terms are identical in all except the interference contributions shown in figure 2.11:

$$\begin{aligned} &2Re(F_5 + F_6)^*(F_7 + F_8), \\ &2Re(H_1 + H_2)^*(H_3 + H_4), \\ &2Re(H_5 + H_6)^*(H_7 + H_8). \end{aligned} \tag{2.76}$$

The squared matrix elements for these processes are separated into their vectorial and axial parts. Further details are presented in their paper [11].

The complete structure of the cross-section for massive photon and W,Z production is presented as a sum over the different contributions. To adjust the formulae for W,Z production several changes have to be made. The appropriate weak coupling constants have to be introduced, the correct flavour combinations have to be chosen, together with the relevant K-M matrix elements, and finally a sum has to be performed over the final flavours.

Coupling Constants.

For the production of intermediate vector bosons the following change has to be made in the coupling constant:

$$\alpha \rightarrow \frac{\alpha_W}{4} = \frac{\sqrt{2} G_F m_W^2}{4\pi} = \frac{\alpha}{4 sin^2\theta_W}, \tag{2.77}$$

where α is the electromagnetic fine structure constant, which runs to $(127.8)^{-1}$ at the scale of the W mass, and $sin^2\theta_W$ is defined in terms of the parameter ρ, where

$$\rho = \frac{m_W^2}{m_Z^2 cos^2\theta_W}. \tag{2.78}$$

Within the standard model, this parameter is constrained to be close to unity. The experimentally obtained value of $\sin^2\theta_W$ is

$$sin^2\theta_W \simeq 0.23. \tag{2.79}$$

The complete normalisation and coupling constants then are given by:

$$\begin{aligned} K_{qq} &\rightarrow K_{qq}/4 sin^2\theta_W, \\ K_{qg} &\rightarrow K_{qg}/4 sin^2\theta_W. \end{aligned} \tag{2.80}$$

Matrix element and parton combinations for W production

The structure of the hard-process cross-section for the production of massive photons is simply the sum of the different parts given in the appendices to references [10] and [11]. For W and Z production, the combinations of the different contributions are somewhat trickier and require the introduction of the K-M matrix elements and various quark-quark, quark-gluon and gluon-gluon combinations. In the following construction of the cross-section parts, i, j are the family indices of the initial-state partons. The weak mixing angles are contained in the matrices

$$\begin{aligned} \theta_{ij} &= |K_{ij}|^2, \\ D_{ij} &= Re(K^\dagger K), \\ U_{ij} &= Re(K K^\dagger), \end{aligned} \tag{2.81}$$

where K is the K-M matrix. Following Arnold and Reno the top quark and all terms of the order

$$[b \text{ distribution in hadron}] \times [b \text{ weak mixing angles}] \tag{2.82}$$

have been ignored. This reduces the Θ-matrix to the form

$$\Theta \simeq \begin{pmatrix} cos^2\theta_c & sin^2\theta_c & 0 \\ sin^2\theta_c & cos^2\theta_c & 0 \\ 0 & 0 & 0 \end{pmatrix}, \tag{2.83}$$

and the D and U matrices to

$$D \simeq U \simeq \begin{pmatrix} 1 & 0 & 0 \\ 0 & 1 & 0 \\ 0 & 0 & 0 \end{pmatrix}. \tag{2.84}$$

For W^+ production:

$$
\begin{aligned}
u\bar{d} \to W^+ &: \Theta_{ij}[(q\bar{q} \to g\gamma^*) + (q\bar{q} \to gg\gamma^*) + 2T_R|F_1 + F_2|^2] \\
&\quad + [U_{ii}|F_5 + F_6|^2 + D_{jj}(u \leftrightarrow t)] \\
&\quad + \Theta_{ij}[2(F_1 + F_2)^*(F_5 + F_6) + (u \leftrightarrow t)] \\
u\bar{u} \to W^+ &: (trD)\delta_{ij}|F_3 + F_4|^2 + U_{ii}|F_5 + F_6|^2 \\
&\quad + \delta_{ij}2U_{ii}(F_3 + F_4)^*(F_5 + F_6) \qquad (2.85) \\
uu \to W^+ &: [U_{ii}|F_5 + F_6|^2 + U_{jj}(u \leftrightarrow t)] + \delta_{ij}U_{ii}2(H_1 + H_2)^*(H_7 + H_8) \\
ud \to W^+ &: U_{ii}|F_5 + F_6|^2 + \frac{1}{2}\Theta_{ij}2(H_1 + H_2)^*(H_5 + H_6) \\
ug \to W^+ &: U_{ii}[(qg \to q\gamma^*) + (qg \to qg\gamma^*)] \\
gg \to W^+ &: (trD)(gg \to q\bar{q}\gamma^*).
\end{aligned}
$$

In (2.85) the F's and H's refer to the Feynman diagrams in figures 2.9 and 2.10. To complete the construction for W^+-production, symmetries are invoked. Weak interactions in general violate both C and P invariance but to a good approximation maintain CP invariance. This means that weak interactions are invariant under simultaneous particle $\leftrightarrow$ antiparticle and $\lambda \leftrightarrow -\lambda$ transformations, where λ is the particle helicity. This, together with isospin and a 180 degree rotation of the plane of the W and the beam, requires the following addition to (2.85) :

$$u \leftrightarrow \bar{d}, d \leftrightarrow \bar{u}, \Theta \leftrightarrow \Theta^T, U \leftrightarrow D. \qquad (2.86)$$

This completes the expression for W^+-production.

The structure function combinations for the different processes in (2.85), where the quark labels for the different contributions are generic labels, are presented here. For instance,

$$u\bar{d} \equiv u\bar{d} + u\bar{s} + u\bar{b} + c\bar{d} + c\bar{s} + c\bar{b}. \qquad (2.87)$$

The symmetry relations described above increase this combination with terms of

the type

$$\bar{d}u + \bar{d}c + \cdots \tag{2.88}$$

Those processes that are prefixed by a δ_{ij} are convoluted with quark and anti-quark distributions from within the same family.

The Couplings, Matrix Element Structure and Parton Combinations for Z Production.

The Z-fermion coupling is

$$\frac{e}{2\sqrt{2}sin\theta_W} Z_\mu \bar{f}\gamma^\mu(v_f - a_f\gamma_5)f. \tag{2.89}$$

In this case the vectorial and axial couplings are different and are defined by

$$\begin{aligned} g^{(V)} &= \left(\frac{m_W^2}{4M_Z^2}\right)^{\frac{1}{2}}(\tau_3 - 4e_f sin^2\theta_W), \\ g^{(A)} &= \left(\frac{m_W^2}{4M_Z^2}\right)^{\frac{1}{2}}\tau_3. \end{aligned} \tag{2.90}$$

These couplings require the definition of the τ_3 and e_f for the relevant fermions. In this case it is the inclusive cross-section that is being studied and so the relevant fermion-Z couplings are those for the u and d quarks. $\tau_3 = 1, -1$ for the u and d quarks respectively.

Following Arnold and Reno, it is useful to define the quantity:

$$\begin{aligned} \mathcal{F}_{ab}^{\pm} =& [g_a^2|F_5 + F_6|^2 + g_b^2(u \leftrightarrow t)] \\ & \pm g_a^{(V)} g_b^{(V)} 2(F_5^{(V)} + F_6^{(V)})^*(F_7^{(V)} + F_8^{(V)}) \\ & + g_a^{(A)} g_b^{(A)} 2(F_5^{(A)} + F_6^{(A)})^*(F_7^{(A)} + F_8^{(A)}). \end{aligned} \tag{2.91}$$

The structure of the matrix element combinations are

$$
\begin{aligned}
u\bar{d} \to Z &: \mathcal{F}^{+}_{ud} \\
u\bar{u} \to Z &: \delta_{ij}[(q\bar{q} \to g\gamma^*) + (q\bar{q} \to gg\gamma^*) + 2T_R|F_1 + F_2|^2] \\
&\quad + \delta_{ij} g_u^2[2(F_1 + F_2)^*(F_5 + F_6) + 2(F_3 + F_4)^*(F_5 + F_6) + (u \leftrightarrow t)] \\
&\quad + \delta_{ij}(N_u g_u^2 + N_d g_d^2)|F_3 + F_4|^2 + \mathcal{F}^{+}_{uu} \\
ud \to Z &: \mathcal{F}^{-}_{ud} \\
uu \to Z &: \frac{1}{2}\delta_{ij} g_u^2[2(H_1 + H_2)^*(H_5 + H_6) + 2(H_1 + H_2)^*(H_7 + H_8) + (u \leftrightarrow t)] \\
&\quad + \mathcal{F}^{-}_{uu} \\
ug \to Z &: g_u^2[(qg \to q\gamma^*) + (qg \to qg\gamma^*)] \\
gg \to Z &: (N_u g_u^2 + N_d g_d^2)(gg \to q\bar{q}\gamma^*).
\end{aligned}
\tag{2.92}
$$

In this expression $N_{u,d}$ are the number of up and down type flavours used in the calculation.

Once again the parton combinations must be saturated to include all possibilities for Z production. This leads to the following additions to the expression above:

$$
\begin{aligned}
&1.\ u \leftrightarrow d, \\
&2.\ u \leftrightarrow \bar{u},\ d \leftrightarrow \bar{d}.
\end{aligned}
\tag{2.93}
$$

To obtain the final inclusive cross-section, these expressions are folded into the kinematics and the remaining phase space integrals. These are described in section 2.4.

2.4 Kinematics and Integration Techniques.

This is a study of the inclusive process

$$p + \bar{p} \to W^{\pm}(Z^0) + X \tag{2.94}$$

up to $O(\alpha_s^2)$. To this order the intermediate vector boson is accompanied by one or two jets. The invariant mass of the two jet system in the latter case is defined

in (2.60) and can be rewritten as

$$s_2 = x_1 x_2 S + x_1 T + (1 - x_1) m_W^2 x_2 U + (1 - x_2) m_W^2 - m_W^2, \tag{2.95}$$

where the definitions of the partonic variables have been used. By simple rearrangement this gives the following expression for x_2:

$$x_2 = \frac{s_2 - m_W^2 - x_1(T - m_W^2)}{x_1 S + U - m_W^2} \leq 1. \tag{2.96}$$

A change in integration variable from x_2 to s_2 in the general expression for the cross-section ((2.47)) may be performed here with the Jacobian

$$\frac{1}{x_1 S + U - m_W^2}, \tag{2.97}$$

and lower integration limit

$$A = U + x_1(S + T - m_W^2) \geq 0. \tag{2.98}$$

This makes the lower limit for the x_1 integration as

$$B = \frac{-U}{S + T - m_W^2}. \tag{2.99}$$

This effectively completes the requirements for the calculation of the differential cross-section

$$\frac{d\sigma}{dp_T^2 dy} = \int_B^1 dx_1 \int_A^1 ds_2 \frac{1}{(x_1 S + U - m_W^2)} s \frac{d\sigma_{a,b}}{dtdu}(x_1, x_2) G_{a/A}(x_1, M^2) G_{b/B}(x_2, M^2) \tag{2.100}$$

except for the structure functions, which will be described in the next section, and the choice of the scales, which will be described in section 2.6. For the $2 \rightarrow 2$ processes, s_2 is set to zero in (2.96).

However, to obtain a differential cross-section with respect to the transverse momentum only, one has to obtain the relevant limits for the $y-$integration. Consider a general $2 \rightarrow 2$ interaction $a + b \rightarrow c + d$. The hadronic cross-section is given by:

$$\begin{aligned}\frac{d\sigma}{dp_{Tc}^2 dy_c} &= \pi E_c \frac{d\sigma}{d^3 p_c} \\ &= \int dx_a dx_b G_{a/A}(x_a, \mu^2) G_{b/B}(x_b, \mu^2) E_c \frac{d\hat{\sigma}}{d^3 p_c} \\ &= \int dx_a dx_b G_{a/A}(x_a, \mu^2) G_{b/B}(x_b, \mu^2) \frac{s}{\pi} \delta(s + t + u - m_c^2 - m_d^2) \frac{d\hat{\sigma}}{dt},\end{aligned} \tag{2.101}$$

where $\hat{\sigma}$ is the hard process cross-section and, as usual, x_a and x_b are the momentum fractions of the interacting partons within hadrons A and B respectively. The only massive particle in this treatment is the vector boson and so m_d^2 is set to zero. The rapidity of the boson is defined by

$$y_c = \frac{1}{2} \ln \left[\frac{E_c + p_{Lc}}{E_c - p_{Lc}} \right], \tag{2.102}$$

where E_c and p_{Lc} are the energy and longitudinal momentum of the vector boson, respectively. The 4-momentum, c, may be written in the form

$$c = (\mathbf{p_T^c}, m_T^c \sinh y_c; m_T^c \cosh y_c), \tag{2.103}$$

where $m_T = \sqrt{p_T^2 + m^2}$ is the transverse mass. It is possible to restate the partonic variables s, t, and u in terms of the transverse momentum, rapidity, hadronic variables and momentum fractions. Then, by performing the x_b integral, and using the condition $x_{a,b} \leq 1$, the limits of the rapidity integration are easily obtained. For the $2 \rightarrow 3$ process, where $s_2 \neq 0$, the δ-function above is replaced by a θ-function and the number of integrals is increased by one.

The integrals were performed numerically with the integration package VEGAS [22], which uses Monte-Carlo techniques. The package requires several passes through the Monte-Carlo procedure because of a sophisticated redefinition of the grid to increase the efficiency of the integration.

There are several advantages in using such a package. For instance, it is possible by suitable programming to mimic the experimental set-up (for the measurement of a particular quantity) in the theoretical calculation and thereby match the calculation as closely as possible with the experimental measurement of the quantity being calculated. A good example of this is the imposition of cuts in calculations to match the efficiency and triggering of experiments.

In addition, matrix elements for higher-order processes are generally very long and complicated and quite often not susceptible to reduction in size and complexity. It is then quite suitable to leave the expression in an unreduced form and then to number-crunch with a package like VEGAS. This is particularly true in the case of the calculation of helicity amplitudes using spinor techniques [23,24].

2.5 The MRS Structure Functions

One source of theoretical uncertainty in these calculations concerns the choice of parton distributions. In this study the recent parametrisations of Martin, Roberts and Stirling [12] have been used.

These sets of parton distributions have been obtained by a next-to-leading-order structure function analysis of deep inelastic scattering data, which can now be measured with high precision. These measurements are a good test of QCD and provide a means of making precise measurements of the scale parameter, Λ_{QCD}. In addition, they allow an accurate determination of the parton distribution functions. Martin *et al.* [12] analyse the data directly in terms of the $\ln Q^2$ dependence of the parton distributions. This dependence is defined by the Altarelli-Parisi equations, including the next-to-leading order corrections.

The quark distribution functions may be determined directly from a measurement of deep inelastic scattering cross-sections, but not the gluon distribution function. This quantity enters the picture indirectly, via the singlet (under $SU(N_f)$) structure function evolution equation and this represents some freedom of choice, loosely constrained by theory. To represent this uncertainty, the MRS

structure function sets include various gluon parametrisations. These were obtained from several equally acceptable fits to deep inelastic scattering data and are described below.

The non-singlet calculation of $W, Z-$production to $O(\alpha_s^2)$ has been performed with the earlier sets of MRS structure functions, called MRS1,2 and 3. These sets correspond to different values for Λ_{QCD} and different forms for the gluon parametrisation:

$$\begin{aligned} set1 &: \Lambda_{QCD} = 107MeV \; - \text{ soft gluon} \\ set2 &: \Lambda_{QCD} = 250MeV \; - \text{ hard gluon} \\ set3 &: \Lambda_{QCD} = 178MeV \; - \frac{1}{\sqrt{x}} \text{ gluon.} \end{aligned} \tag{2.104}$$

Sets 1 and 2 are analogous to the earlier parametrisations of Duke and Owens [25].

The complete second-order calculation, with the matrix elements of Arnold and Reno [11] was performed with the more recent MRSE′ and MRSB′ sets [26]. These sets have Λ_{QCD} =100 and 200 MeV respectively and identical soft gluon parametrisations. These structure function parametrisations are valid in the following x and Q^2 regions:

$$\begin{aligned} &10^{-4} < x < 1, \\ &5 \; GeV^2 < Q^2 < 1.31 \times 10^6 \; GeV^2. \end{aligned} \tag{2.105}$$

2.6 'Optimisation' Procedures with respect to the Choice of Scales.

Finite order perturbative QCD calculations have certain ambiguities which severely limit their predictive capabilities, especially when precision measurements are made. In this section, a description of the dependence of the differential cross-section of the process $p + \bar{p} \rightarrow W(Z) + X$ on the choice of renormalisation and factorisation schemes is presented. This is accompanied by a phenomenological description of the technique of 'optimisation', first suggested by Stevenson

[27], which, it is hoped, removes some of the theoretical ambiguity but does not solve the problem. In $O(\alpha_s^2)$ calculations in perturbative QCD renormalisation scheme dependence is introduced via the arbitrary scale, μ, in the coupling constant $\alpha_s(\mu)$, where μ has dimensions of mass. To this order, the factorisation scheme ambiguity is introduced partly by the freedom of choice that exists for the scale that characterises the structure functions, and partly by the definition of the structure functions themselves.

Three types of divergences enter QCD calculations: (i) the ultraviolet divergences from the consideration of loop diagrams, (ii) the infrared mass singularities that result from the collinear emission of gluons from the quarks in the initial channel and finally (iii) the infrared divergences that result from the collinearity between the bremsstrahlung final state boson and the parent final state quark. (iii) is regulated by the mass of the intermediate vector boson, while (i) and (ii) are handled by dimensional regularisation. The arbitrary renormalisation scale μ is introduced through the $\overline{MS}$-scheme. As we saw in section 2.2, the singularities associated with the initial state partons are factored off and this requires the introduction of the factorisation scale, M, which gives rise to scale dependent structure functions.

In the rest of this discussion the phenomenological formalism of Aurenche *et al.* [28-30], with respect to the 'optimisation' theory, is followed. Initially, it is suitable to consider only the non-singlet case. Then, the generic form of the cross-section is given by

$$\begin{aligned} E\frac{d\sigma}{d^3p} =& \frac{\alpha_s(\mu)}{\pi}\left[\hat{\sigma}_B + \frac{\alpha_s(\mu)}{\pi}\left[b\ln(\mu/\Lambda) + 2\ln(p_T/M)P_{qq}\otimes\right]\hat{\sigma}_B\right. \\ &\left. + \frac{\alpha_s(\mu)}{\pi}K_{q\bar{q}}\right] \otimes G_v(M) \otimes G_v(M) \\ =& \frac{\alpha_s(\mu)}{\pi}\sigma^{Born}\left[1 + \frac{\alpha_s(\mu)}{\pi}\tau - \frac{\alpha_s(\mu)}{\pi}\rho_1(M,\Lambda)\right], \end{aligned} \tag{2.106}$$

where $\hat{\sigma}_B$ is the hard process cross-section for the process

$$q + \bar{q} \rightarrow W(Z) + g, \tag{2.107}$$

and

$$\sigma^{Born} = \hat{\sigma} \otimes G_v(M) \otimes G_v(M). \tag{2.108}$$

The M, Λ dependent piece in (2.106) is just

$$\rho_1(M,\Lambda) = -\left[2\ln(p_T/M)P_{qq} \otimes \hat{\sigma}_B + K_{q\bar{q}}\right] \otimes G_v(M) \otimes G_v(M)/\sigma^{Born}. \quad (2.109)$$

The $A \otimes B$ indicates that these are convolution integrals. $K_{q\bar{q}}$, the higher-order correction after factorisation is finite and independent of μ and M. ρ_1 is renormalisation scheme independent and may therefore be calculated in any renormalisation scheme. (2.106), where $\tau = b\ln(\mu/\Lambda)$, demonstrates the μ dependence of the second-order cross-section.

As has been mentioned previously, $\alpha_s(\mu)$ is defined up to second order and the scale dependence of this coupling is given by the equation

$$\mu\frac{\partial a(\mu)}{\partial \mu} = -ba^2(\mu)(1 + ca(\mu)), \quad (2.110)$$

where $b \equiv \beta_0/2$ and $c \equiv \beta_1/4\beta_0$ and

$$a(\mu) = \frac{\alpha_s(\mu)}{\pi}. \quad (2.111)$$

The solution of this equation requires a constant of integration, Λ, and is

$$\tau = \frac{1}{a(\mu)} + c\ln\frac{ba(\mu)}{2(1 + ca(\mu))}. \quad (2.112)$$

The renormalisation scale dependence of the second-order cross-section can now be fully expressed in terms of $a(\mu)$. Although it is reasonable to set $\mu \sim O(p_T)$ to prevent large logarithms of the form $\ln(\mu/p_T)$ from appearing, QCD perturbation theory does not specify a value for μ. If $\mu \to \mu'$ then the cross-section is corrected by terms that are of order $a^3(\mu)$. This is demonstrated in the evolution equation for a:

$$a(\mu') = a(\mu) + b\ln(\mu/\mu')a^2(\mu) + O(a^3). \quad (2.113)$$

In the next chapter, the phenomenology of this optimisation is presented and it will be seen that the dependence of the second-order cross-section on

μ is approximately parabolic. If the factorisation scale is kept fixed at some suitable value, this parabolic relationship provides the opportunity of locating a renormalisation scale that satisfies the condition

$$\mu \frac{\partial \sigma^{(2)}}{\partial \mu} \simeq \frac{\partial \sigma^{(2)}}{\partial a(\mu)} = 0. \tag{2.114}$$

This point on the $\sigma^{(2)} - \mu$ curve specifies the $PMS-$scale (or Principle of Minimum Sensitivity scale). This scale has some theoretical appeal because the perturbation series to all orders must be scale independent and for the second-order cross-section, this point on the graph most satisfies this condition. The other scale that is sometimes chosen is that denoted by the name 'fastest apparent convergence' (or FAC) scale, and is defined as the scale that sets the higher order contribution to zero. On the $\sigma^{(2)}$-μ curve it is the scale at which the first-order curve intersects with the first+second-order curve.

By substituting the expression for the second-order cross-section into (2.114) the following transcendental equation is obtained:

$$1 + ca \ln \frac{ba}{2(1+ca)} + \frac{ca}{2(1+ca)} = a\rho_1(M, \Lambda). \tag{2.115}$$

This equation is solved numerically for $a = a'(M)$ for fixed M, p_T, x_T and y. In (2.115) ρ_1, b and c are renormalisation scheme independent and therefore so is a'. It is then possible to express the renormalisation scheme independent second-order cross-section as

$$\sigma^{(2)}_{opt} = a'(M)\sigma^{Born}\left(1 - \frac{ca'(M)}{2(1+ca'(M))}\right). \tag{2.116}$$

The factorisation scale dependence of the cross-section remains. This is dealt with in a similar fashion. The definitions for the distribution functions and the short and long scale parts are given in section 2.2. Performing the change $M \to M'$, the correction factor that follows is at least of order a^3. This may be

verified by observing that the G_v dependence is given by [31]

$$G_v(M') = G_v(M) + a(M)\ln(M/M')P_{qq} \otimes G_v(M) + O(a^2) \qquad (2.117)$$

and by noting the general M-independence of the higher-order $a^2 K_{qq}$. Again the condition for 'optimisation' is defined by

$$M\frac{\partial\sigma^{(2)}}{\partial M}\bigg|_{M=M_{opt}} = 0, \qquad (2.118)$$

and again this is solved numerically. Aurenche *et al.* [28] show that the 'optimum' point, at which the cross-section is determined, is a saddle point of an approximately hyperbolic surface, spanned by $\sigma^{(2)}$ when it is plotted as a function of μ and M.

The previous discussion is restricted to the non-singlet sector. In the singlet sector both quarks and gluons are admitted in the initial channel. In principle, each sector should be optimised separately and this is described by Aurenche *et al.* [28]. However, if the whole of $\sigma^{(2)}$ is optimised, they estimate the introduced error to be less than 10%.

2.7 Numerical calculations - non-singlet $O(\alpha_s^2)$ calculation

Chronologically, this calculation was performed in two parts. The first part was performed with the non-singlet matrix elements of Ellis, Martinelli and Petronzio [10] and this is presented first. The $O(\alpha_s)$ cross-sections have also been calculated by Ellis and Stirling [32] and the integration limits, matrix-elements and structure function combinations for this calculation were checked numerically against those of the former (for the $2 \to 2$ case).

The contribution of the $O(\alpha_s^2)$ diagrams to the cross-section is scale dependent and in the first case, to obtain a feel for this contribution, the scales are set at

$$\mu = M = p_T^W, \qquad (2.119)$$

and unless otherwise stated, the rest of the calculation is performed with $\mu = M$.

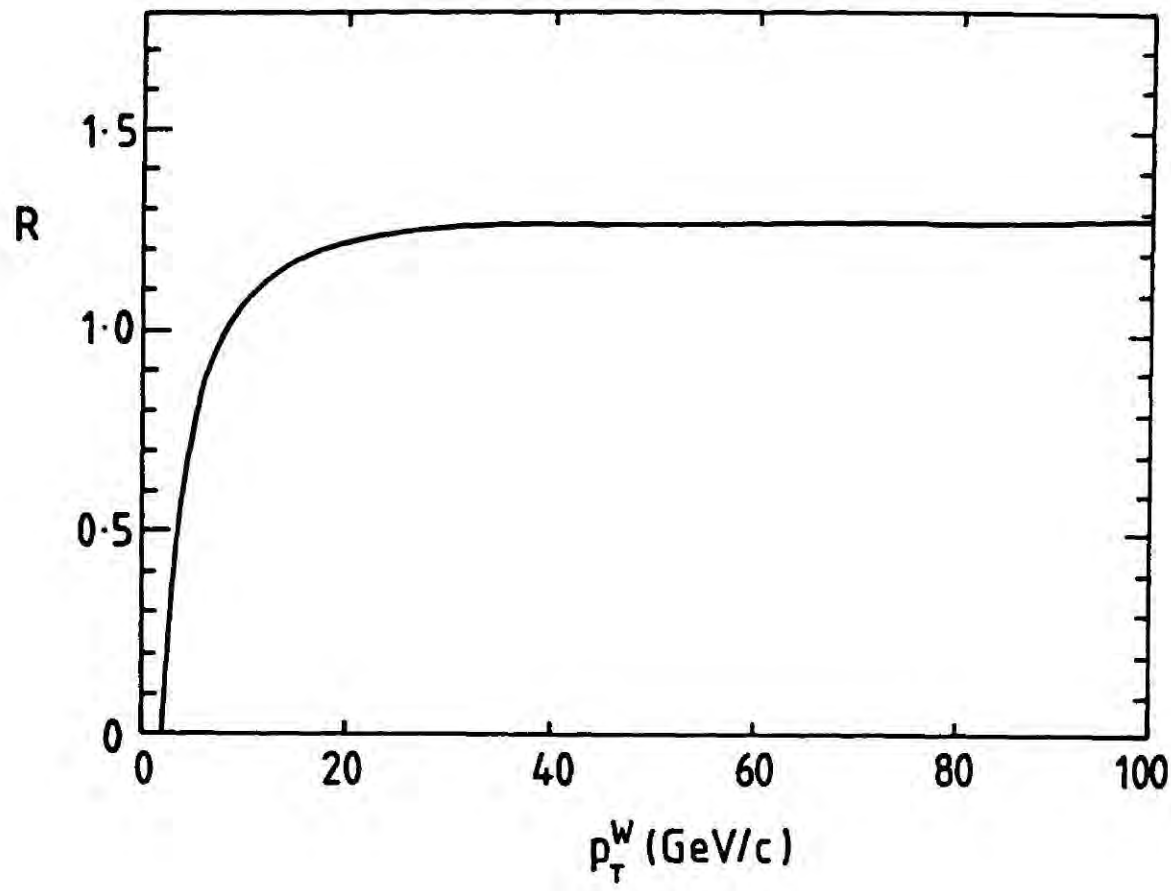

Figure 2.12 Ratio of the $O(\alpha_s^2)$ corrected to the $O(\alpha_s)$ uncorrected transverse momentum distribution for the non-singlet part of the $p + \bar{p} \rightarrow W + X$ cross-section at $\sqrt{S} = 630$ GeV The QCD scale is $Q = p_T^W$ and MRS1 structure functions are used.

The ratio

$$R = \frac{(d\sigma/dp_T^W)_{O(\alpha_s^2)}}{(d\sigma/dp_T^W)_{O(\alpha_s)}}, \tag{2.120}$$

is presented in figure 2.12 and we see that for $p_T^W > 20\,GeV/c$ the second-order contribution is constant at $\simeq 30\%$.

Since these matrix elements are restricted only to the nonsinglet sector, some assumption has to be made about the contribution of the singlet sector at $O(\alpha_s^2)$. An estimate of this uncertainty may be obtained by determining the contribution of the singlet sector to the $O(\alpha_s)$ cross-section and then by assuming that the contribution of the singlet sector to the $O(\alpha_s^2)$ is of the same level. At the CERN energy, $\sqrt{S} = 630\,GeV$ the cross-section is dominated by the nonsinglet sector (see figure 2.13). The maximum contribution of the singlet sector occurs at

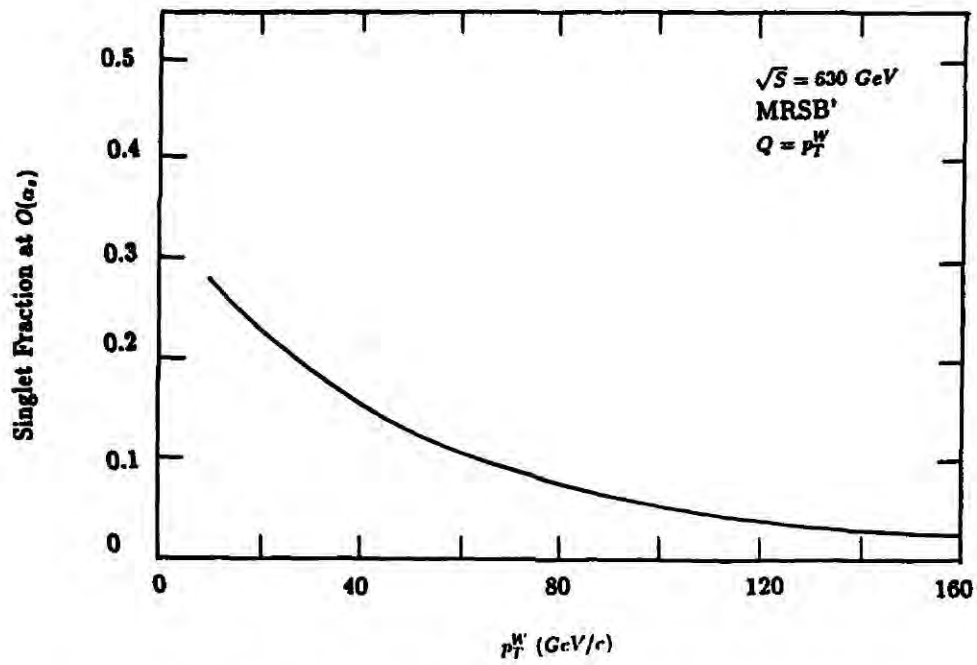

Figure 2.13 The fraction of the $O(\alpha_s)$ differential cross-section that is the singlet contribution at $\sqrt{S} = 630$ GeV with $Q = p_T^W$ and the MRSB' structure functions.

small p_T^W. This curve depends on the scale and structure functions, but these uncertainties are of the order of 15-20%. With the assumption made above, this allows us to set the theoretical uncertainty due to the non-availability of the singlet matrix elements to be of the order of 10%. This estimate of the uncertainty is larger at higher $\sqrt{S}$, since the singlet contribution to the cross-section increases with centre-of-mass energy.

The prescription for the choice of scales, as mentioned earlier, is that of 'optimisation'. However, unlike the procedure described by Aurenche *et al.* [28-30] in this study, the factorisation and renormalisation scales have been set equal to each other and a one-dimensional optimisation has been performed. The procedure was carried out for the non-singlet sector only, as this removes the need to approximate the singlet contribution to the optimisation. In their studies of prompt photon production at $p\bar{p}$ colliders, Aurenche *et al.* [28] make the point that the combined optimisation of the singlet and non-singlet sectors should produce an optimum scale that differs little from the scales obtained from the separate optimisation of these sectors. This uncertainty is very small when p_T^W is large, because (see figure 2.13) in this region (at CERN energies) the non-singlet contribution dominates.

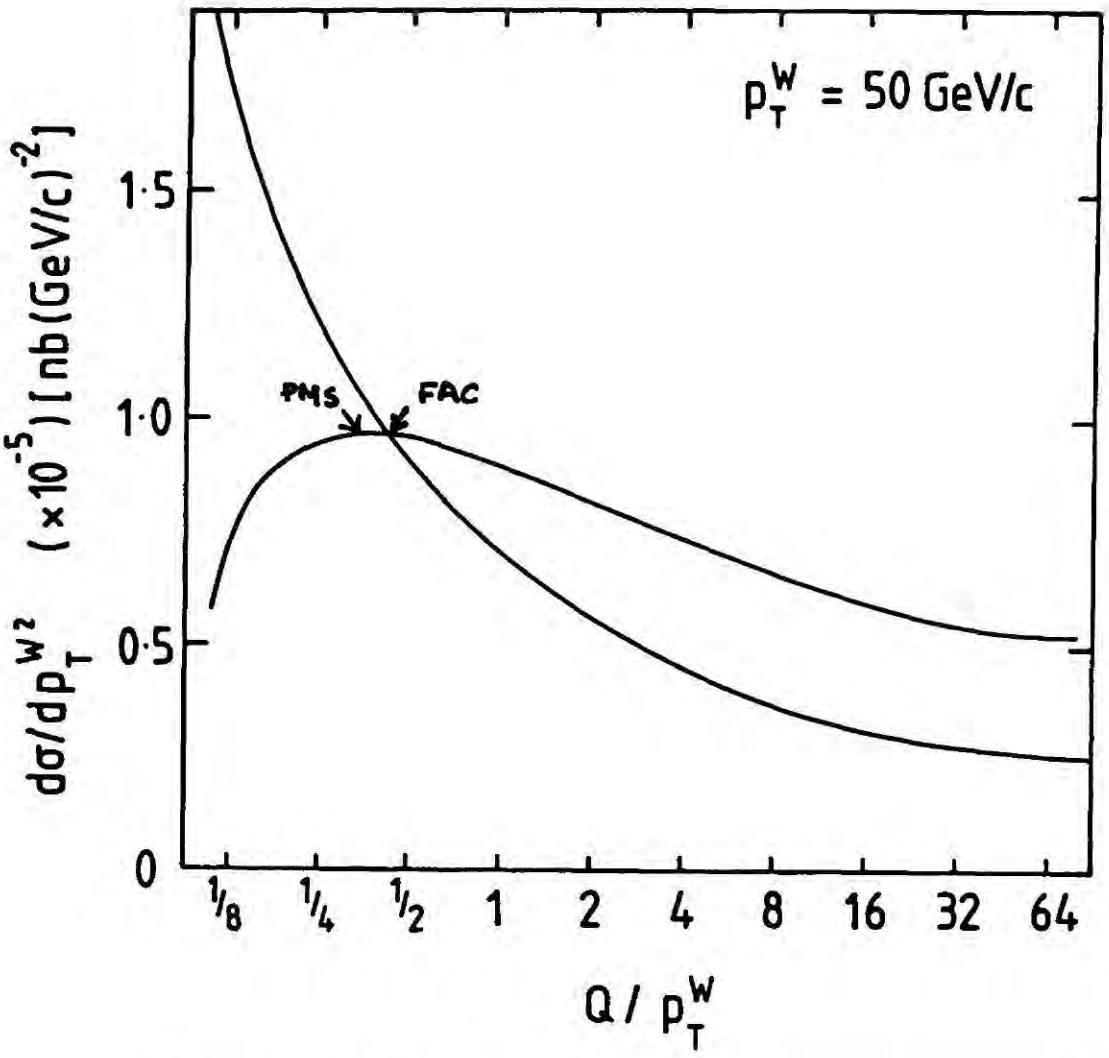

Figure 2.14 The $O(\alpha_s)$ and $O(\alpha_s^2)$ non-singlet transverse momentum distributions at p_T^W = 50 GeV/c as a function of the QCD scale. The QCD scales Q_{PMS} and Q_{FAC}, as defined in the text, are indicated.

The technique of optimisation is described here. In figure 2.14 the differential cross-section, $d\sigma/dp_T^2$, is plotted against the scale Q, which has been set to

$$Q = p_T^W \times f, \tag{2.121}$$

where $f = \frac{1}{16} \rightarrow 32$ and where $\sqrt{S} = 630\,GeV$ and $p_T^W = 50\,GeV/c$. The monotonically decreasing curve represents the $O(\alpha_s)$ non-singlet cross-section and the second curve is its $O(\alpha_s^2)$ partner. It is clear that the higher-order curve is less scale dependent than the leading-order one and this is a good sign. In addition, the next-to-leading order curve has the characteristic parabolic shape which provides two choices for the scale, Q_{PMS} and Q_{FAC}. As has been mentioned previously, Q_{FAC} is the 'fastest apparent convergence' scale and is the scale at which all higher-order contributions are forced to be zero. Q_{PMS} is more appealing

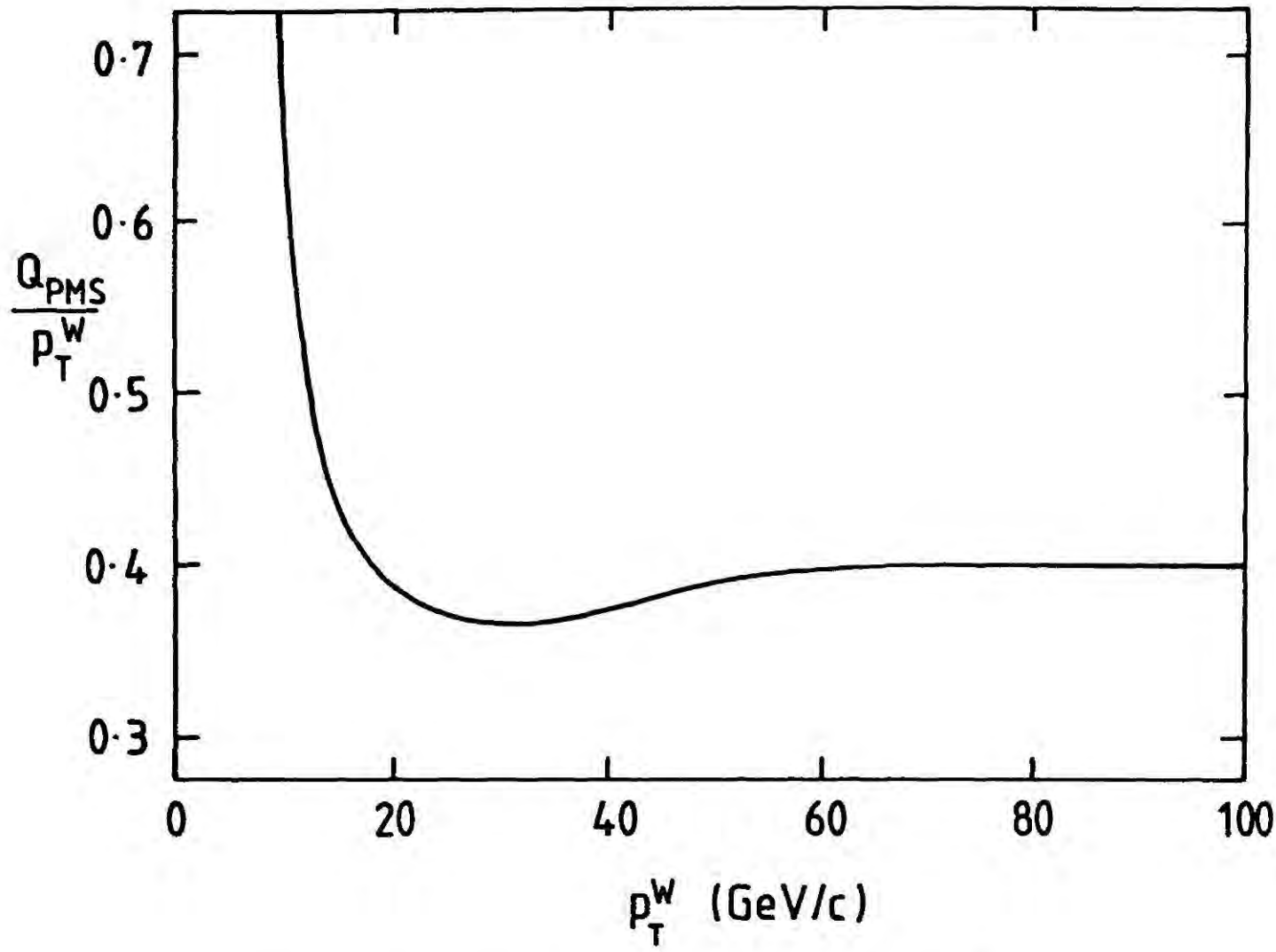

Figure 2.15 The QCD scale, as defined in the text, as a function of p_T^W.

theoretically, in the sense that any perturbation theory calculation to all orders is by definition scale independent and at $O(\alpha_s^2)$ this point on the curve represents a quantity that is scale-independent; it is the turning point of the $O(\alpha_s^2)$ cross-section. It is this scale that is used in this study. To pin down the scale further, it was necessary to repeat this calculation with a finer grid for the scale and for the set of kinematic parameters set above, and the optimised scale emerges as $Q = 0.4 p_T^W$. This procedure is repeated for different values of p_T^W. In figure 2.15, the optimised scale is plotted against p_T^W. It is clear that for $p_T^W \geq 15 GeV/c$, the optimised scale is constant at

$$Q_{opt} \simeq 0.4 \times p_T^W . \tag{2.122}$$

This flatness in the curve is a reflection of the constancy of the 'K-factor' seen in figure 2.12.

The low-p_T region is the $p_T \leq 10\,GeV/c$ region. In this region, as indicated in the introduction, there is multigluon emission and Sudakov form factors have to be taken into account. An analytic continuation to this region has been performed by Davies, Stirling and Webber [33] at $O(\alpha_s)$ and by Davies and Stirling [34] for the non-singlet sector at $O(\alpha_s^2)$.

In this study, the procedure of 'optimisation' is regarded as a prescription for choosing the renormalisation and factorisation scales. It is not claimed that this choice of scales is theoretically more correct than setting the scale to any other of the large scales that appear in the theory, such as p_T^W or m_W. However, the procedure does present a mechanism for the unambiguous definition of scales that takes into account the higher-order corrections. In addition, it provides a quantitative measure of the p_T range in which perturbative QCD holds. In figure 2.15, it is clear that for $p_T < 8$ GeV/c, perturbative QCD begins to break down.

The data presented by the UA1 [8] and UA2 [9] collaborations at CERN are in the form of the differential cross-section

$$\frac{1}{\sigma_{tot}} \frac{1}{p_T^W} \frac{d\sigma}{dp_T^W}, \tag{2.123}$$

where σ_{tot} is the total $W^{\pm}$ cross-section at $\sqrt{S} = 630\,GeV$ which corresponds to the total number of W's observed. For calculational purposes, this quantity σ_{tot} is handled differently from the differential cross-section because it is an $O(\alpha_s)$ quantity. As a function of scale it is monotonically decreasing and so cannot be optimised with respect to scale. In determining this quantity the scale is set at m_W.

The uncertainty that arises from the choice of structure functions is demonstrated by the use of the MRS1 and MRS2 sets. These differ in the value of Λ_{QCD} (107 and 250 MeV respectively) and in the gluon parametrisations. MRS2 contains a hard gluon and MRS1 a soft gluon. These provide upper and lower bounds on the uncertainty due to the structure functions.

In figure 2.16 the differential cross-section in (2.123) is plotted against p_T^W together with the 1987 data from UA1 and UA2. The final states are $e\nu$ and $\mu\nu$ for UA1 and $e\nu$ for UA2. For the reasons presented above, only data that

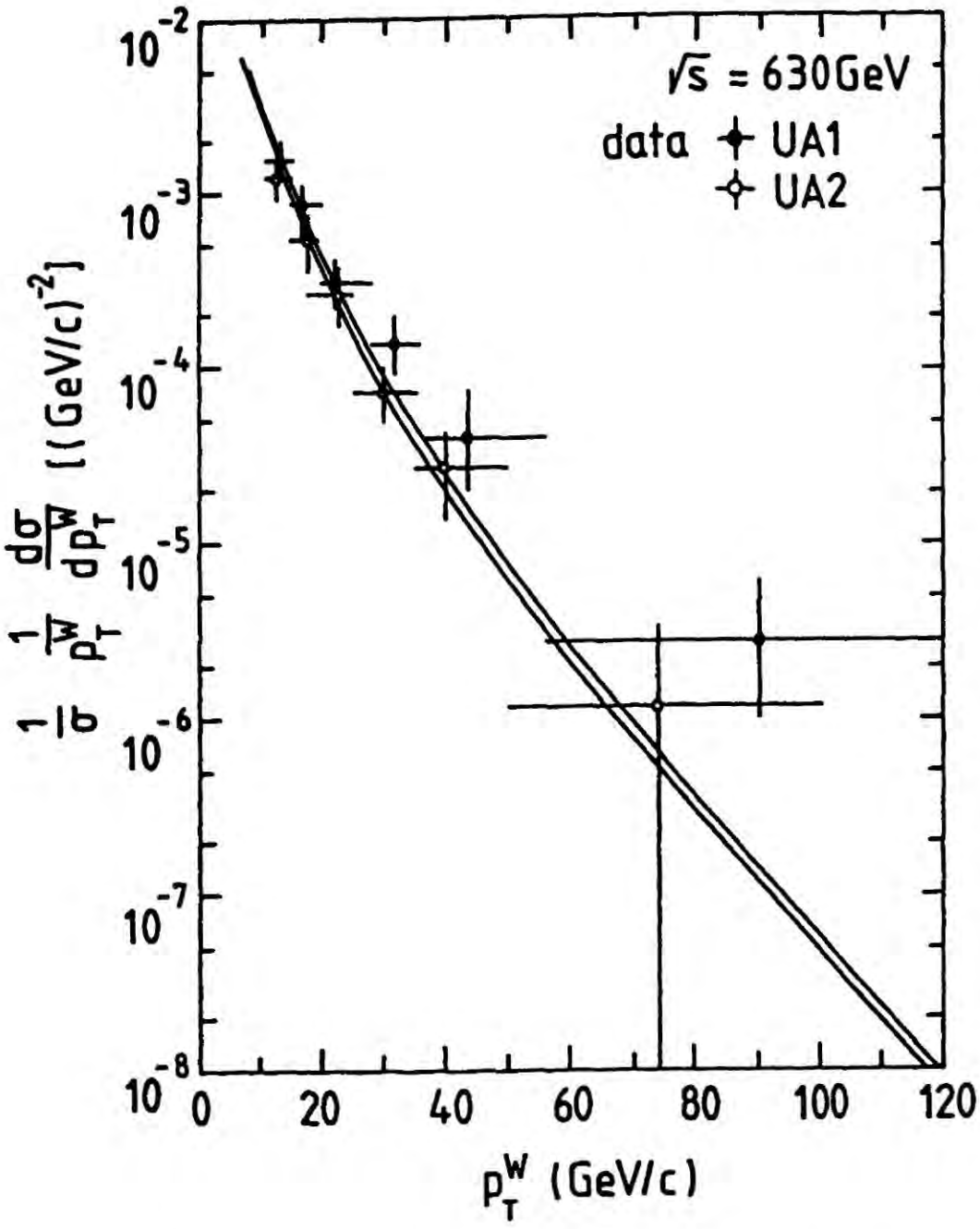

Figure 2.16 The non-singlet corrected QCD predictions for the W transverse momentum distribution in $p\bar{p}$ collisions at $\sqrt{S}$ = 630 GeV, together with the data from the UA1 and UA2 collaborations. The lower and upper curves are for the MRS1 and MRS2 structure function sets.

correspond to $p_T^W > 10\,GeV/c$ are plotted. The agreement is good over the complete range shown. At present it is clear that the data are not yet suitable for the discrimination between the two sets of parton distributions or to pin down a prediction of Λ_{QCD}. With better statistics a good test should be possible. However, the uncertainty in the measurement of p_T^W is a potential problem. It depends on the measurement of the missing transverse momentum of the neutrino and for this reason the UA2 collaboration prefers to base its measurement of p_T^W on the transverse energy carried away by the hadronic jets for their QCD analysis

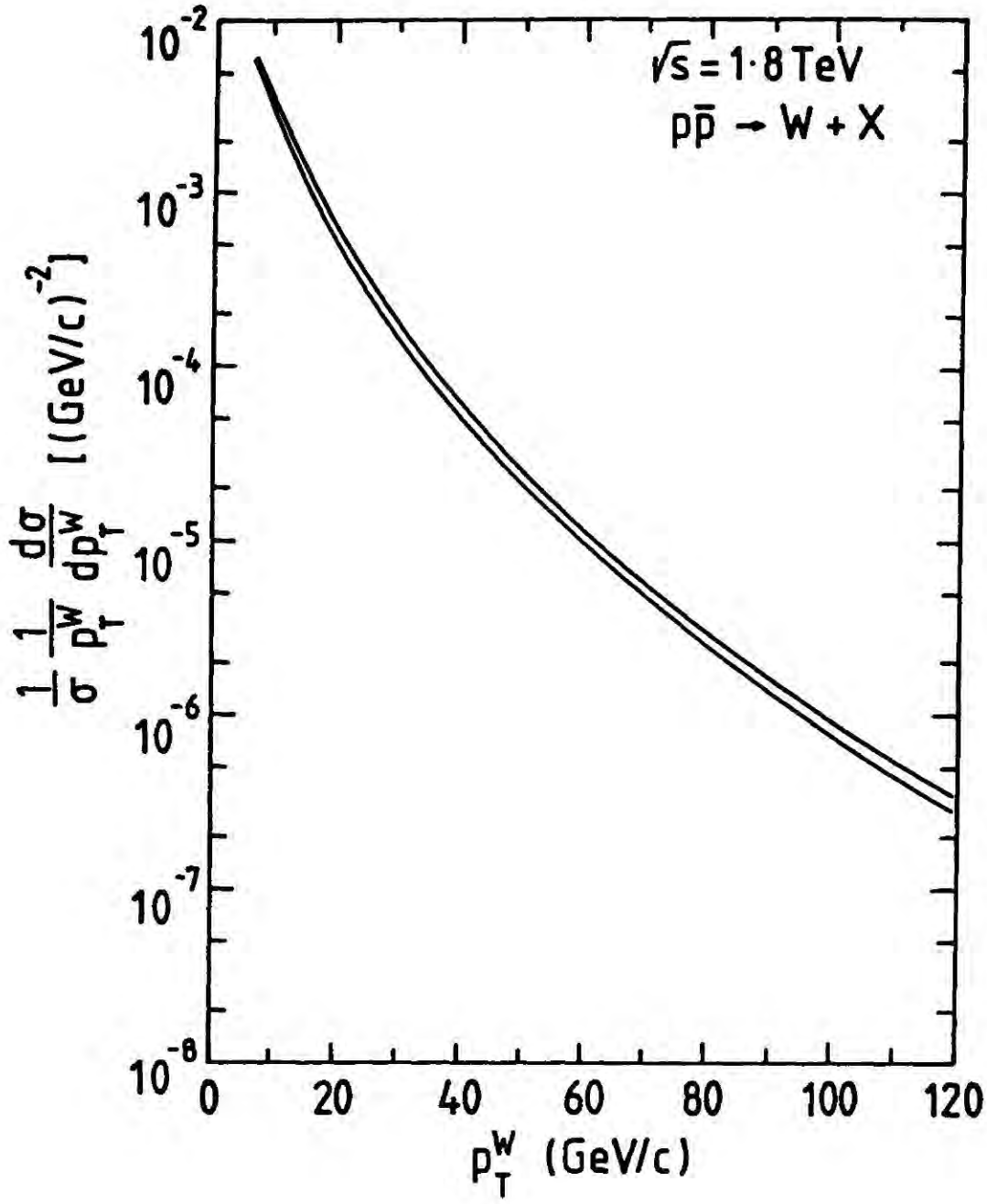

Figure 2.17 The non-singlet corrected QCD predictions for the W transverse momentum distribution at $\sqrt{S} = 1.8$ TeV. Again the upper curve relates to the MRS2 set of structure functions while the lower curve to the MRS1 set.

of W + jet events [9]. Their estimate of the error in the measurement of p_T^W is $\pm 5\,GeV/c$ over and above the errors shown on their data in figure 2.16. The prediction for the Fermilab collider at 1.8 TeV is shown in figure 2.17.

The UA1 data contain two events in the largest p_T^W bin: a muon event + 2 jets and an electron event + 2 jets. These have p_T^W significantly larger than the rest of the sample, $82 \pm 12\,GeV/c$ and $105 \pm 14\,GeV/c$, respectively. This event rate is an order of magnitude larger than the theoretical expectations. It is clear that it is no longer possible to adjust the QCD parameters to force the theoretical curve

in figure 2.16 to be much harder in the tail. The parton distributions and Λ_{QCD} are too well constrained by other processes to allow any significant variation.

More recent data has since become available and they are presented below with an update of the theoretical calculation to take into consideration the recent work of Arnold and Reno [11]. This removes the uncertainty of the singlet contribution at $O(\alpha_s^2)$ and so helps to tighten the bounds on the theoretical uncertainty.

At the time that this part of the study was performed, the UA1 and UA2 collaborations had about an order of magnitude fewer Z events and so a comparable study of the p_T^Z spectrum was not possible. The most recent runs at the CERN $Sp\bar{p}S$ collider have obtained significantly more data than the previous runs and so this situation may improve. Benchmark calculations for the CERN collider and for the Tevatron are presented in figure 2.18 for the non-singlet case at $O(\alpha_s^2)$.

2.8 Numerical calculations - complete $O(\alpha_s^2)$ calculation

When the complete $O(\alpha_s^2)$ matrix elements became available, the FORTRAN code was updated and the calculation was repeated. In this first part, the calculation and discussion is restricted to CERN energies. To obtain an indication of the contribution of the singlet sector to the $O(\alpha_s^2)$ cross-section, the scales were set, as before, to

$$\mu = M = p_T^W \tag{2.124}$$

and the quantity R, defined in (2.120), is shown in figure 2.19 as a function of p_T^W. It is clear from a comparison of this figure with figure 2.12 that the singlet contribution at $O(\alpha_s^2)$ increases the overall cross-section by approximately 10% . It must be emphasised that this effect is scale dependent.

The process of optimisation was repeated with the full set of initial state partons. In figure 2.20 the ratio μ_{opt}/p_T^W is plotted against p_T^W and it is clear that for $p_T^W > 10\,GeV/c$, the scale is constant at $0.4 \times p_T^W$. A comparison between

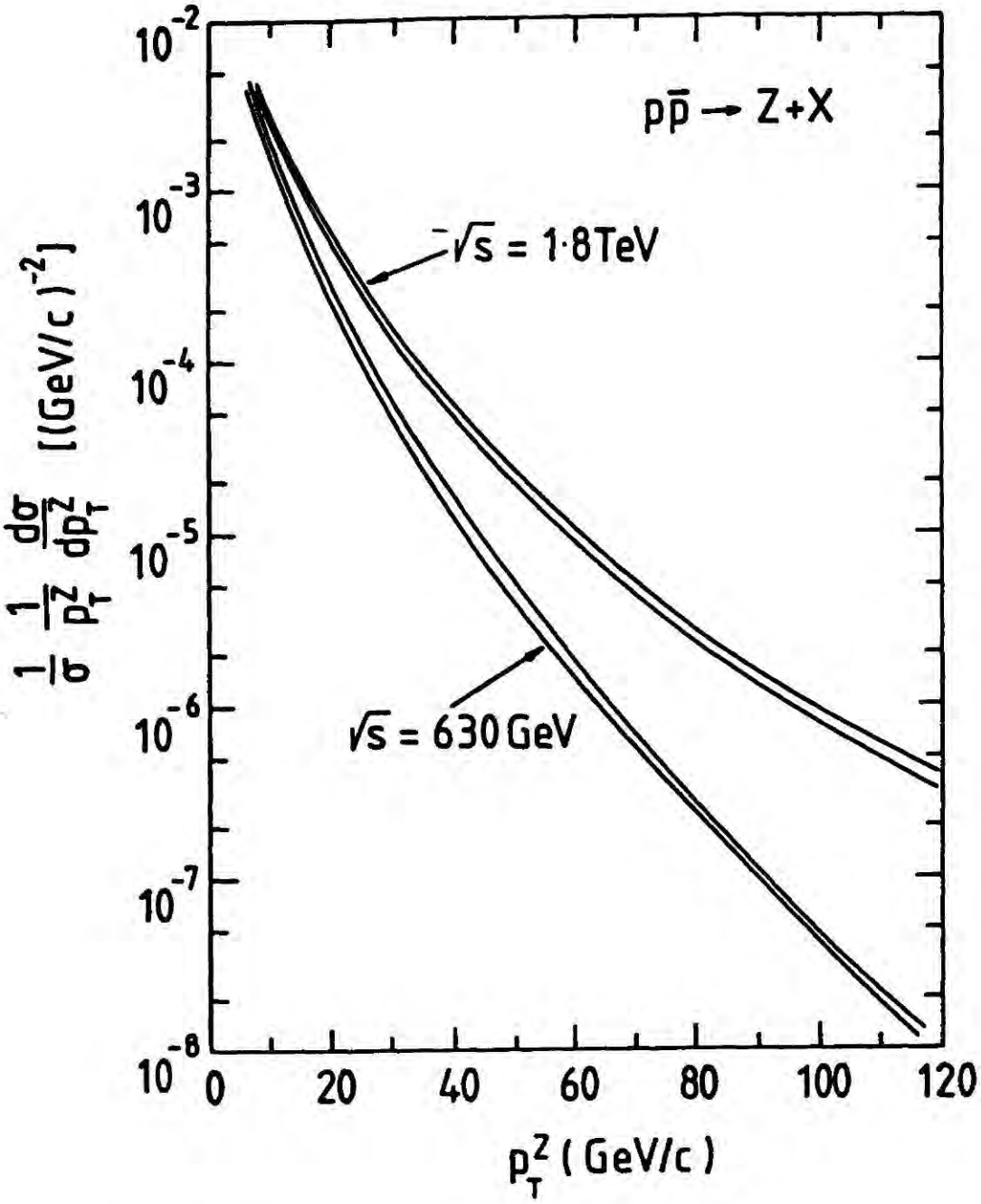

Figure 2.18 The corrected QCD predictions for the Z transverse momentum distribution in $p\bar{p}$ at $\sqrt{S} = .63$ and 1.8 TeV. The lower and upper curves are for the MRS1 and MRS2 sets of structure functions, respectively.

figure 2.15 and figure 2.20 demonstrates that the full second-order correction constrains the p_T^W dependence of the optimised scale more sharply than the non-singlet correction alone. This scale is used for the rest of the calculation.

The full second-order differential cross-section $d\sigma/dp_T^W$ differs only slightly from the partially corrected one at the optimal scale. The most recent data from UA2 [35] are shown in figure 2.21, together with the full $O(\alpha_s^2)$ theoretical prediction for the MRSB′ set of structure functions. The calculation was performed at the optimal scale. Again, there is good agreement between the theory and the

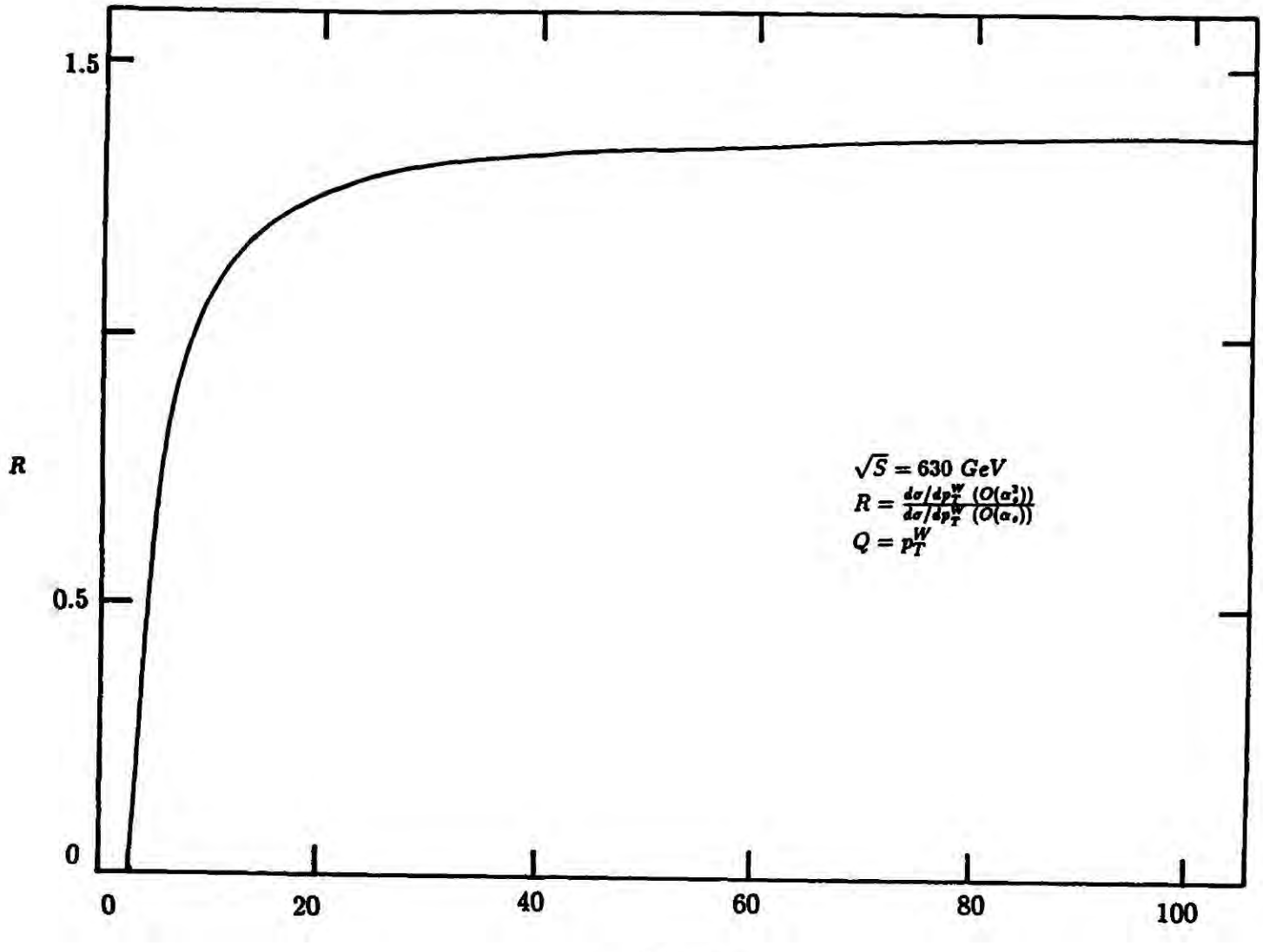

Figure 2.19 Ratio of the fully-corrected $O(\alpha_s^2)$ to the $O(\alpha_s)$ uncorrected transverse momentum distribution for the $p + \bar{p} \rightarrow W + X$ cross-section at $\sqrt{S} = 630$ GeV The QCD scale is $Q = p_T^W$ and MRS1 structure functions are used.

available data.

At $p\bar{p}$–colliders there exists an assymetry in the rapidity distributions of W^+ and W^- bosons. The rapidity distributions of W^+ and W^- produced at the CERN collider at a transverse momentum of 50 GeV/c, are plotted in figure 2.22. As expected, the summed W^+ and W^- cross-section is symmetrical about the $y = 0$ axis, while the W^+, W^- cross-sections are not. Data on this asymmetry are not yet available.

Data from the Tevatron are imminent and so predictions for the vector boson p_T-distributions at 1.8 TeV are important. The first step was to repeat the optimisation calculations that were done at the CERN energy. It turns out that at 1.8 TeV the straightforward analysis that was possible at $\sqrt{S} = 630$

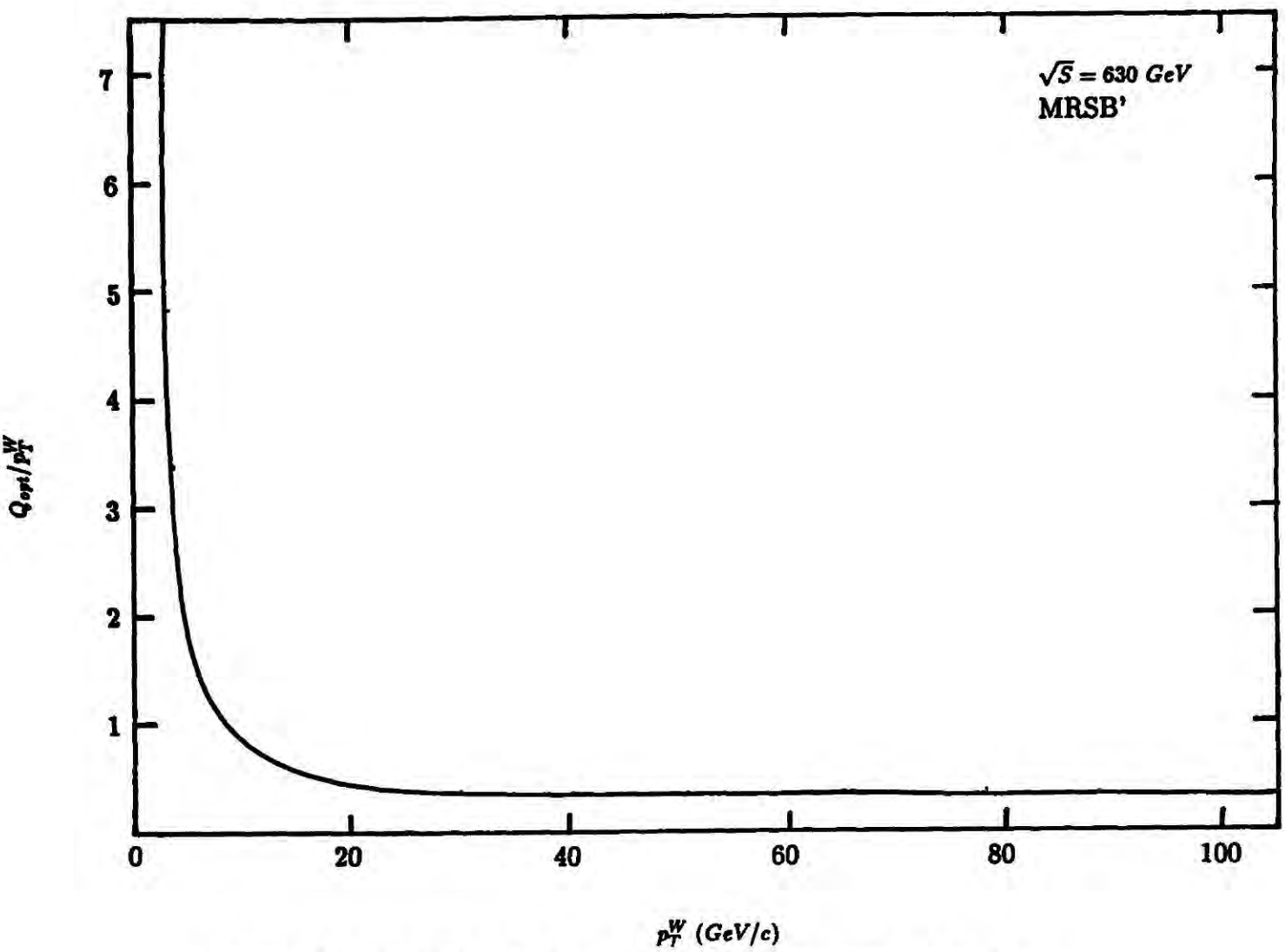

Figure 2.20 The QCD scale, Q_{PMS}, as defined in the text, as a function of p_T^W in the fully-corrected case.

GeV, was not possible. The relationship between the optimised scale and p_T^W is given in table 1 and it is clear that this relationship is qualitatively different from that at the CERN energy. The reason for this appears to stem from the numerous $\ln s_2/M^2$ terms that appear in the matrix elements. A possible solution of this problem is to calculate the cross-section at the optimum scale at each p_T^W. However, this is not feasible below an $p_T^W \simeq 60$ GeV/c since in this p_T^W range the process of optimisation takes the calculation into the non-perturbative regime. In table 1, the difference in the cross-sections calculated at the optimised scale and at p_T^W is shown and it is clear that the theoretical uncertainty is large at small p_T^W. Part of the effect at small p_T^W has to do with the fact that the optimised scale squared falls to below 5 GeV^2 and the MRS structure functions 'freeze' below this value of Q^2.

It is interesting that at $p_T^W = 65$ GeV/c there are two discernable peaks, one

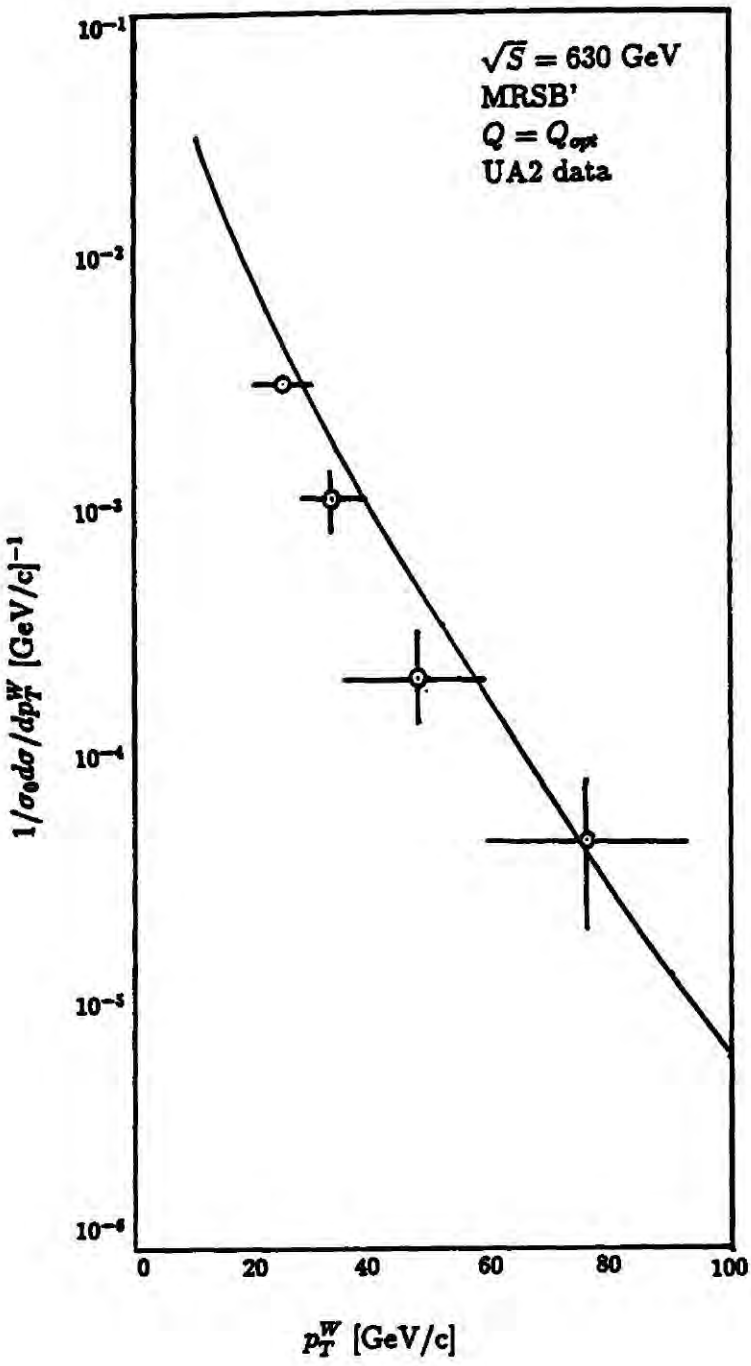

Figure 2.21 The fully-corrected QCD predictions for the W transverse momentum distribution in $p\bar{p}$ collisions at $\sqrt{S} = 630$ GeV, together with the most recent data from the UA1 and UA2 collaborations.

at $0.15 \times p_T^W$ and the other at $0.04 \times p_T^W$. At $p_T^W = 60$ GeV/c the former peak is just about washed out. Investigation of this continues.

For the purpose of making benchmark predictions for the Tevatron and the proposed 6 TeV $p\bar{p}$-collider in the Soviet Union (called UNK), the QCD scales were set at m_W and the results are plotted in figure 2.23. The theoretical uncertainty due to the arbitrariness in the choice of the scales has also been studied at $\sqrt{S} = 1.8$ TeV for the two conventional scales, m_W and p_T^W. In figure 2.24 the ratio R is plotted against p_T^W, where

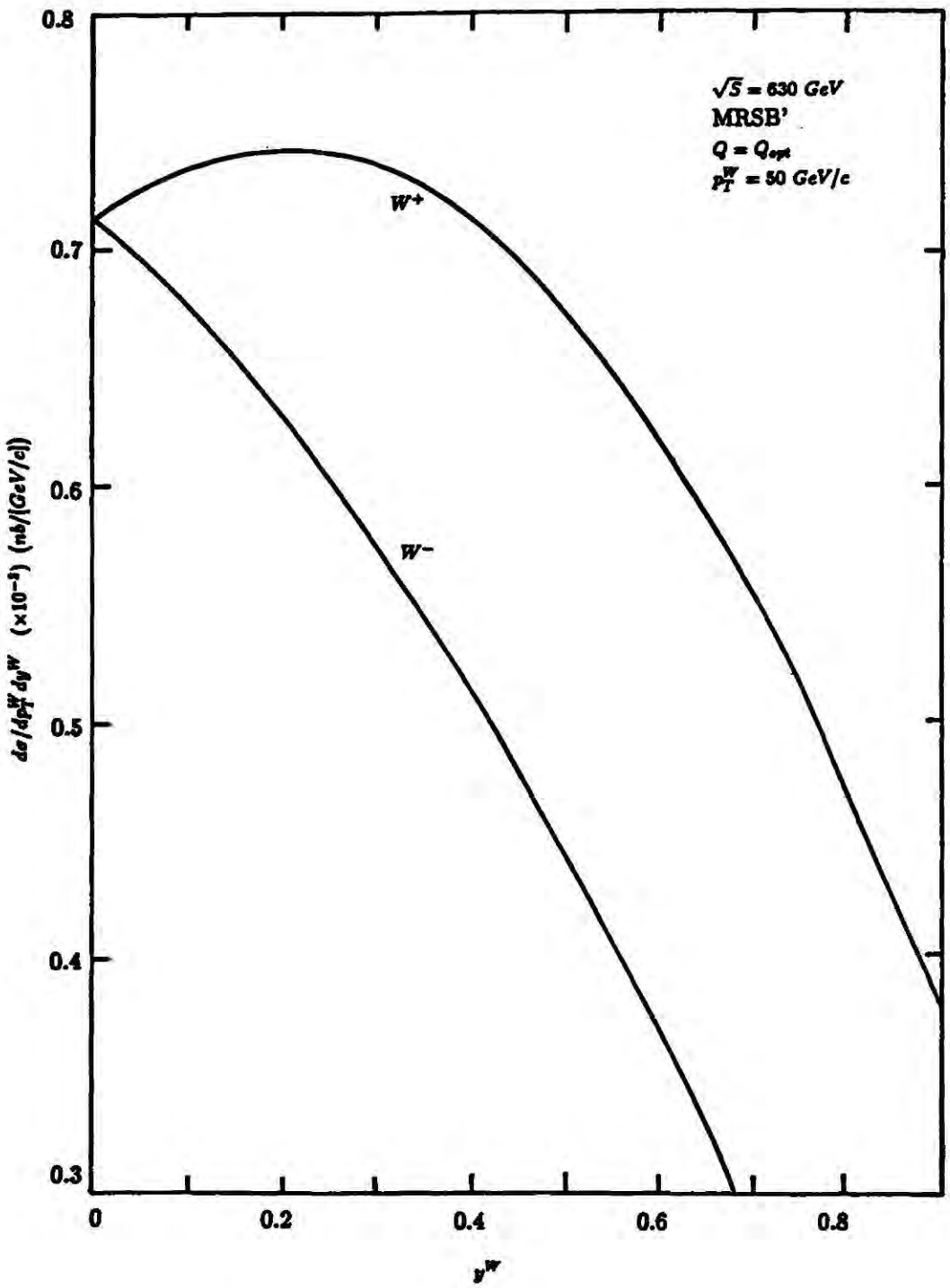

Figure 2.22 The W^+, W^- asymmtery in $p\bar{p}$ collisions.

$$R = \frac{d\sigma/dp_T^W(Q = m_W)}{d\sigma/dp_T^W(Q = p_T^W)}.$$

The structure functions used in this set of calculations are the MRSB′ set. This uncertainty due to the scales is of the order of 10%.

Since the cross-sections at $\sqrt{S} = 1.8$ TeV are particularly sensitive to the gluon content of the proton, a study was made of the dependence of these calculations on the gluon distribution function. The scale was set at the mass of the W boson for each set of structure functions. In this study, the sets chosen are the MRS1 and MRS2 sets which have been described earlier. They have the

Table 1

p_T^W	Q_{opt}/p_T^W	$Q_{opt}\,GeV$	$\frac{\sigma_{opt}-\sigma_{p_T^W}}{\sigma_{p_T^W}}$
20	0.03	0.6	0.44
30	0.03	0.9	0.41
40	0.04	1.6	0.35
50	0.04	2.0	0.30
60	0.04	2.4	0.22
70	0.15	10.5	0.14
80	0.17	13.6	0.13
90	0.20	18.0	0.12
100	0.20	20.0	0.12
120	0.23	27.6	0.11
140	0.24	33.6	0.11
160	0.28	44.8	0.11
180	0.29	52.2	0.11
200	0.29	58.0	0.11

same quark distributions but differ in their gluon parametrisations. The ratio

$$R = \frac{d\sigma/dp_T^W(MRS2)}{d\sigma/dp_T^W(MRS1)}.$$

is plotted against p_T^W and the uncertainty that arises from hard- and soft-gluon parametrisations is of the order of 20% (see figure 2.25) at Tevatron energies and is fairly constant through the p_T^W range, whereas at CERN energies, the dependence falls rapidly from 20% at low p_T^W to a few percent at large values of p_T^W. A similar study of the dependence of the differential cross-section on the new set of MRS structure functions (MRSE′ and MRSB′) indicates that the structure function dependence is smaller than 10% throughout the p_T^W range.

For completeness, two further predictions are in order. The construction of the LHC and SSC is now a real possibility. They will be pp-colliders. With the appropriate changes in the structure function combinations, benchmark predictions for the W p_T^W-spectrum are presented in figure 2.26, with $\mu = M = m_W$.

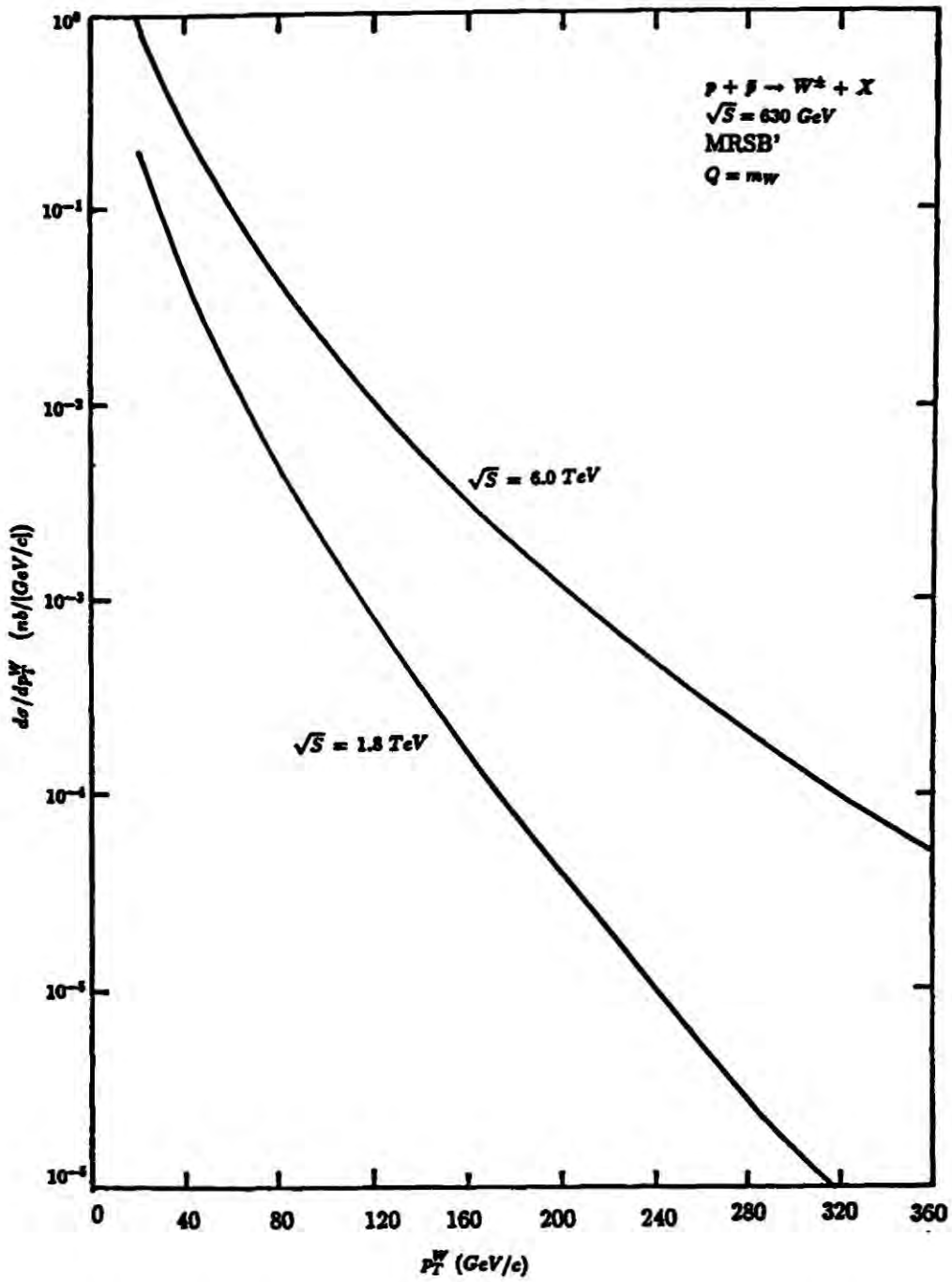

Figure 2.23 The fully-corrected $O(\alpha_s^2)$ QCD predictions for the W transverse momentum distribution in $p\bar{p}$ at $\sqrt{S} = 1.8$ and 6.0 GeV.

The full second-order theoretical predictions for the differential cross-section of neutral intermediate vector bosons have been performed as well. The prediction for the CERN collider is presented in figure 2.27 and for this calculation the scale was set at $0.4 \times p_T^Z$ and the MRSB′ set of structure functions was used. In the same figure the corresponding curve for the Tevatron is plotted but in this case the scale is set at m_Z. Unfortunately at the present time data are not available from the UA1, UA2 or CDF collaborations but with the Tevatron being a copious producer of the Z boson, spectra will become available in the near future.

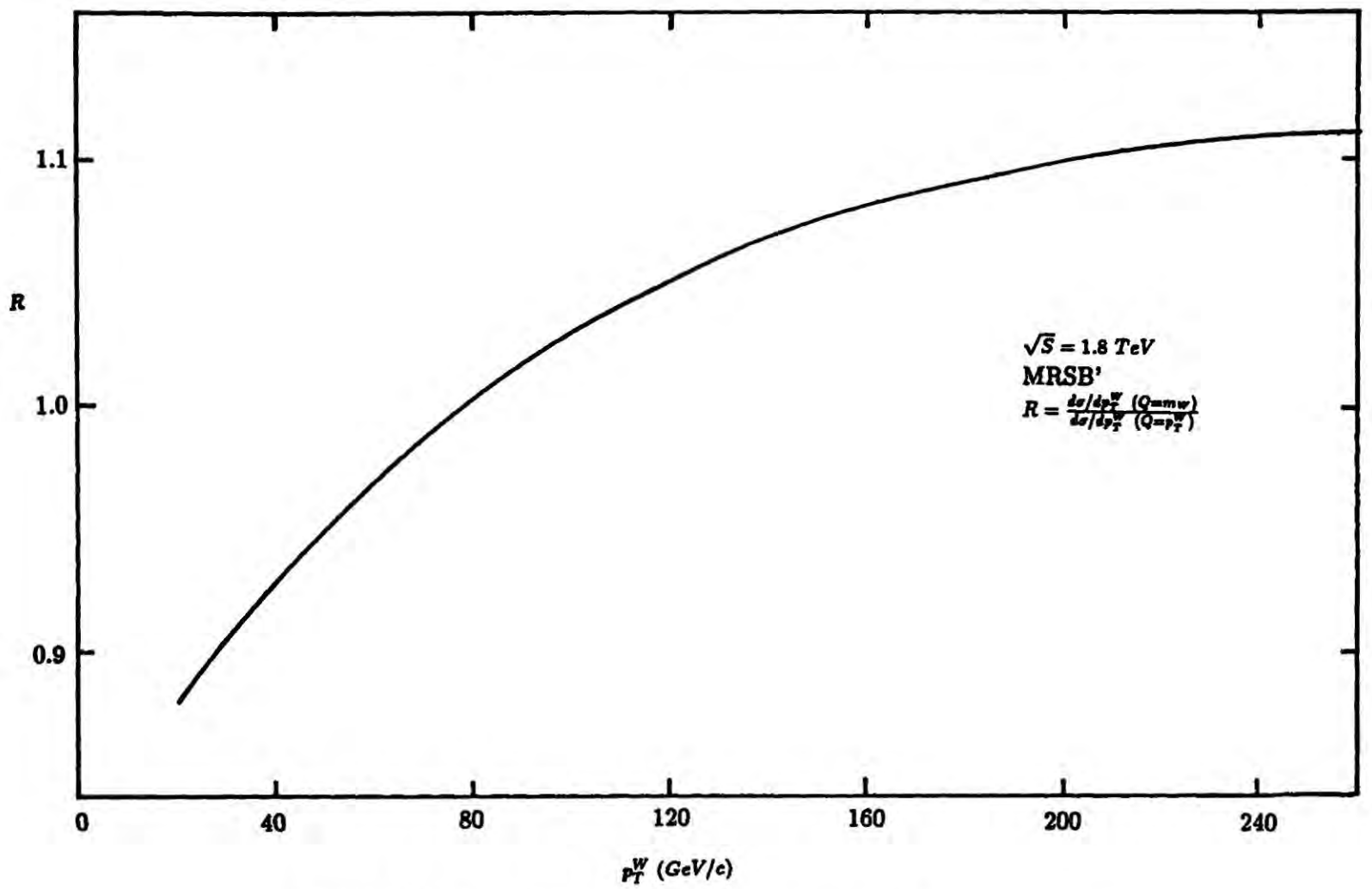

Figure 2.24 The ratio of the differential cross-section calculated with QCD scale $Q = m_W$ to that calculated at p_T^W, with the MRSB' structure functions.

Perhaps the most important aspect of this work is the potential it presents for the extraction of the gluon content of the hadron. Up to next-to-leading order, the matrix elements are known fully and the phase space integrals are performed without any tricky approximations. The gluon contribution to the differential cross-section $d\sigma/dp_T^W dy^W$ at $p_T^W = 50\,GeV/c$ is shown in figure 2.28 for $\sqrt{S} = 0.63$ and $1.8\,TeV$ as a function of the rapidity of the W boson. This indicates that at the Tevatron the gluon contribution to the differential cross-section reaches approximately 60% in certain rapidity regions. Of course, there is still significant uncertainty in the parametrisations of the sea quarks but when the gluon contribution is in the region of 60%, this uncertainty decreases in importance. This calculation is performed with the MRSB′ structure function set.

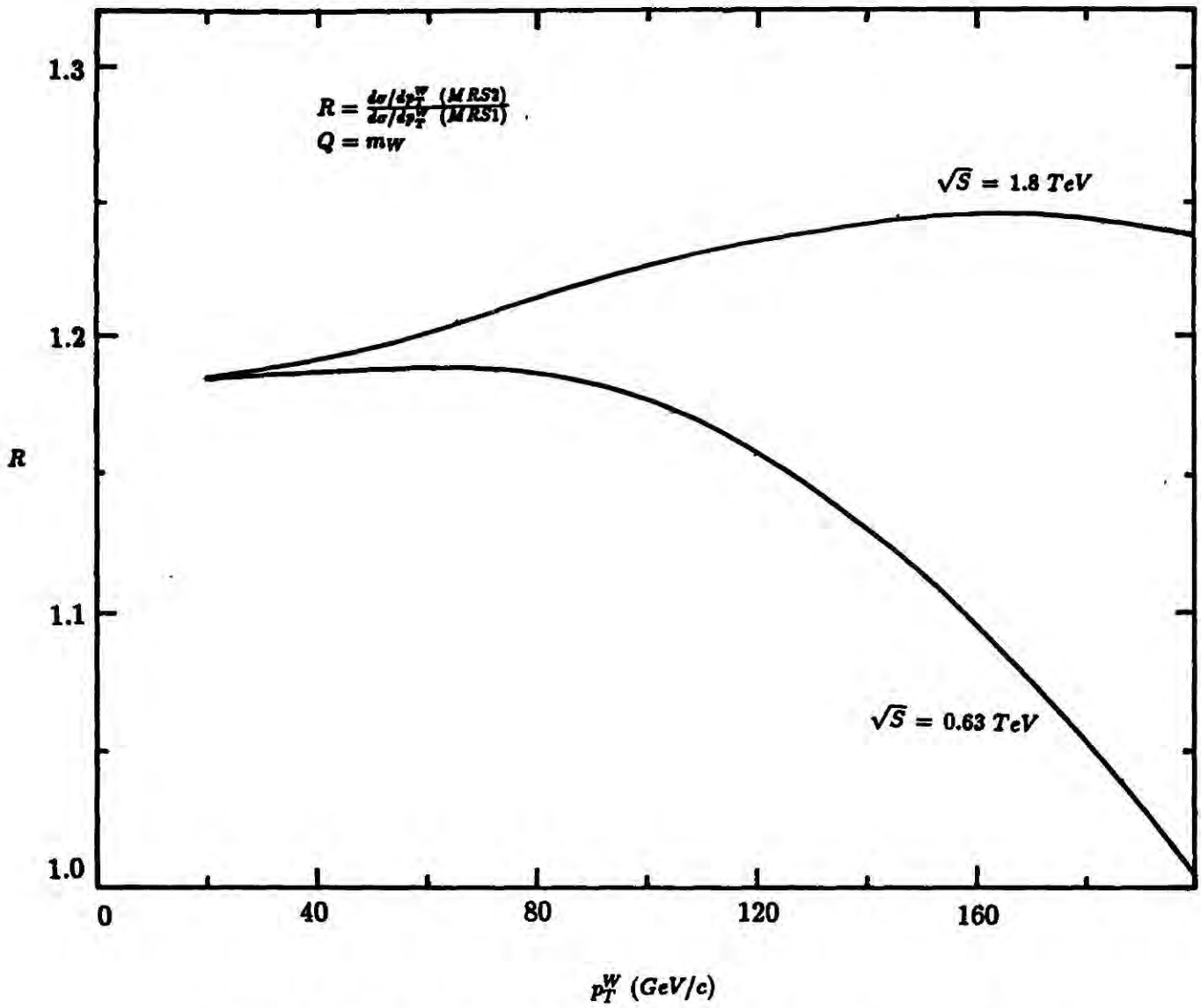

Figure 2.25 The ratio of the differential cross-section calculated with the MRS2 structure functions to that with the MRS1 set of structure functions. The QCD scale is set at $Q = m_W$.

A study of $< p_T^W >$, the average p_T^W of the W bosons produced in these $p\bar{p}$ collisions, was undertaken. The definition of this average is

$$< p_T^W >= \frac{\int_0^{p_T^{max}} d\sigma/dp_T^W \times p_T^W}{\sigma_{tot}} \tag{2.125}$$

and since the partonic differential cross-section is singular at most in $1/p_T^W \ln p_T^W$, a Monte-Carlo integration with a lower limit of $p_T^{min} = 0\,GeV/c$ is possible. The naive QCD expectation is that $< p_T^W >$ scales with $\sqrt{S}$. The general expression for the expectation value of the p_T^{W2} is given by:

$$< p_T^{W2} >= \alpha_s \times S \times f(\tau, \ln(\mu^2/m_W^2), \ln(m_W^2/\Lambda^2)) \tag{2.126}$$

where $\tau = m_W^2/S$. It is clear that this scaling relationship holds in the case of fixed τ and at leading order (where there is no μ dependence). The deviation

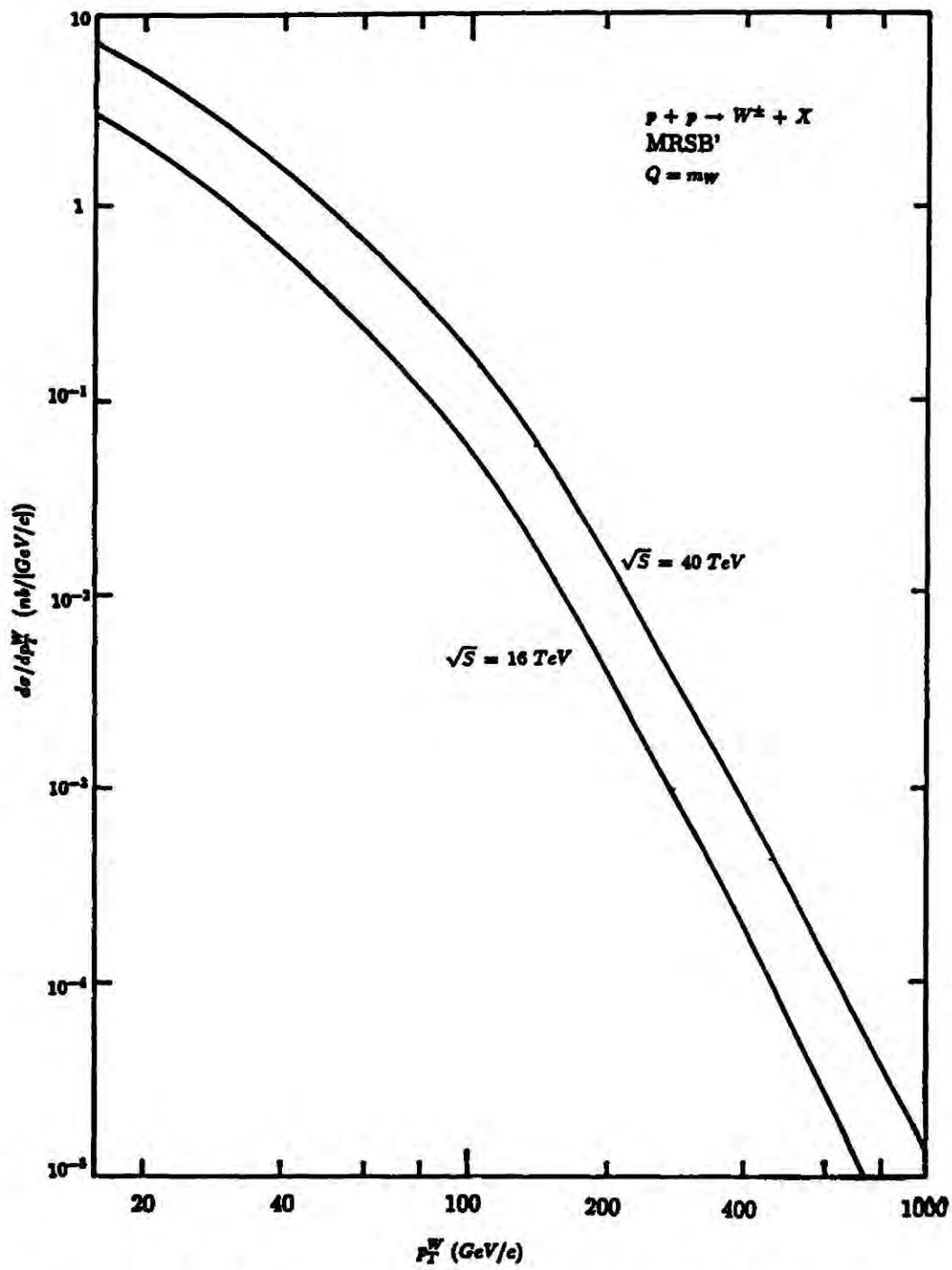

Figure 2.26 The fully-corrected $O(\alpha_s^2)$ transverse momentum distribution of W bosons produced in $pp \rightarrow W + X$ at $\sqrt{S} = 16$ and 40 TeV.

from this scaling prediction for the $O(\alpha_s^2)$ calculation (see figure 2.29) is quite startling. This curve was obtained with a newly optimised scale of $0.3 \times m_W$ and with the MRSB′ set of structure functions. Optimisation in this case is efficient at all values of $\sqrt{S}$. The calculation of $< p_T^W >$ and $< p_T^{W2} >$ are as theoretically constrained as the calculation of the differential cross-sections. The discrepancy that exists between the theoretical predictions for $< p_T^W >$ as a function of $\sqrt{S}$ and the available data (see figure 2.29) may provide a measure of the intrinsic transverse momentum of the partons within the hadrons.

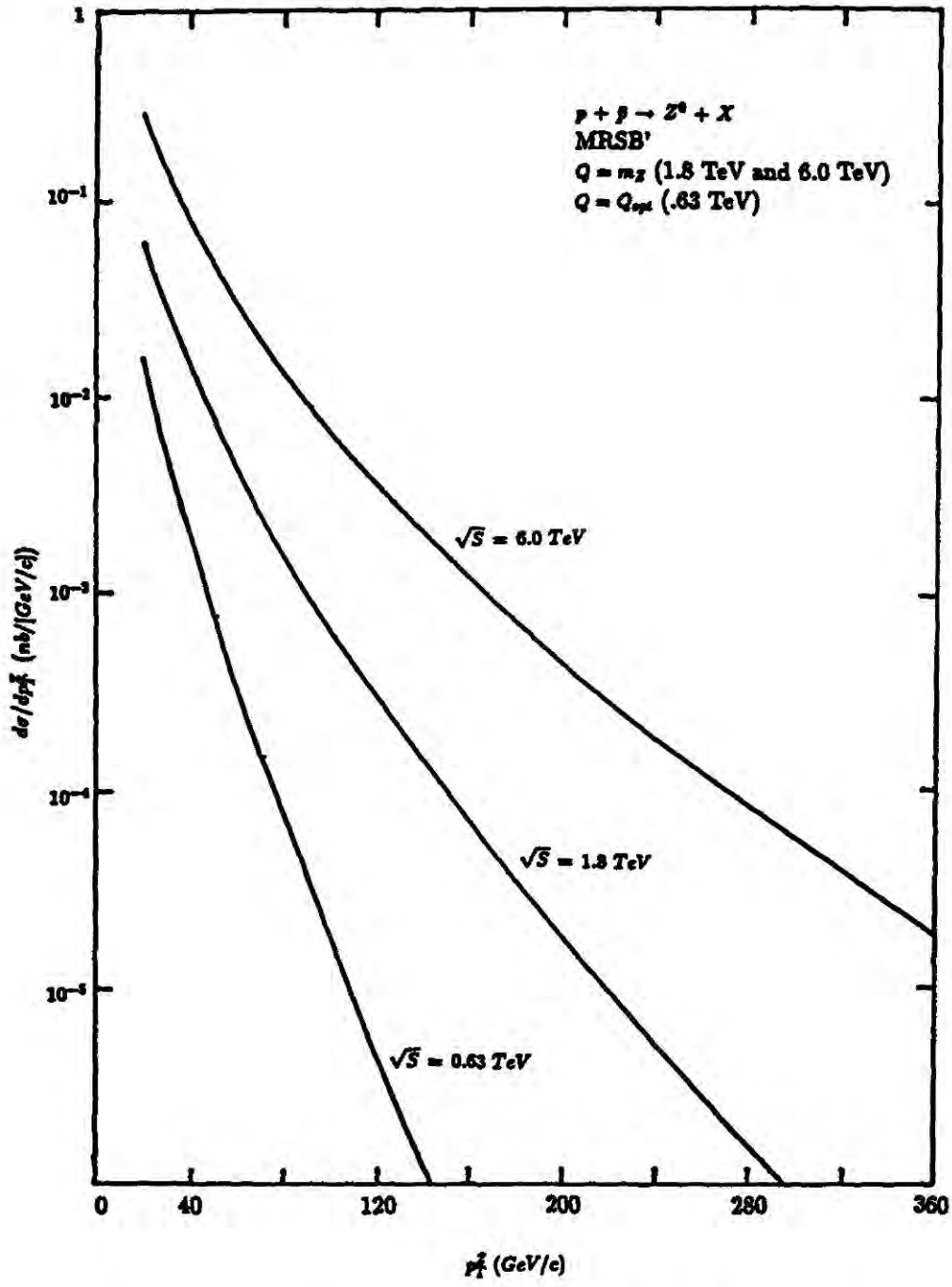

Figure 2.27 The fully-corrected $O(\alpha_s^2)$ prediction for the transverse momentum spectrum of Z bosons produced in $p\bar{p} \rightarrow Z + X$ at $\sqrt{S} = .63$, 1.8 and 6.0 TeV.

2.9 Conclusions.

It has been shown that the QCD prediction for the W transverse momentum spectrum is in good agreement with the data from the UA1 and UA2 collaborations at the CERN $Sp\bar{p}S$ collider. This agreement was first achieved with the non-singlet $O(\alpha_s^2)$ matix elements of Ellis *et al.* [10] and this required an assumption about the contribution of the singlet sector at next-to-leading order. It has been shown that this approximation was valid. With the inclusion of the singlet sector [11], this uncertainty has been removed from the calculation so that the

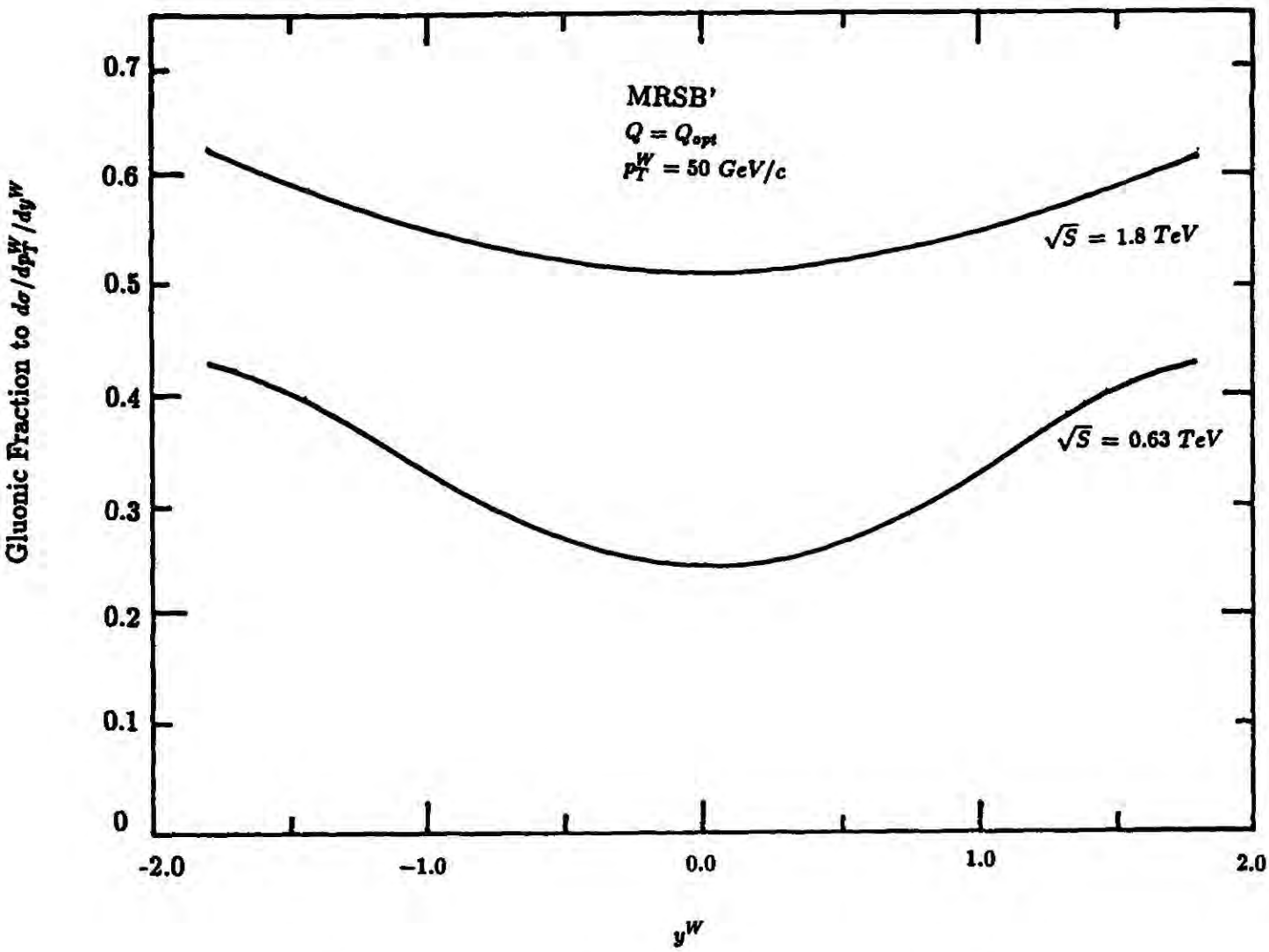

Figure 2.28 The gluonic fraction of the differential cross-section of the fully inclusive production of large transverse momentum W's in $p\bar{p}$ collisions, for $\sqrt{S} = .63$ and 1.8 TeV.

uncertainty in the calculation is restricted to: (i) the structure functions and (ii) the choice of scale.

To present some indication of the theoretical uncertainty, the cross-section is calculated using three different structure functions and two scales (see table 2). The actual quantity presented here is

$$F_{i-j} = \frac{\int_i^j \left[d\sigma/dp_T^W\right] \times dp_T^W}{\sigma_{tot},} \tag{2.127}$$

which is suitable for this purpose because it is the quantity that the experimentalists use to convert their events into cross-sections. So for instance, if the total number of events obtained during a run is N, then the number of events that theory predicts for the bin $[i-j]$ would be

$$N' = F_{i-j} \times N. \tag{2.128}$$

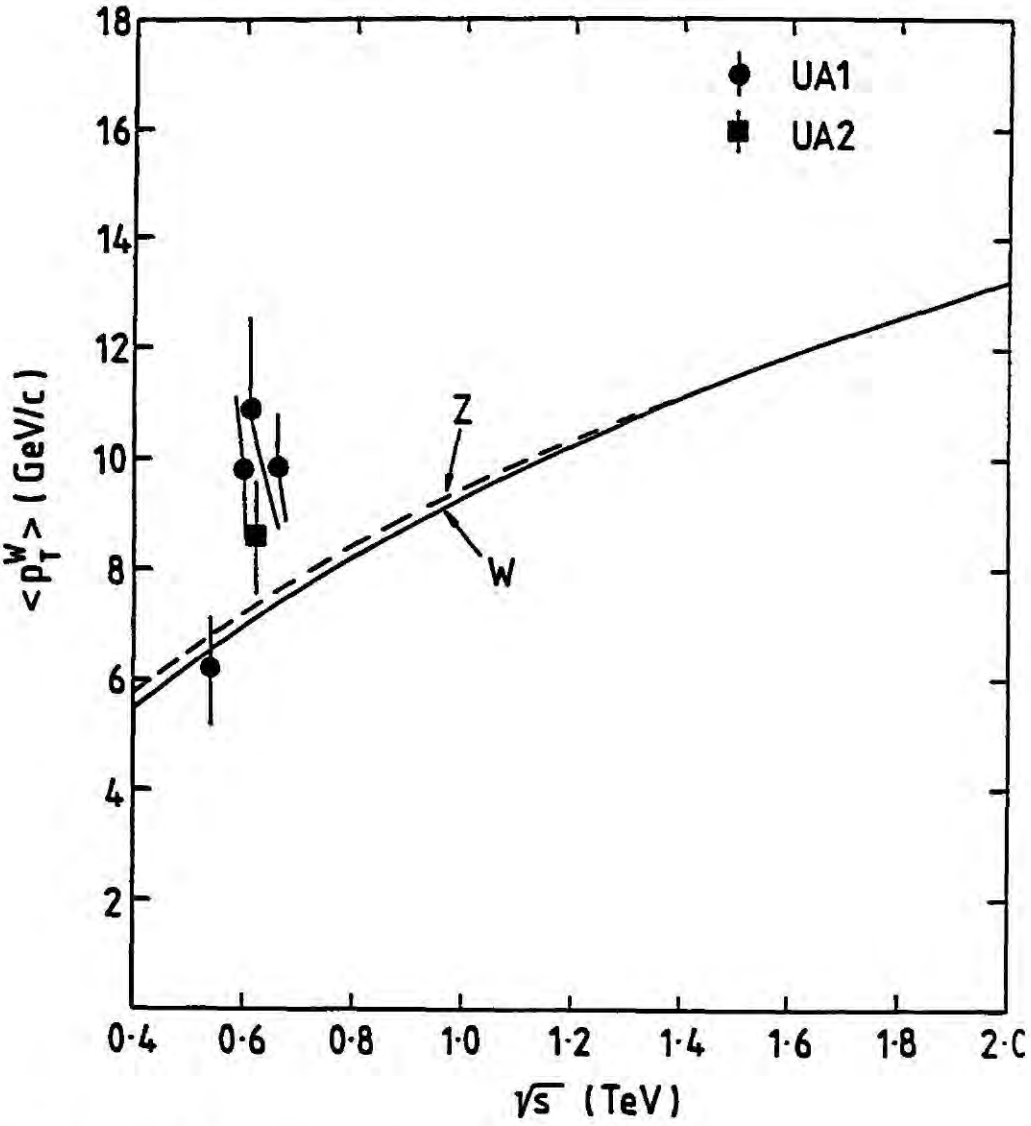

Figure 2.29 The average transverse momentum of W bosons produced in $p\bar{p}$ collisions as a function of $\sqrt{S}$. This calculation was performed at an optimum scale of $0.3m_W$ and with the MRSB$'$ set of structure functions.

Table 2

Str.Func.	Scale Q	λ_{QCD}	$F_{20-40}/\sum F$	$F_{40-60}/\sum F$	$F_{60-100}/\sum F$
MRSB'	Q_{opt}	.200	0.856	0.118	0.026
MRSB'	m_W	.200	0.845	0.126	0.029
MRSE'	Q_{opt}	.100	0.846	0.125	0.028
MRSE'	m_W	.100	0.839	0.130	0.031
MRS2	Q_{opt}	.250	0.860	0.116	0.025
MRS2	m_W	.250	0.847	0.124	0.028

The ratios F allow for the cancellation of some of the uncertainty.

Examining table 2, it is possible to estimate that the theoretical uncertainty

in the calculation is of the order of 20%.

It is clear that this process is not yet a precision test for perturbative QCD. However, the recently upgraded CERN collider (with the addition of ACOL) together with the recent upgrade of the UA experiments promise to improve considerably the statistics of the data. In addition, the CDF experiment is a copious producer of W and Z bosons and there is considerable hope that in the near future the process could be extremely important in pinning down Λ_{QCD} and the structure functions. Already there is fairly good agreement with the standard QCD predictions such as

$$\Lambda_{QCD} \sim 200 \pm 100\,\mathrm{MeV}. \tag{2.129}$$

The search for the top quark and the charged Higgs will be facilitated by the understanding of this process which is a background process for these searches. The, as yet unavailable, data from the Tevatron and from the proposed UNK accelerator will be challenged by well-defined and constrained theoretical predictions. Any statistically significant deviation in the data must signal 'new physics'.

REFERENCES

1. S.D. Drell and T.M.Yan: Phys. Rev. Lett.**25**, 316 (1970).
2. G. Altarelli, R.K. Ellis and G. Martinelli: Nucl. Phys. **B143**, 521 (1978) (E: **B146**, 544 (1978); **B157**, 461 (1979).
3. G. Altarelli: Phys. Rep.**81**, 1 (1982).
4. K. Kajantie and R. Raitio: Nucl. Phys. **B139**, 72 (1978).
5. R.K. Ellis, H. Georgi, M. Machacek, H.D. Politzer and G.G. Ross: Nucl. Phys. **B152**, 214 (1979).
6. J. Ellis and C.T. Sachrajda: Proc. 1979 Cargese Summer Institute on Quarks and Leptons (CERN-TH 2782/1979).
7. D. Amati, R. Petronzio and G. Veneziano: Nucl. Phys. **146** 29 (1978).
8. C. Aljabar *et al.*, UA1 Collab.: Phys. Lett. **B193**, 389, (1987).
9. R. Ansari *et al.*. UA2 Collab.: Phys. Lett. **B194**, 158 (1987).
10. R.K. Ellis, G. Martinelli and R. Petronzio: Nucl. Phys. **B211**, 106 (1983).
11. P. Arnold and H. Reno: FERMILAB-PUB-88/168-T, (E:FERMILAB-PUB-89/59-T).
12. A.D. Martin, R.G. Roberts and W.J. Stirling: Phys. Rev. **D37**, 1161 (1988).
13. H.D. Politzer: Phys. Rep. **14C**, 129 (1974);
14. R.K. Ellis, *et al.*: Nucl. Phys. **B152**, 285 (1979).
15. F. Halzen and A.D. Martin: Quarks and Leptons published Wiley (1984).
16. H.D. Politzer: Nucl. Phys. **B129**, 185 (1977).
17. A. Zee, F. Wilczek and S.B. Treiman: Phys. Rev. **D10**, 2881 (1974).
18. G. 't Hooft and M. Veltman: Nucl. Phys. **B44**, 189 (1972).
19. W.A. Bardeen, *et al.*: Phys. Rev. **D18**, 3998 (1978).

20. M. Diemoz *et al.*: Z. Phys. **C39**, 21 (1988).

21. M. Chanowitz, M. Furman and I. Hichcliffe: Nucl. Phys. **B159**, 225 (1979).

22. G. Lepage: J. Comput. Phys. **27**, 192 (1978).

23. S.D. Ellis and W.J. Stirling: Phys. Rev. **D23**, 214 (1981).

24. K. Hagiwara and D. Zeppenfeld: Nucl. Phys. **B274**, 1 (1986).

25. D.W. Duke and J.F. Owens: Phys. Rev. **D30**, 49 (1984).

26. A.D. Martin, R.G. Roberts and W.J. Stirling: DTP/89/18.

27. P.M. Stevenson: Nucl. Phys. **B277**, 758 (1986).

28. P. Aurenche *et al.*: Nucl. Phys. **B297**, 661 (1988).

29. P. Aurenche *et al.*: Nucl. Phys. **B286**, 509 (1987).

30. P. Aurenche *et al.*: Nucl. Phys. **B286**, 553 (1987).

31. S.B. Libby and G. Sterman: Phys. Rev. **D18**, 3257 (1978).

32. R. Kleiss, W.J. Stirling and S.D. Ellis: Phys. Lett. **154B**, 435 (1985).

33. C. Davies and W.J. Stirling: Nucl. Phys. **B244**, 337 (1984).

34. C. Davies, W.J. Stirling and B. Webber: Nucl. Phys. **B256**, 413 (1985).

35. G. Blaylock: personal communication.

---

3. A Study of the Equivalent Photon Approximation at HERA

3.1 Introduction

The HERA electron-proton collider is ideally suited to the study of hard scattering processes in almost-real photon-proton collisions [1]. Such processes provide many important tests of perturbative QCD and measurements of hadronic structure. Current fixed-target photoproduction experiments have collision energies limited to several tens of GeV. In contrast, HERA can investigate photoproduction at energies of order *hundreds* of GeV. For instance, if the proton beam at HERA has an energy of 820 GeV, then if

$$E_\gamma = 10\,GeV,\ \sqrt{S} = 180\,GeV$$

and if

$$E_\gamma = 20\,GeV,\ \sqrt{S} = 250\,GeV.$$

As a result, processes such as the production of large transverse momentum jets [2,3], hadrons [4] and single photons [5], Drell-Yan lepton pairs [6] and heavy quark pairs [7,8,9] can be studied.

Especially interesting are those processes which have been calculated to next-to-leading order in QCD perturbation theory. These offer the prospect of *precision* tests of the theory. Examples are the production of large transverse momentum photons ($\gamma q \rightarrow \gamma q$) [10] and the production of heavy flavours ($\gamma g \rightarrow Q\overline{Q}$) [11]. The first of these processes is important because in principle it provides a measurement of the quark distributions in the proton. According to the detailed phenomenological analysis of reference [5], the cross section should be measureable out to about $p_T^\gamma \simeq 50\ GeV/c$ which corresponds to x values for the quarks of $O(0.1)$ (assuming the standard HERA parameters with $\sqrt{s} \equiv \sqrt{s_{ep}} = 314\,GeV$). If the inclusive cross sections can be measured to an accuracy of better than order 10%, then some discrimination between various standard sets of quark distributions can be achieved [5]. In addition, the small p_T^γ cross section receives

contributions from the hadronic (i.e. quark and gluon) content of the photon, and it may be possible to extract information on these quantities by first 'subtracting off' the Born contribution [5].

There is, however, an important caveat to all of this. The 'precision' studies so far have all used the Equivalent Photon Approximation (EPA). This approximation, developed by von Weizsäcker [12] and Williams [13] in 1934, helps to reduce the complexity of a certain class of cross-section calculations in small-angle electron scattering. For example, it may be used to relate the high energy photon-induced cross section $d\sigma_{\gamma A \to B}$ to the corresponding electron-induced cross section $d\sigma_{eA \to B}$ by

$$d\sigma_{eA \to B} = \int dx\ G_{\gamma/e}(x)\ d\sigma_{\gamma A \to B}, \tag{3.1}$$

where $G_{\gamma/e}(x)$ is the structure function analogue for the distribution of photons in an electron. Clearly if one is interested in studying higher order QCD corrections, the quark and gluon content of the proton and photon and so on, it is important to establish that the errors introduced by this approximation are small and under control. This is the subject of the present study.

In the earlier work on the EPA [12,13], the approximation was defined in a semi-classical fashion in terms of the relevant impact parameters and the frequency of the photons. The cross-section expression above in this early formulation would have been written as

$$d\sigma_{eA \to B} = \int \frac{d\omega}{\omega} N(\omega) d\sigma_{\gamma A \to B}, \tag{3.2}$$

where $N(\omega)/\omega$ represents the number of equivalent photons with frequency ω in the field of a fast moving charged particle. The expression obtained for $N(\omega)$ by von Weizsäcker and Williams was

$$N(\omega) = \frac{2\alpha}{\pi} \ln\left(\frac{b_M}{b_m}\right) \tag{3.3}$$

where b_M is the largest impact parameter in the problem and b_m is the smallest. If the impact parameter is larger than $b_M = E/(\omega m)$ then the field of the relativistic particle (mass m) varies rapidly and the contribution to the cross-section

falls off rapidly. This determines the value of b_M. In this semi-classical theory, the Compton wavelength of the relativistic particle is used as the small impact parameter. Substituting these expressions for the impact parameters into (3.3), it is easily shown that the virtual photon-spectrum exhibits a logarithmic dependence on the frequency ω of the Coulomb field. The function $N(\omega)$ above is given by

$$N(\omega) = \frac{2\alpha}{\pi} \ln\left(\frac{E}{\omega}\right). \tag{3.4}$$

Many interesting real photoproduction processes may be studied at HERA such as the photoproduction of large p_T jets. However, for most of them it is not feasible to perform exact calculations, either because the diagrams are too complicated or the calculation time is excessive. The Compton scattering process is used as a simple test case since exact and approximate calculations are feasible to check the EPA. In addition, it may be noted that this happens to be an interesting process in its own right (see chapter 4). Here, a short study of the efficiency of the approximate calculation is made for the specific case of performing calculations with HERA parameters. This is done by doing a complete calculation for the process

$$e + q \rightarrow e + q + \gamma \tag{3.5}$$

and this is compared with the Compton scattering cross-section

$$\gamma + q \rightarrow \gamma + q, \tag{3.6}$$

where the initial state photons are the quasi-real photons that result from bremstrahlung off the 30 GeV electron beam and which are described by the EPA.

In the second section, the usual EPA is derived in the infinite-momentum frame, based on the derivation of Chen and Zerwas [14]. In section three, a description of the matrix element calculation for the process in (3.5) is presented. This calculation was performed with the spinor techniques of Kleiss and Stirling [16,17]. In section four, the phase space calculation is described. The results of the calculation are presented in section five, and finally the conclusions are presented in section six.

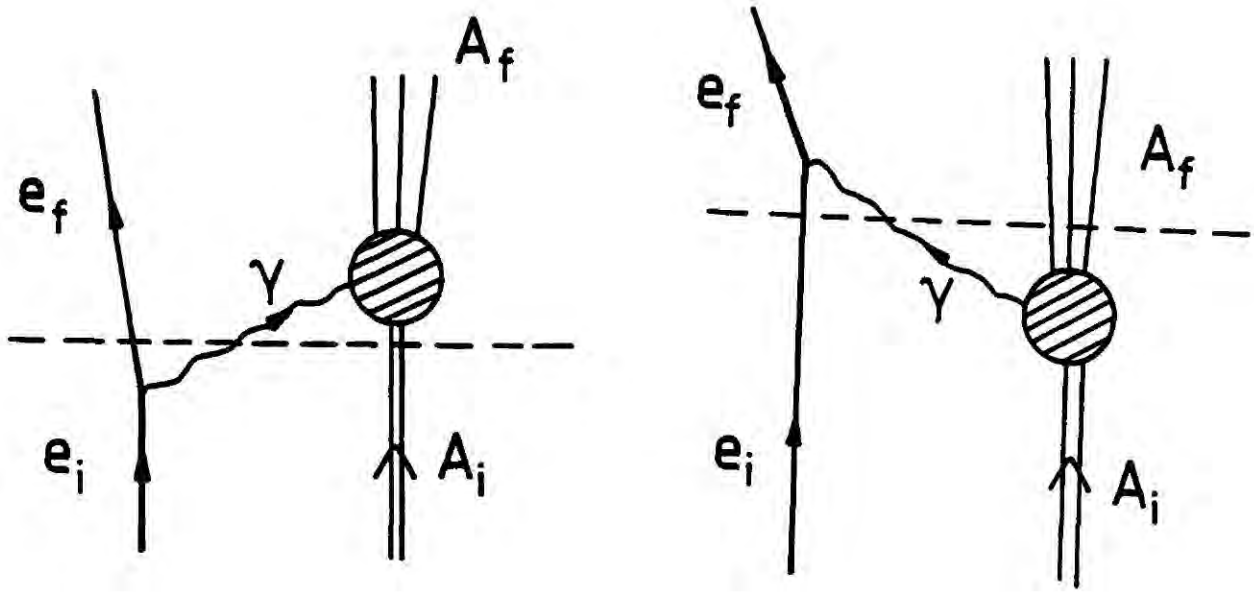

Figure 3.1 Diagrams for the inelastic scattering of an electron on a proton target in time-ordered perturbation theory.

3.2 Derivation of the Electron 'Structure Function'.

Detailed derivations of the EPA can be found in the literature (see for example references [14,17,18]) and so in this section the EPA is derived schematically using the technique of time-ordered perturbation theory in the infinite momentum frame. In the single photon approximation the diagrams in figure 3.1 represent inelastic electron scattering on a target A,

$$e_i + A_i \rightarrow e_f + A_f. \tag{3.7}$$

There are two possible intermediate states $|n\rangle$ in this process which correspond to the cut lines in figure 3.1 and the transition amplitude for this process is given by

$$T_{fi} = \sum_n \frac{< f|H|n >< n|H|i >}{E_i - E_n}, \tag{3.8}$$

where H is the Hamiltonian of the interaction and E_i and E_n are the initial state and intermediate state energies respectively.

The internal photon line leads to a factor of $(2\pi)^{-3}E^{-1}(\gamma)$ in the expression for the transition amplitude. Additionally, for each intermediate step there is a factor $(E_i - E_n)$, where E_n is the total energy in the initial channel and E_n is the intermediate-state energy. The $e_i\gamma e_f-$vertex is written as $\bar{u}(p_f)e\gamma^\mu u(p_i)\epsilon_\mu$. The intermediate-state ket is given by $|n\rangle = |e_f, \gamma_\lambda, A\rangle$, and substituting these into (3.8) produces the following expression for the transition amplitude:

$$T(e_iA_i \to e_fA_f) = e\sum_{\lambda=\pm1} \frac{\bar{u}(e_f)\not{\epsilon}(\lambda)u(e_i)\langle A_f|H|\gamma(\lambda), A_i\rangle}{2E(\gamma)[E(e_i) - E(e_f) - E(\gamma)]}\Bigg|_{\mathbf{p}(\gamma)=\mathbf{p}(e_i)-\mathbf{p}(e_f)} + \ldots \tag{3.9}$$

up to constant factors. This sum runs over the helicity states of the photon. Contributions from the longitudinal and scalar polarisations of the photon have been left out.

Assume that the incoming electron's three-momentum is $\mathbf{P}$ along the x-axis say, and that the three-momenta of the outgoing electron and photon are $\mathbf{P}'$ and $\mathbf{q}$ respectively. In the infinite momentum frame the momenta may be parametrised as

$$\begin{aligned} p(e_i) &= (\mathbf{P}; E(e_i)) = (P, \mathbf{0}; P + \frac{m_e^2}{2P}), \\ p(e_f) &= (\mathbf{P}'; E(e_f)) = ((1-x)P, -\mathbf{q_T}; (1-x)P + \frac{m_e^2 + q_T^2}{2(1-x)P}). \\ p(\gamma) &= (\mathbf{q}; E(\gamma)) = (xP, \mathbf{q_T}; xP + \frac{q_T^2}{2xP}). \end{aligned} \tag{3.10}$$

In these expressions, x is the momentum fraction of the initial-state electron carried off by the photon and $q_T = |\mathbf{q_T}|$ is the transverse momentum of the photon. In time-ordered perturbation theory, the vertices conserve momentum but not energy.

With the momenta in (3.10), the denominator in (3.9) reduces to

$$\frac{-(q_T^2 + m_e^2x^2)}{(1-x)}, \tag{3.11}$$

which indicates that cross-section is dominated by the small-q_T region where the scale of the matrix element is given by the inverse mass of the electron. This

fact allows the second diagram in figure 3.1 to be ignored since the scale of the amplitude in this case is given by the inverse mass of the proton. The square of the numerator in (3.9) has a term of the form

$$\sum_s [\bar{u}(e_f)\not{\epsilon}(\lambda')u(e_i)]^*[\bar{u}(e_f)\not{\epsilon}(\lambda')u(e_i)], \tag{3.12}$$

where the sum runs over the spins of the electron. Using the spin sums

$$\begin{aligned} \sum_s u(p,s)\bar{u}(p,s) &= (\not{p}+m), \\ \sum_s v(p,s)\bar{v}(p,s) &= (\not{p}-m) \end{aligned} \tag{3.13}$$

and averaging over the direction transverse momentum of the final state electron (3.12) reduces to

$$\delta_{\lambda\lambda'}\frac{2q_T^2}{x^2(1-x)}[1+(1-x^2)]+.... \tag{3.14}$$

The longitudinal and scalar polarisations of the photon do not contribute to leading order in q_T^2 and so the transition amplitude squared may be written as

$$\sum_s |T(e_iA_i \to e_fA_f)|^2 = e^2\frac{2(1-x)}{x^2(q_T^2+m_e^2x^2)}[1+(1-x)^2]\sum_\lambda |T(\gamma_\lambda A_i \to A_f)|^2. \tag{3.15}$$

In deriving (3.15), terms containing higher powers of the denominator (3.11) - which do not give logarithmic behaviour when the transverse momentum is integrated (see below) - have been omitted. They may be taken into account to obtain corrections to the leading order electron structure functions [14,17,18]. Finally, the cross-section for this process may be obtained by multiplying (3.15) by the flux factor and then integrating over the momenta of the final-state electron:

$$\sigma(e_iA_i \to e_fA_f) = \frac{\alpha}{\pi}\int_0^1 dx\frac{1+(1-x)^2}{x}\ln\frac{q_T^{max}}{m_ex}\sigma(\gamma A_i \to A_f). \tag{3.16}$$

Comparing (3.16) with (3.1) gives the electron 'structure function':

$$F_e^\gamma = \frac{\alpha}{\pi}\ln\eta\frac{1+(1-x)^2}{x}, \tag{3.17}$$

where $\eta = q_T^{max}/m_ex \gg 1$. In practice the value of q_T^{max} will be determined by the other kinematic variables in the process. It is not in fact a well-defined quan-

tity since when the final-state electron's transverse momentum becomes large, the small-angle approximation breaks down and the electron's phase space integration no longer factorises from the rest of the final state. All one can say, then, is that q_T^{max} is some quantity of the order of the maximum transverse momentum allowed by the overall kinematics. Within this definition, there are various possibilities for the variable η:

$$\eta = \frac{\sqrt{s}}{2m_e}, \frac{E_e}{m_e}, \frac{\sqrt{s_{\gamma p}}}{2m_e}, \frac{\sqrt{s_{\gamma q}}}{2m_e}, \ \ldots \tag{3.18}$$

In what follows different choices for η will be used to determine which gives the best approximation to the cross section.

The above analysis is relevant for the situation where the scattered electron is 'untagged', i.e. allowed to have any final-state momentum and therefore almost always lost in the beam-pipe at small angle. If, on the other hand, the electron is detected or 'tagged' in some small angular range then the above expressions for η are replaced by the ratio of the maximum and minimum tagging angles (see below). In what follows the EPA is studied for both tagged and untagged electrons.

The EPA provides a measure of the 'photon content' of the electron and to obtain a cross-section of an electron initiated process, such as $e_i + A_i \rightarrow e_f + A_f$, the corresponding photon cross-section may be convoluted with the EPA (see (3.1)).

As has been mentioned previously, to test the validity of the EPA in the HERA context a complete calculation of the process is

$$e + q \rightarrow e + \gamma + q \ ,$$

is performed where the final state photon has large momentum transverse to the electron-proton beam direction, and compare the resulting cross section with the real photon Compton scattering cross section for

$$\gamma + q \rightarrow \gamma + q$$

convoluted with the electron structure function derived above. The gauge-invariant set of Feynman diagrams for the process (14) are shown in figure 3.2. The

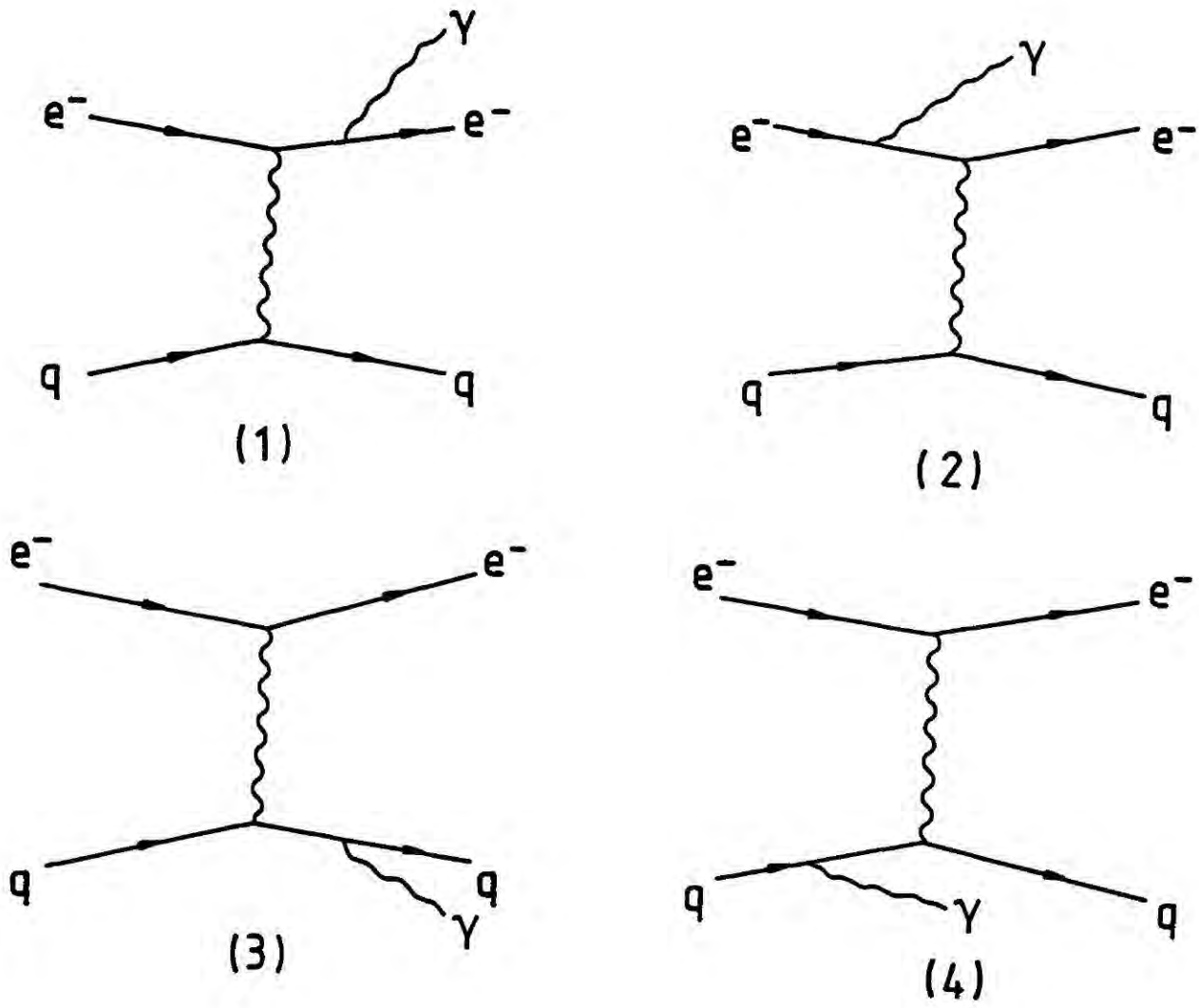

Figure 3.2 Feynman diagrams for the scattering process $e + q \rightarrow e + q + \gamma$.

four diagrams are calculated at the helicity amplitude level – using the 'spinor techniques' of reference [16] – and then evaluated numerically. Note that because the cross sections of interest involve small-angle electron scattering, it is necessary to keep the electron mass non-zero throughout the calculation, i.e in the matrix element *and* in the phase space integrals.

3.3 The Helicity Amplitude Calculation.

The gauge-invariant set of Feynman diagrams for the process in (3.5) comprises of four diagrams, shown in figure 3.2. The diagrams have been calculated at helicity amplitude level and then evaluated numerically. In what follows, this calculation is repeated to demonstrate the use of spinor techniques in the evaluation of Feynman graphs.

The calculation was done with massive electrons but massless quarks. The quark helicity at the $q\gamma q-$vertex is conserved and so the helicity of both the initial and final state quarks is set at $\lambda(q)$. However, for the massive electrons helicity is not conserved at the $e\gamma e-$vertex. The initial- and final-state electrons have helicities $\lambda(e_i)$ and $\lambda(e_f)$, respectively and the helicity of the photon is $\lambda(\gamma)$.

The initial- and final-state electrons in figure 3.2 have momenta p_1 and p_3 respectively, while the initial- and final-state quarks have momenta p_2 and p_4 respectively. The external photon has momentum k. To begin with, the Feynman diagram in figure 3.2(1) is expressed in terms of the spinors, polarisation vectors and $\gamma-$matrices, as usual.

$$\begin{aligned}\mathcal{M}(k,p_j,\lambda_\gamma,\lambda_j) = {} & \bar{u}(p_3,\lambda_3)(ie\gamma_\mu)\,\epsilon^{\mu*}(k,\lambda_\gamma) \\ & \frac{i(\not{p}_3+\not{k}+m)}{(p_3+k)^2-m^2}(ie\gamma_\nu)u(p_1,\lambda_1)\times\left[\frac{-ig^{\nu\lambda}}{(p_4-p_2)^2}\right] \\ & \bar{u}(p_4,\lambda_q)(ie_q\gamma_\lambda)\,u(p_2,\lambda_q),\end{aligned} \tag{3.19}$$

where m is the mass of the electron and the ϵ is the polarisation vector of the the external photon. The $\gamma-$matrices are the usual Dirac ones.

The spinors [15,16] are defined in terms of a fundamental negative-helicity spinor, $u_-(k_0)$ and the corresponding positive-helicity spinor is then defined as

$$u_+(k_0) = \not{k}_0' u_-(k_0), \tag{3.20}$$

where the four vectors k_0 and k_0' satisfy the following: $k_0.k_0 = 0$, $k_0'.k_0' = -1$ and $k_0.k_0' = 0$. These spinors represent the helicity states of a massless fermion of

momentum k_0; that is,

$$u_\lambda(k_0)\bar{u}_\lambda(k_0) = \frac{1}{2}(1+\lambda\gamma^5)\not{k}_0. \tag{3.21}$$

From these, it is possible to construct spinors for any other fermion as follows

$$u_\lambda(p) = (\not{p}+m)u_{-\lambda}(k_0)/\sqrt{2p.k_0}, \tag{3.22}$$

where $\lambda = \pm 1$. The spinors are normalised in the usual way, $\bar{u}_\lambda(p)u_\lambda(p) = 2m$, where m is the mass of the particle. To take (3.19) a step further, the polarisation vector, ϵ, is defined in terms of states of definite helicity denoted by

$$\epsilon^\mu_\lambda(k) = \frac{\bar{u}_\lambda(k)\gamma^\mu u_\lambda(p_0)}{\sqrt{4k.p_0}}, \tag{3.23}$$

where p_0 is any light-like vector which is not collinear to k. This vector p_0 defines the gauge in which the calculation is performed.

Using the Chisholm identity

$$[\bar{u}_\lambda(p_1)\gamma^\mu u_\lambda(p_2)]\gamma_\mu = 2\times[u_\lambda(p_2)\bar{u}_\lambda(p_1) + u_{-\lambda}(p_1)\bar{u}_{-\lambda}(p_2)], \tag{3.24}$$

$\not{\epsilon}$ may be expressed in terms of spinors as

$$\not{\epsilon}_\lambda(k) = \frac{[u_\lambda(p_0)\bar{u}_\lambda(k) + u_{-\lambda}(k)\bar{u}_{-\lambda}(p_0)]}{\sqrt{4p_0.k}}. \tag{3.25}$$

The internal fermion lines are treated as a sum of the two helicity projections divided by the usual propagator squared. So for instance, an internal fermion line, $\not{p}$, is replaced by

$$\not{p} = u_+(p)\bar{u}_+(p) + u_-(p)\bar{u}_-(p). \tag{3.26}$$

The expression for the helicity amplitude (3.19) can now be expressed in

terms of spinors and γ matrices, using (3.23) and (3.26), as

$$\begin{aligned}\mathcal{M}(k,p_j,\lambda_\gamma,\lambda_j) &= C \times \bar{u}(p_3,\lambda_3)(ie\gamma_\mu)[\bar{u}(p_0,\lambda_\gamma)\gamma^\mu u(k,\lambda_\gamma)] \\ &[u(p_3,+)\bar{u}(p_3,+) + u(p_3,-)\bar{u}(p_3,-) + u(k,+)\bar{u}(k,+) + u(k,-)\bar{u}(k,-)]\,, \\ &\gamma_\nu u(p_1,\lambda_1)\bar{u}(p_4,\lambda_q)(\gamma^\nu)u(p_2,\lambda_q)\end{aligned} \tag{3.27}$$

where the couplings and propagators are collected together in C

$$C = \frac{-ie^2 e_q}{[(p_3+k)^2 - m^2](p_4-p_2)^2\sqrt{4(p_0.k)}}, \tag{3.28}$$

and the ν and λ indices have been contracted.

By applying the Chisholm identity (3.24), the helicity amplitude may then be expressed completely in terms of products of spinors as

$$\begin{aligned}\mathcal{M}(k,p_j,\lambda_\gamma,\lambda_j) &= 4C \times \bar{u}(p_3,\lambda_3)\,[u(k,-\lambda_\gamma)\bar{u}(p_0,-\lambda_\gamma) + u(p_0,\lambda_\gamma)\bar{u}(k,\lambda_\gamma)] \\ &[u(p_3,+)\bar{u}(p_3.+) + u(p_3,-)\bar{u}(p_3,-) + u(k,+)\bar{u}(k,+) + u(k,-)\bar{u}(k,-)] \\ &[u(p_2,\lambda_q)\bar{u}(p_4.\lambda_q) + u(p_4,-\lambda_q)\bar{u}(p_2,-\lambda_q)]u(p_1,\lambda_1).\end{aligned} \tag{3.29}$$

Finally, it is necessary to define spinor products which define the spinor algebra for the calculation. In the case in which there are massive particles, three spinor products are required. These are:

$$\begin{aligned}S_{+-}(p_1,p_2) &= \bar{u}_+(p_1)u_-(p_2) \\ &= (p_1^y + ip_1^z)\eta_2/\eta_1 - (p_2^y + ip_2^z)\eta_1/\eta_2, \\ S_{-+}(p_1,p_2) &= [S_{+-}(p_2,p_1)]^*, \\ S_{\pm\pm}(p_1,p_2) &= m_1\eta_2/\eta_1 + m_2\eta_1/\eta_2, \\ \eta_i &= [2p_i^0 - 2p_i^x]^{1/2}.\end{aligned} \tag{3.30}$$

The connection with the massless case is a smooth one, meaning that as $m \to 0$ in (3.30), the spinor products reduce to those for the massless case:

$$\begin{aligned}S(p_1,p_2) &\equiv \bar{u}_+(p_1)u_-(p_2) = -S(p_2,p_1)^*, \\ T(p_1,p_2) &\equiv \bar{u}_-(p_1)u_+(p_2) = [S(p_2,p_1)]^*.\end{aligned} \tag{3.31}$$

These lead to the following relation between the spinor products and the dot

product between momenta:

$$|s(p_1,p_2)|^2 = 2p_1.p_2, \tag{3.32}$$

in the massless case. Notice that in the massless case it is only the first two spinor products in (3.30) that survive.

The helicity amplitude can now be presented in terms of these spinor products which will allow the diagram to be calculated, in terms of the momenta and helicities of the particles, using (3.30).

$$\begin{aligned}
&\mathcal{M}(k,p_j,\lambda_\gamma,\lambda_j) = 4C \times [S(p_3,k,\lambda_3,-\lambda_\gamma)\\
&\times [S(p_0,p_3,-\lambda_\gamma,+)S(p_3,p_2,+,\lambda_q) + S(p_0,p_3,-\lambda_\gamma,-)S(p_3,p_2,-,\lambda_q)+\\
&S(p_0,k,-\lambda_\gamma,+)S(k,p_2,+,\lambda_q) + S(p_0,k,-\lambda_\gamma,-)S(k,p_2,-,\lambda_q)]\\
&\times S(p_4,p_1,\lambda_q,\lambda_1)+\\
&S(p_3,k,\lambda_3,-\lambda_\gamma)\\
&\times [S(p_0,p_3,-\lambda_\gamma,+)S(p_3,p_4,+,-\lambda_q) + S(p_0,p_3,-\lambda_\gamma,-)S(p_3,p_4,-,-\lambda_q)+\\
&S(p_0,k,-\lambda_\gamma,+)S(k,p_4,+,-\lambda_q) + S(p_0,k,-\lambda_\gamma,-)S(k,p_4,-,-\lambda_q)]\\
&\times S(p_3,p_1,-\lambda_q,\lambda_1)+\\
&S(p_3,p_0,\lambda_3,\lambda_\gamma)\\
&\times [S(k,p_3,\lambda_\gamma,+)S(p_3,p_2,+,\lambda_q) + S(k,p_3,\lambda_\gamma,-)S(p_3,p_2,-,\lambda_q)]\\
&\times S(p_4,p_1,\lambda_q,\lambda_1)+\\
&S(p_3,p_0,\lambda_3,\lambda_\gamma)\\
&\times [S(k,p_3,\lambda_\gamma,+)S(p_3,p_4,+,-\lambda_q) + S(k,p_3,\lambda_\gamma,-)S(p_3,p_4,-,-\lambda_q)]\\
&\times S(p_2,p_1,-\lambda_q,\lambda_1)].
\end{aligned} \tag{3.33}$$

This expression for the helicity amplitude is a function of the momenta of the external four-momenta, the one gauge-determining four-momentum and the helicities of the initial- and final-state electrons, the photon and the quark. A helicity amplitude is calculated for each of the possible helicity combinations. Noting that the particle helicities can be ± 1, and that the helicity is not conserved at the $e\gamma e-$vertex but is conserved at the $q\gamma q-$vertex, the possible amplitudes for

this diagram are:

$$\begin{aligned}
\mathcal{M}(k,p_j,\lambda_\gamma,\lambda_1,\lambda_2,\lambda_3,\lambda_4) : &\mathcal{M}(k,p_j,+,+,+,+,+)\\
&:\mathcal{M}(k,p_j,+,+,+,-,-)\\
&:\mathcal{M}(k,p_j,+,-,+,+,+)\\
&:\mathcal{M}(k,p_j,+,-,+,-,-)\\
&:\mathcal{M}(k,p_j,+,+,-,+,+)\\
&:\mathcal{M}(k,p_j,+,+,-,-,-)\\
&:\mathcal{M}(k,p_j,+,-,-,+,+)\\
&:\mathcal{M}(k,p_j,+,-,-,-,-).
\end{aligned} \tag{3.34}$$

This list of helicity amplitudes is completed by repeating the cycle for the negative photon helicity case. Numerically, this doubles the contribution from (3.34). This process is repeated for each of the four diagrams.

The next step in the calculation is to coherently add up each helicity amplitude for the full set of diagrams. For instance,

$$\mathcal{M}^{eq\to eq\gamma}(k,p_j,+,+,+,+,+) = \sum_i \mathcal{M}_i(k,p_j,+,+,+,+,+), \tag{3.35}$$

where i runs through the full set of diagrams. These helicity amplitudes are imaginary numbers at this stage of the calculation. They are then squared and summed over all possible helicity combinations, providing finally the matrix element squared for the process in (3.5). This quantity must be gauge-invariant and as the four momentum p_0 is restricted only by the requirement that it is not collinear with k, changing p_0 should leave the matrix element squared unchanged. This provides a good self-consistency check.

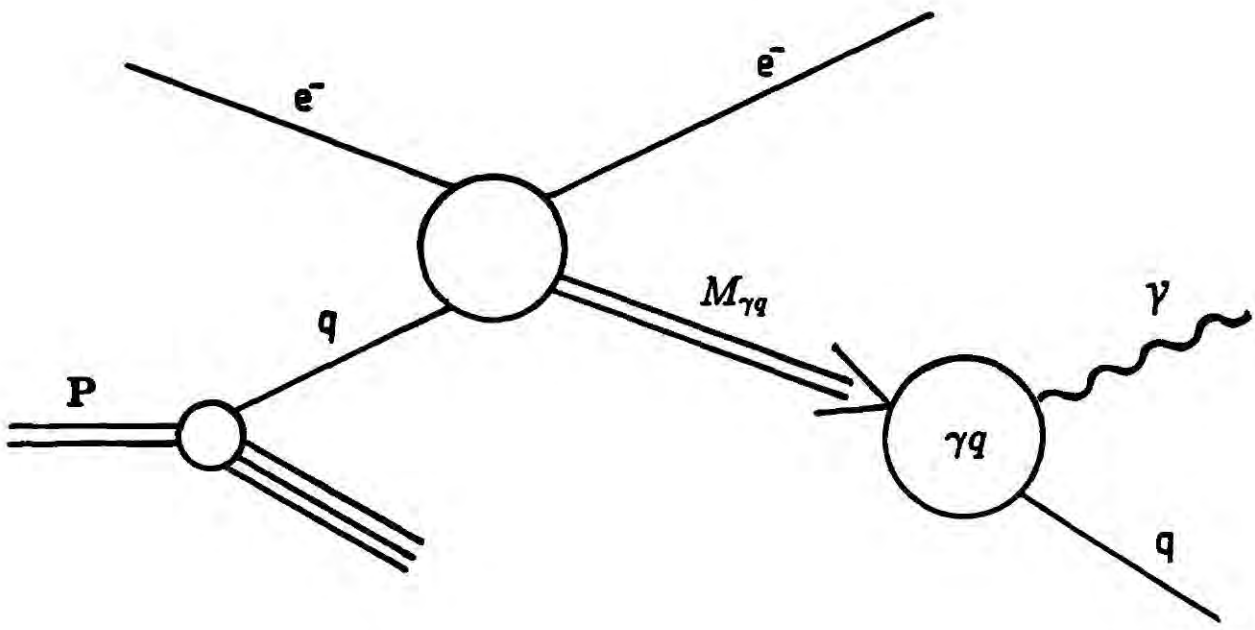

Figure 3.3 A schematic representation of the 2 → 3−body phase space calculation.

3.4 The Phase Space Integrals.

For three particles in the final state, the invariant phase space is given by

$$(PS)^3 = \int \frac{d^3p_3}{(2\pi)^3 2p_3^0}\frac{d^3p_4}{(2\pi)^3 2p_4^0}\frac{d^3k}{(2\pi)^3 2k^0}(2\pi^4)\delta^{(4)}(p_1+p_2-p_3-p_4-k). \quad (3.36)$$

The three-body phase space is treated in two steps, each of two-body phase space. As is shown schematically in figure 3.3, the first step is to consider the production of an electron and a composite γq system to which a mass of $M_{\gamma q}$ is designated. The next step is to handle the decay of this composite state into a photon and a quark.

For the first step, (3.36) may be written as

$$\begin{aligned}(PS)^3 =&(2\pi)^{-5}\frac{1}{8}\int \frac{d^3p_3}{p_3^0}\delta^{(4)}(p_1+p_2-p_3-P_{\gamma q})\\ &\times \int_{S_0}^{S} dM_{\gamma q}^2 \int d^4P_{\gamma q}\delta(P_{\gamma q}^2-M_{\gamma q}^2) \qquad (3.37)\\ &\times \int \frac{d^3k}{k^0}\frac{d^3p_4}{p_4^0}\delta^{(4)}(P_{\gamma q}-k-p_4).\end{aligned}$$

The γq integrals may be simplified somewhat by making the observation that in

(3.37)

$$\begin{aligned}\int d^4P_{\gamma q} &= \int dE_{\gamma q} d^3P_{\gamma q}\delta(P_{\gamma q}^2 - M_{\gamma q}^2) \\ &= \int \frac{dE_{\gamma q}^2}{2E_{\gamma q}} d^3P_{\gamma q}\delta(E_{\gamma q}^2 + \mathbf{p}_{\gamma q}^2 - M_{\gamma q}^2) \\ &= \frac{d^3P_{\gamma q}}{2E_{\gamma q}},\end{aligned} \tag{3.38}$$

and $E_{\gamma q}^2 = \mathbf{p}_{\gamma q}^2 - M_{\gamma q}^2$. Using (3.38), the expression for the phase space reduces to a recognisable two body phase space with some additional integrals:

$$\begin{aligned}(PS)^3 &= (2\pi)^{-5}\frac{1}{16}\int \frac{d^3p_3}{p_3^0}\frac{d^3P_{\gamma q}}{E_{\gamma q}}\delta^{(4)}(p_1 + p_2 - p_3 - P_{\gamma q}) \\ &\quad \times \int_{S_0}^{S} dM_{\gamma q}^2 \int \frac{d^3k}{k^0}\frac{d^3p_4}{p_4^0}\delta^{(4)}(P_{\gamma q} - k - p_4) \\ &= (2\pi)^{-5}\frac{1}{16}\int \frac{d^3p_3}{p_3^0 \times E_{\gamma q}}\delta(p_1^0 + p_2^0 - p_3^0 - E_{\gamma q}) \\ &\quad \times \int_{S_0}^{S} dM_{\gamma q}^2 \int \frac{d^3k}{k^0}\frac{d^3p_4}{p_4^0}\delta^{(4)}(P_{\gamma q} - p_3 - p_4).\end{aligned} \tag{3.39}$$

At this stage it is possible to simplify matters by going into the ep centre-of-mass frame in which $p_1^0 + p_2^0 = \sqrt{S}$ and then

$$(PS)^3 = (2\pi)^{-5}\frac{1}{16}\int \frac{p_3 dp_3 d\Omega}{p_3^0 E_{\gamma q}}\delta(\sqrt{S} - p_3^0 - E_{\gamma q})...., \tag{3.40}$$

where $d\Omega$ is a volume element. In this frame $|\mathbf{p}_3| = |\mathbf{P}_{\gamma q}| = p_f$, say. Then

$$W = \sqrt{S} = (p_f^2 + m_e^2)^{1/2} + (p_f^2 + M_{\gamma q}^2)^{1/2} \tag{3.41}$$

and it is easily shown that

$$\frac{dW}{dp_3} = p_3\frac{W}{p_3^0 E_{\gamma q}}. \tag{3.42}$$

The volume element may be written as $d\Omega = sin\theta\, d\theta\, d\phi = dcos\theta\, d\phi$. Substituting this volume element expression and (3.42) into the phase space expression (3.40)

produces

$$(PS)^3 = (2\pi)^{-4}\frac{1}{16}\int\frac{|p_3|dcos\theta}{\sqrt{S}}\int dM_{\gamma q}^2 \times \int\frac{d^3k}{k^0 p_3^0}\delta(k^0 + p_3^0 - E_{\gamma q}). \tag{3.43}$$

The next step is to enter the γq centre-of-mass frame and to repeat this last two body calculation. For this step, $M_{\gamma q}$ and $P_{\gamma q}$ are available from the above and the phase space for this two-body decay is

$$\int\frac{d^3k}{k^0 p_3^0}\delta(k^0 + p_3^0 - E_{\gamma q}) = \int\frac{|\mathbf{k}|}{E_{\gamma q}}dcos\theta_\gamma d\phi_\gamma. \tag{3.44}$$

Putting (3.44) in (3.43) a final expression for the three-body phase space is obtained:

$$(PS)^3 = (2\pi)^{-4}\frac{1}{32}\int\frac{|p_3|dcos\theta}{\sqrt{S}}\int dM_{\gamma q}^2 \times \int dcos\theta_\gamma d\phi_\gamma. \tag{3.45}$$

The integrals in (3.45) are performed numerically with the VEGAS package. To perform the $M_{\gamma q}^2$ integral, it is necessary to define the upper and lower limits of $M_{\gamma q}^2$. The upper limit is defined by invariant external kinematics:

$$S_{ep} = 2P_e.P_p = 4 \times 30 \times 820 \;\; GeV^2, \tag{3.46}$$

where P_e and P_p are the laboratory frame momenta of the electron and the proton, respectively. S_0 is defined by a suitable cut-off value and the $M_{\gamma q}^2$ integral can be written as

$$\int_{S_0}^{S_{ep}}\frac{dM_{\gamma q}^2}{M_{\gamma q}^2} \times M_{\gamma q}^2 = \int_{S_0}^{S_{ep}} d\ln M_{\gamma q}^2 \times M_{\gamma q}^2. \tag{3.47}$$

In terms of the random VEGAS integration parameter r_1, $M_{\gamma q}^2$ is defined by

$$M_{\gamma q}^2 = S_0^{r_1} \times S_{ep}^{1-r_1}, \tag{3.48}$$

where $0 \leq r_1 \leq 1$. The Jacobian for this change of variable is just $J_M = \ln(S/S_0)$.

The cross-section calculation is obtained by convoluting (3.45) and the matrix element calculation of the last section with the distribution function of the quarks within the proton. If the momentum of the quark within the proton is $p_2 = x \times P_p$, then

$$S_{eq} = x \times S_{ep} > S_0 + (M_{\gamma q} + m_e)^2 \tag{3.49}$$

and the upper and lower limits of the $x-$integration are

$$\begin{aligned} x_{max} &= 1, \\ x_{min} &= \frac{S_0 + (M_{\gamma q} + m_e)^2}{S_{ep}}. \end{aligned} \tag{3.50}$$

In terms of the random VEGAS parameter r_2, $x = J_x \times r_2 + x_{min}$ where $J_x = x_{max} - x_{min}$.

In the eq centre-of-mass frame, the four-vectors may be defined as follows:

$$\begin{aligned} p_1 &= (p, 0, 0; [p^2 + m_e^2]^{\frac{1}{2}}), \\ p_2 &= (-p, 0, 0; p), \\ p_3 &= (qcos\theta, -qsin\theta sin\phi, -qsin\theta cos\phi; p_3^0), \\ P_{\gamma q} &= (-qcos\theta, qsin\theta sin\phi, qsin\theta cos\phi; E_{\gamma q}), \end{aligned} \tag{3.51}$$

where $p = \sqrt{\hat{s}}/2$, and q, p_3^0 and $E_{\gamma q}$ are defined as

$$\begin{aligned} E_{\gamma q} &= \sqrt{\hat{s}} - p_3^0, \\ q^2 &= (p_3^{02} - m_e^2) \\ &= (E_{\gamma q}^2 - M_{\gamma q}^2), \end{aligned}$$

which lead to

$$\begin{aligned} p_3^0 &= \frac{\hat{s} + m_e^2 - M_{\gamma q}^2}{2\sqrt{\hat{s}}}, \\ E_{\gamma q} &= \sqrt{\hat{s}} - p_3^0, \\ q^2 &= E_{\gamma q}^2 - M_{\gamma q}^2. \end{aligned} \tag{3.52}$$

The matrix elements have a pole in the t-channel. This pole can be isolated

and absorbed into the phase space expression. $\hat{t}$ is defined as

$$\begin{aligned}\hat{t} &= (p_1 - p_3)^2 = -2p_1.p_3 + 2m_e^2 \\ &= -2(p_1^0 p_3^0 - pqcos\theta) + 2m_e^2,\end{aligned} \tag{3.53}$$

where p, q are defined above. Dividing (3.45) by $\hat{t}$ gives

$$\begin{aligned}(PS)^3 &= \frac{1}{(2\pi)^4}\frac{1}{32}\frac{1}{\sqrt{S}}\int_{-\pi}^{\pi}\frac{q\ dcos\theta}{-2(p_3^0 p_1^0 - pqcos\theta)}\int_0^{2\pi}d\phi\int .... \\ &= \frac{1}{(2\pi)^3}\frac{1}{32}\frac{1}{\sqrt{S}}\int_{-1}^{1}\frac{qdy}{-2(a-by)}....,\end{aligned} \tag{3.54}$$

where $a = p_3^0 p_1^0$ and $b = pq$. If the substitution $z = a - by$ is made in (3.54) then this integral reduces to

$$(PS)^3 = -\frac{1}{(2\pi)^5}\frac{1}{32}\frac{1}{\sqrt{S}}\int_{a-b}^{a+b}\frac{q}{2b}d\ln z..... \tag{3.55}$$

In terms of the VEGAS parameter, r_3, this integral may be parametrised as follows:

$$\begin{aligned}z &= (a+b)^{r_3}(a-b)^{1-r_3} \\ \ln z &= r_3\ln(a+b) + (1-r_3)\ln(a-b).\end{aligned}$$

This substitution introduces a Jacobian $J_{cos} = \ln[(a-b)/(a+b)]$.

The final stage is to develop the four-momenta of the photon and quark in the final state and this is achieved by going to the γq centre-of-mass frame defining the photons angular variables in terms of the VEGAS random parameters as

$$\begin{aligned}\cos\theta_\gamma &= 2r_4 - 1 \\ \text{and}\quad \phi_\gamma &= 2\pi r_5.\end{aligned}$$

This prepares the phase space for computation.

The amplitude for the scattering process (3.5) contains additional singularities when the final-state photon is collinear with the outgoing electron and quark. However these are not in the 'physical' region, since the experimental set-up that is envisaged triggers on a large transverse momentum photon balanced by a large transverse momentum (quark) jet, with the electron emerging at small angle to the beam. The three final-state particles are therefore always well-separated in phase space. To make this more precise a minimum invariant mass cut (which has been defined as $M_{\gamma q}$ above) is imposed on the final-state γq system together with a minimum transverse momentum cut on the photon.

A check for the phase space was performed by using the kinematics of the problem and producing the four-vectors and event weights with the phase space generator, RAMBO [19]. By building in the identical cuts to this check, it was possible to obtain exact correspondence between the two phase space calculations.

3.5 Calculations and Comparisons.

For the final-state configuration that is of relevance only the third and fourth Feynman diagrams in figure 3.2 are numerically relevant. However some care must be taken with this statement as only the complete set of four diagrams is gauge invariant. In other words, the statement that some diagrams give bigger contributions than others is gauge dependent. The first two diagrams do not have an intermediate quasi-real photon propagator and are therefore outside the EPA interpretation.

Gauge invariance is only slightly broken by considering this subset of Feynman diagrams. This has been checked in the following manner. The structure function and phase space weight of the calculation were switched-off, though the phase space subroutine still produced the four vectors of the external particles, which therefore satisfied the mass-shell and conservation of momentum conditions. The ratio

$$\frac{\mathcal{M}(diagrams1+2)+\mathcal{M}(diagrams3+4)}{\mathcal{M}(diagrams3+4)}, \tag{3.56}$$

was considered where the diagram numbers refer to their numbering in figure 3.2.

Deviation from 1 in the quantity in (3.56) provides a measure of the breakdown of gauge invariance. The gauge-defining vector, p_0, is a general, massless four-vector and was parametrised in terms of (r, θ, ϕ). These parameters were then allowed to vary in incremental steps of the order of 10^{-2} through their full range and no deviation from one in the ratio (3.56) bigger than 0.1% was found. However, as expected, when $p_0 = k$, the photon four-momentum, the matrix element diverges because of the $(p_0.k)$ pole in (3.23). However, if this pole is approached in $\cos\theta$ increments of 1×10^{-6}, keeping $\cos\phi$ fixed on the $\cos\phi$ of the photon, no divergence is encountered and the ratio in (3.56) is unaltered. If this incremental step is further decreased to 1×10^{-7} then the divergence is encountered but the ratio is still consistent with gauge invariance around this divergence. Thus, for this set of gauges, diagrams 1 and 2 in figure 3.2 may in practice be ignored.

For the actual cross section calculations the MRS1 set of quark distributions is used [20], with $\Lambda_{QCD} = 107\ MeV$, and the factorisation scale is set equal to the transverse momentum of the photon. Four flavours of quarks are assumed. These parameters are held fixed throughout the analysis. The effect of different choices of parton distributions and of different scales has been studied for the EPA cross section in reference [5].

The first step was to obtain some indication of the relative accuracy of the three usual choices for η in the electron 'structure function' in (3.18) in the case in which the final state electron is untagged. The invariant mass of the final-state γq–system is given a lower cut, $M_{\gamma q} = \sqrt{s_{\gamma q}} \geq 20\,GeV$. The results of this calculation are presented in table 1. The uncertainties, error(1), error(2) and error(3) refer to the choices $\eta = \sqrt{\hat{s}}/2m_e$, $\eta = E_e/m_e$ and $\eta = \sqrt{S}/2m_e$ respectively. Note the $\hat{s}$ denotes the γq subprocess centre-of-mass scattering energy, i.e. $\hat{s} \equiv s_{\gamma q}$.

The results indicate that in the case of the untagged final-state electron, the $\sqrt{S}/2m_e$ choice for η produces the smallest error in the cross-section. This is not perhaps surprising since $\sqrt{S}/2$ represents the absolute maximum of the transverse momentum of the outgoing electron. It also has the advantage of being Lorentz invariant. From the results of reference [5] the total cross-section for $p_T^\gamma > 10\,GeV/c$ is an order of magnitude larger than that with $p_T^\gamma > 20\,GeV/c$,

Table 1

$p_T^{\gamma min}$	% error(1)	% error(2)	% error(3)
10	-19.5	-13.5	-0.5
20	-19.1	-19.1	-6.9
30	-18.5	-21.0	-9.1
40	-17.9	-22.0	-10.2
50	-17.2	-22.5	-10.9
60	-16.4	-22.8	-11.0
70	-15.2	-22.8	-11.0
80	-14.7	-22.8	-11.0

and this is where the EPA with $\eta = \sqrt{S}/2m_e$ has a very small error. The EPA does appear to get slightly worse at large values of p_T^γ, but the corresponding cross-sections are too small to be measured experimentally .

The approximate calculation consistently underestimates the exact cross section. This is presumably because with exact kinematics and matrix elements the quasi-real photon has an effective 'intrinsic' transverse momentum which can enhance the transverse momentum of the final state photon, giving a harder spectrum and a larger cross section at large p_T^γ. It may be concluded at this stage, therefore, that for untagged electrons the choice $\eta = \sqrt{S}/2m_e$ gives the best approximation to the large p_T^γ cross section, and that the residual errors are significantly smaller than the theoretical uncertainties in the photon-proton cross section.

It is interesting to investigate the energy dependence of the accuracy of the EPA in the untagged case. This has been performed for two values of the minimum transverse momentum of the photon, $10\,GeV/c$ and $50\,GeV/c$. In the first instance, the energies of the incoming electron and proton are set equal to each other and the invariant mass of the $M_{\gamma q}$ system is maintained at $20\,GeV/c$. The percentage errors are obtained, as in the last case, via

$$\%error = \frac{\sigma(approx) - \sigma(exact)}{\sigma(exact)} \times 100\% \qquad (3.57)$$

and the results are presented in figure 3.4. It is clear that the $\eta = E_e/m_e =$

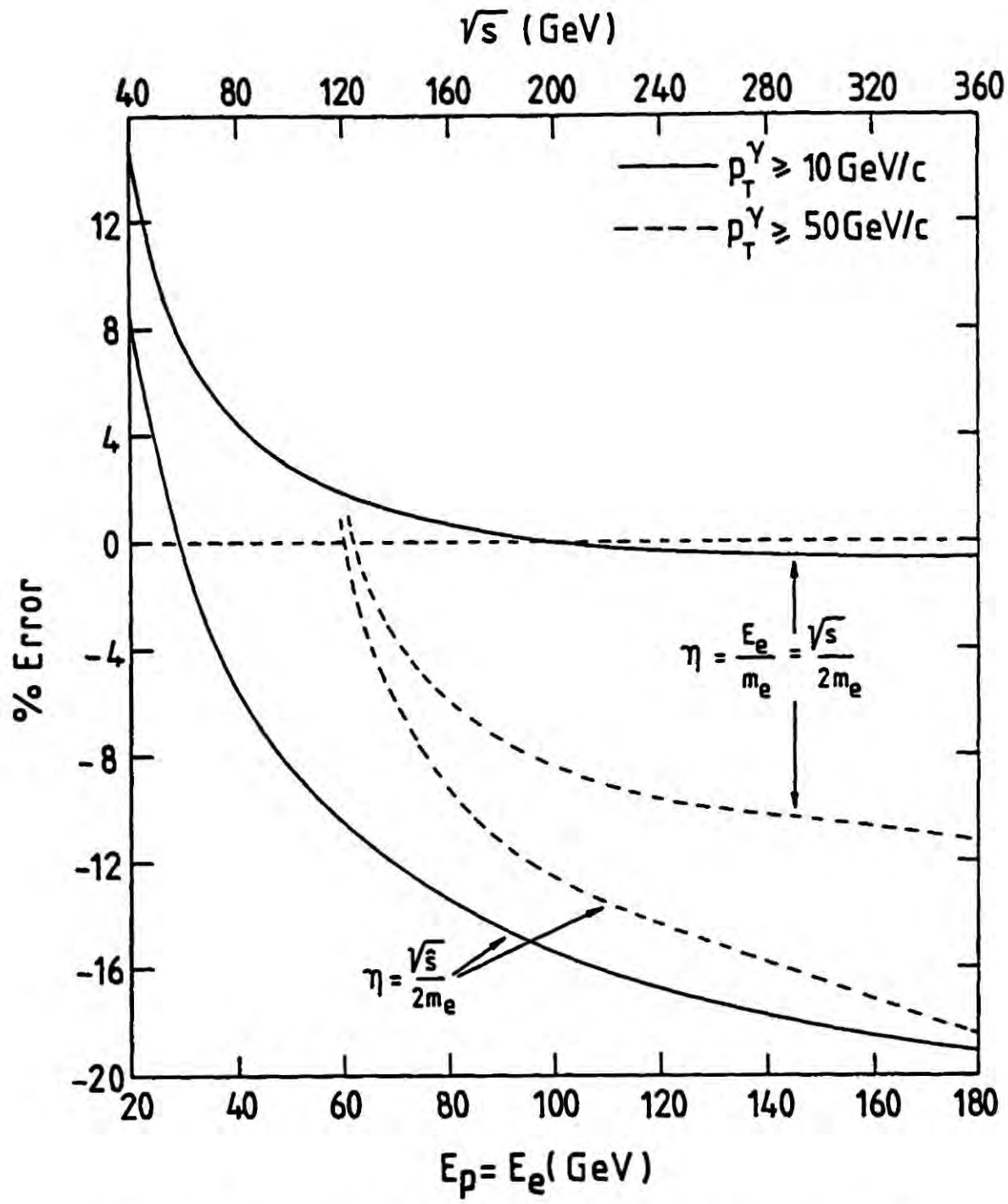

Figure 3.4 Percentage error from the equivalent photon approximation in the process $ep \rightarrow ep\gamma$ at high energy. The error is shown for two values of the final state photon minimum transverse momentum (10 GeV/c (solid curves) and 50 GeV/c (dashed curves)) as a function of the scattering energy, in the electron-proton centre-of-mass frame.

$\sqrt{S}/2m_e$ choices fare better in this energy range and become more efficient with increasing energy. With the higher p_T^γ cut the error increases to about -10%, indicating a weak dependence on the subprocess scattering energy. Note that the choice $\eta = \sqrt{\hat{s}}/2m_e$ is everywhere less accurate and gets steadily worse as the energy increases. There is a slight improvement with the higher p_T^γ cut, simply because $\ln \eta$ is larger.

To investigate this further the calculation was repeated, setting $E_p = 820\,GeV$

so as to examine the dependence of the $\eta = E_e/m_e$ choice on the electron energy for more HERA-like parameters. The results are then surprisingly good. The choice $\eta = \sqrt{S}/2m_e$ presents errors which are approximately -0.5% and this error is constant through the energy range considered. The results of this comparison are shown in figure 3.5. The loss of Lorentz invariance when $\eta = E_e/m_e$ is chosen is demonstrated by the fact that the behaviour of the E_e/m_e curve in this case is significantly different from the behaviour of the corresponding curve in figure 3.5. This clearly demonstrates that the parameter η cannot be chosen independently of the other four-momenta in the scattering process.

By a change of variables, the $\ln \eta$ term in the EPA may be recast in terms of an integral over the angle of the outgoing electron:

$$\int_0^{O(1)} \frac{d\theta^2}{\theta^2 + O(\eta^{-2})} \simeq 2\ln(\eta) + ... \tag{3.58}$$

in the high energy limit. If the outgoing electron can be detected at small angle then the limits in this intergral are replaced by the maximum and minimum scattering angles. Then providing $1 \gg \theta_{max} > \theta > \theta_{min} \gg \eta^{-1}$, the logarithm of η is replaced by $\ln(\theta_{max}/\theta_{min})$, i.e.

$$\int_{\theta^2_{min}}^{\theta^2_{max}} \frac{d\theta^2}{\theta^2 + O(\eta^{-2})} \simeq 2\ln(\frac{\theta_{max}}{\theta_{min}}) + ... \tag{3.59}$$

With this replacement of the logarithm in the electron structure function (3.17) a measure of the accuracy of the EPA in the case of a tagged electron may be obtained. Again the case of a minimum photon transverse momentum of $p_T^\gamma > 10\,GeV$ is taken with the energy parameters of the HERA collider. The results of the calculation are presented in table 2 for various ranges of the electron scattering angle (in milliradians).

In the milliradian angular range the approximation again works remarkably well. At large scattering angles the approximation breaks down, as expected, but the error is still not particularly large. Note that the last range in Table

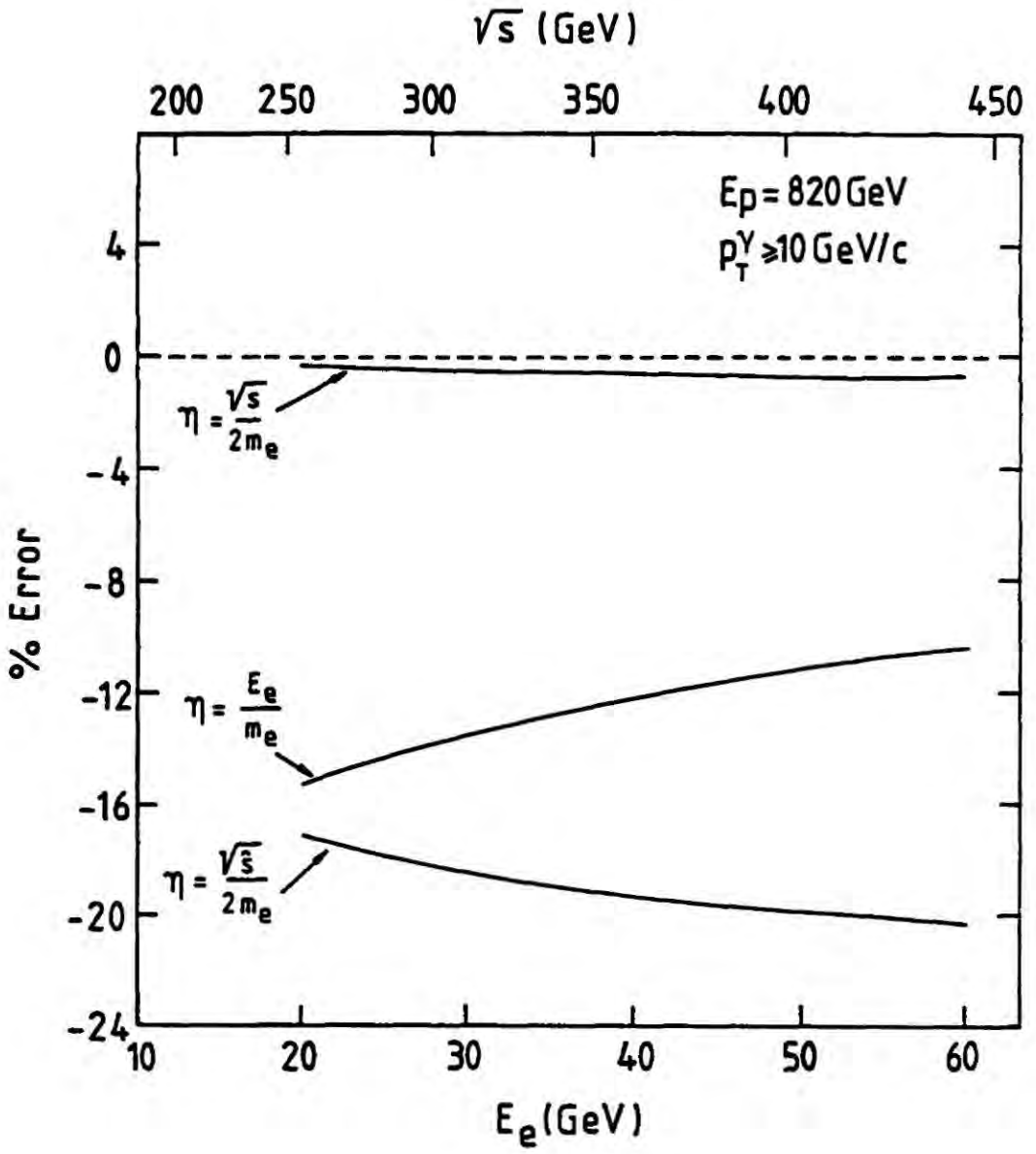

Figure 3.5 Percentage error from the equivalent photon approximation for a fixed value (820 GeV) of the proton energy and the final state photon minimum transverse momentum (10 GeV/c), as a function of the electron energy. The errors corresponding to three different choices of η are displayed.

2 corresponds to scattering angles between about 5 and 57 degrees. At very small scattering angles the approximation also breaks down, simply because the inequality $\theta_{min} \gg \eta^{-1}$ is no longer valid. The choice $\eta = \sqrt{s}/2m_e$ gives $\eta^{-1} \sim 10^{-6}$ at HERA energies and therefore a deviation may be expected when θ_{min} approaches this value. It would be straightforward to generalise the logarithm to incorporate a dependence on both η and the scattering angles in order to interpolate between the tagged and untagged situations. Note that the EPA cross sections are the same for each of the angular ranges in Table 2, since the

Table 2

θ_{min}	θ_{max}	% error
0.01	0.10	16.9
0.10	1.00	3.6
1.00	10.00	0.6
10.00	100.00	1.6
100.00	1000.00	27.5

logarithm in the electron structure function is the same (ln(10)) in each case.

The energy dependence of the EPA in the tagged case is investigated in the same way as for the untagged electron. The efficiency of the approximation is checked for three θ regions and these results are presented in Table 3. Again, the calculation is performed with a minimum p_T^γ of $10\,GeV/c$, the angular ranges are in milliradians and the errors are in percentages.

Table 3

$\sqrt{S}(GeV)$	$1-10$	10-100	100-1000
40	6.0	1.1	5.2
80	2.4	0.7	10.4
120	0.8	0.8	13.6
160	0.6	0.8	16.3
200	0.4	0.8	19.8
240	0.3	0.8	23.9
280	0.3	0.9	26.2
320	0.3	0.9	28.1
360	0.3	1.1	30.0

These results indicate that the EPA in the case of the tagged electron is very stable with respect to energy in the range $\theta = [1, 100]$ mrad. However, this is not very interesting for HERA parameters (at the early stages of HERA operation). The minimum tagging angle at HERA will be in the region of 6 deg [21]. To obtain a measure of the efficiency of the EPA (for the tagged case) in this region

Table 4

θ_{min}	θ_{max}	% error
6 deg	8 deg	5.1
8 deg	10 deg	7.4
10 deg	12 deg	9.7
12 deg	14 deg	12.6
14 deg	16 deg	15.6
16 deg	18 deg	17.9
18 deg	20 deg	23.8
20 deg	22 deg	28.4
22 deg	24 deg	30.9
24 deg	26 deg	35.7
26 deg	28 deg	44.0
28 deg	30 deg	46.4
30 deg	32 deg	48.5

the total cross-section is calculated in two-degree bins in both the exact and approximate cases and then compared. These results are contained in table 4.

The EPA is efficient to within 10% in the small θ region and breaks down in the large θ region. In this case as well, the EPA overestimates the total cross-section by the percentages in table 4 and this grows with θ_{min}.

3.6 Conclusions.

The accuracy of the equivalent photon approximation at HERA energies has been investigated by performing an exact calculation of the cross section for large transverse momentum photon production and comparing it with the approximate calculation using different choices of the variable η which enters in the electron 'structure function'. It has been shown that for the untagged case the choice $\eta = \sqrt{s}/2m_e$ works very well over a wide range of scattering energies and photon transverse momenta. The residual errors are significantly smaller than (i) the other $O(10-20\%)$ theoretical uncertainties due to higher order perturbative corrections and parton distribution uncertainties and (ii) the contributions at

smaller p_T^γ from the quark and gluon content of the quasi-real photon. It would be expected that these conclusions will also be valid for other hard scattering processes, such as the the production of large transverse momentum jets.

In the study of processes such as deep inelastic Compton scattering at HERA, the use of the EPA will be a useful tool in producing a realistic spectrum of photons in the initial state. This approach will be an alternative one to that used by Aurenche *et al.* [10], in which they adopt an average photon momentum.

As has been mentioned above, the smallest angle at which the final-state electron will be tagged is about 6 deg. Above this angle, the uncertainty introduced by the use of the tagged-EPA is well-established and up to an angle of 12 deg this is $< 10\%$. If the HERA detectors can cope with tagging at even smaller angles then the level of uncertainty introduced will be significantly smaller. Between 0.5 deg and 5 deg the uncertainty reduces to 1.6% and this improves at even smaller angles. The dependence of the tagged EPA on $\sqrt{S}$ is very small indeed.

REFERENCES

1. Proceedings of the HERA Workshop, ed. R. Peccei, DESY, Hamburg, 1987.
2. Z. Kunszt and W.J. Stirling, Proceedings of the HERA Workshop, ed. R. Peccei, DESY, Hamburg, 1987, page 331.
3. M. Drees and R.M. Godbole, Phys. Rev. **D39** (1989) 169.
4. P. Aurenche, R. Baier, M. Fontannaz and D. Schiff, Proceedings of the HERA Workshop, ed. R. Peccei, DESY, Hamburg, 1987, page 561.
5. A.C. Bawa and W.J. Stirling, Proceedings of the HERA Workshop, ed. R. Peccei, DESY, Hamburg, 1987, page 317; J. Phys. G. **14** (1988) 1353.
6. Z. Kunszt and W.J. Stirling, Phys. Lett. **217B** (1988) 563.
7. M. Drees and R.M. Godbole, Phys. Rev. Lett. **61** (1988) 682.
8. M. Glück, R.M. Godbole and E. Reya, Z. Phys. **C38** (1988) 441; erratum **C39** (1988) 590.
9. R.K. Ellis and Z. Kunszt, Nucl. Phys. **B303** (1988) 653.
10. P. Aurenche, R. Baier, M. Fontannaz and D. Schiff, Z. Phys. **C24** (1984) 309.
11. R.K. Ellis and P. Nason, Nucl. Phys. **B312** (1989) 551.
12. C.F. von Weizsäcker, Z. Phys. **88** (1934) 612.
13. E. J. Williams, Phys. Rev. **45** (1934) 729.
14. M.-S. Chen and P. Zerwas, Phys. Rev. **D12** (1975) 187.
15. R. Kleiss and W.J. Stirling, Nucl. Phys. **B262** (1985) 235.
16. R. Kleiss and W.J. Stirling, Phys. Lett. **B179** (1986) 159.
17. S.J. Brodsky, T. Kinoshita and H. Terazawa, Phys. Rev. **D4** (1971) 1532.
18. M. Landø, K.J. Mork and H.A. Olsen, Phys. Rev. **D36** (1987) 44.
19. R. Kleiss, W.J. Stirling and S.D. Ellis, Comput. Phys. Commun. **40** (1986) 359.

20. A.D. Martin, R.G. Roberts and W.J. Stirling, Phys. Rev. **D37** (1988) 1161.

21. Private communication with Prof. Poehls of DESY (June, 1989)

---

4. Photoproduction of High Transverse Momentum Photons at HERA

4.1 Introduction

As early as 1969, Bjorken and Paschos [1] suggested that the study of deep inelastic Compton scattering was a 'good way to find out about the internal structure of the proton'. Ever since then there has been great interest in the subject and many studies have been made of it [2-5]. Interest in the subject was renewed when plans were published for the building of the ep–collider called HERA, in Hamburg. Experimentation at HERA is scheduled to begin in 1990 with two major detectors, ZEUS and H1. The scattering of (almost) real photons off protons will be a significant fraction of the physics experimentation at the new collider.

In general, the study of hadronic scattering processes with large p_T in the final state is a good source of information relating to the short-distance structure of the hadrons. However, there is a multitude of partonic processes that contribute to these scattering cross-sections and very often it is difficult to extract unambiguous conclusions from them. If the interactions that are considered include photons as one of the external particles, then the number of contributing subprocesses decreases significantly. The situation improves further if the process that is considered is the photoproduction of large transverse momentum photons, so that there are photon couplings in the initial and final states. The unique feature of the photon as compared to the hadron in the initial and/or final states is that it has a pointlike coupling to the partons. It couples to the quark charge and so different subprocesses have different weightings and so there is the possibility that the different contributions to the cross-section may be untangled. An additional advantage in the utilization of deep inelastic Compton scattering as a probe is the smaller effect of the intrinsic transverse momentum, which for photoproduction gives rise to smaller corrections than for hadroproduction.

The (almost) real photon beam is defined in terms of the four momentum of the final-state electron. Then, in terms of the initial and final electron energies

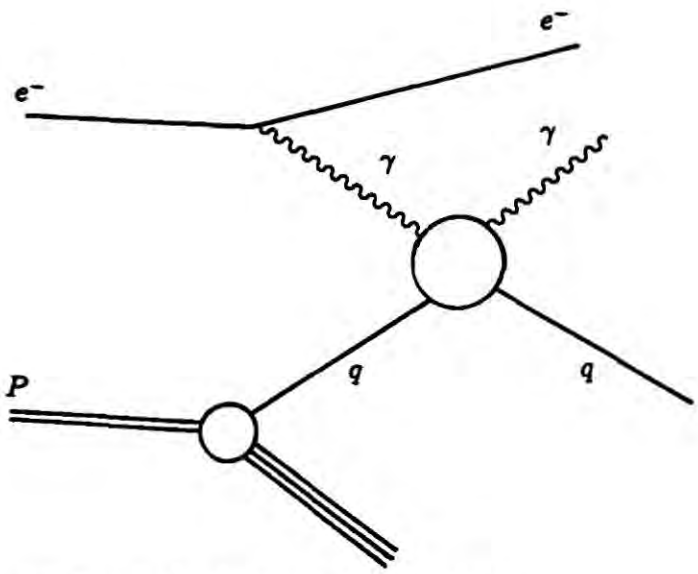

Figure 4.1 Deep inelastic Compton scattering.

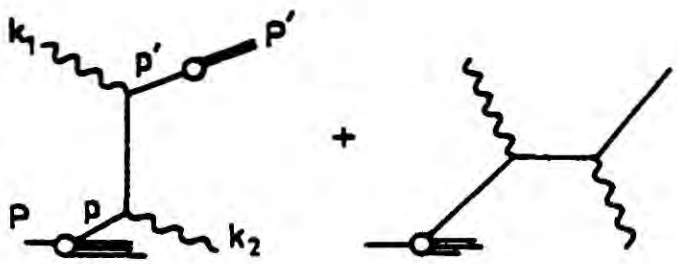

Figure 4.2 The Born-level diagram $\gamma + q \rightarrow \gamma + q$.

and the scattering angle of the electron, it is possible to write the following relations:

$$\begin{aligned} E_\gamma &= E_i - E_f \\ Q^2 &= 2E_iE_f(1 - \cos\theta), \end{aligned} \tag{4.1}$$

where E_γ is the photon energy and Q^2 the invariant mass of the virtual photon. For small angles the expression for Q^2 may be written as

$$Q^2 = E_iE_f\theta^2. \tag{4.2}$$

To obtain a measurement of Q^2, the values for E_f and θ have to be determined experimentally: the energy via calorimetry and the angle via solid-state detectors, perhaps. According to Engelen [6], these solid-state detectors will allow a measurement of θ down to 7 milliradians. However, as has been mentioned in chapter 2, this minimum angle (during the initial experiments) is more likely to be in the region of 100 milliradians. In this study it is assumed that tagging will not be efficient at small angles and the untagged EPA is used (see chapter 2).

Deep inelastic Compton scattering is generically described by the process

$$\gamma + proton \rightarrow \gamma + X. \tag{4.3}$$

In this study, the basic subprocess (see figure 4.2)

$$\gamma + q \rightarrow \gamma + q \tag{4.4}$$

is examined together with the QCD corrections up to $O(\alpha_s)$. These QCD-motivated corrections may be divided into two categories. The first includes all the additional contributions to the basic subprocess in (4.4) at leading-logarithm (or LL) level. The set of processes is shown in figure 4.3 are obtained by considering either the photon structure function or the quark- or gluon-photon fragmentation function (see section 4.2). A further set of these processes contains both the photon structure function and the fragmentation function (see figure 4.4). The final state signals in these LL processes are identical to the signals of the basic subprocess in (4.4). These processes have been considered by various authors [4,5] and several references will be made to these papers in the rest of this chapter. An additional $2 \rightarrow 2$ process that produces an identical final state - that is, a jet and a photon - is the gluon-photon fusion graph that proceeds via a quark box (see figure 4.5). This process has been studied by Combridge [7] and is included in this study.

The third category of processes represents the next-to-leading order in α_s corrections to the process in (4.4). These QCD corrections (see figure 4.6) are sufficiently straightforward to permit the inclusion of all the graphs up to $O(\alpha_s)$ and these are characterized by the processes

$$\begin{aligned} \gamma + q &\rightarrow \gamma + q + g \\ \gamma + g &\rightarrow \gamma + q + \bar{q}, \end{aligned} \tag{4.5}$$

with a photon and two jets in the final state and the interference between the $O(\alpha_s^2)$ virtual diagrams and the basic Compton subprocess. In chapter 1, it was seen that a similar high-p_T hadronic interaction was extremely complicated in

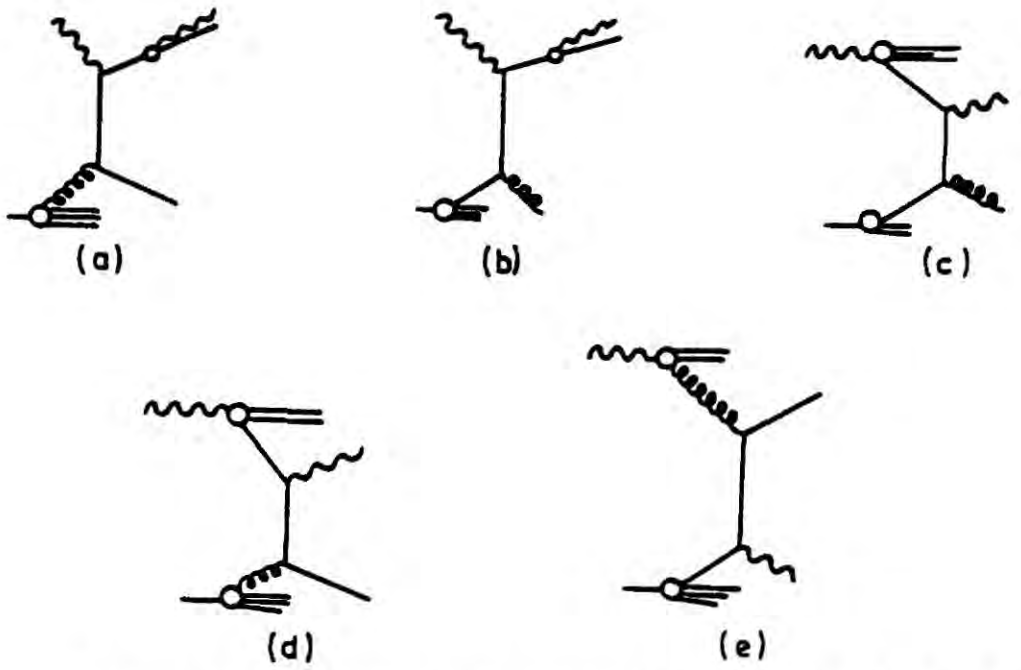

Figure 4.3 Leading-logarithm diagrams that contribute to $O(\alpha^2)$ with the final state quark fragmenting into a quark and photon OR the hadronization of the initial-state photon.

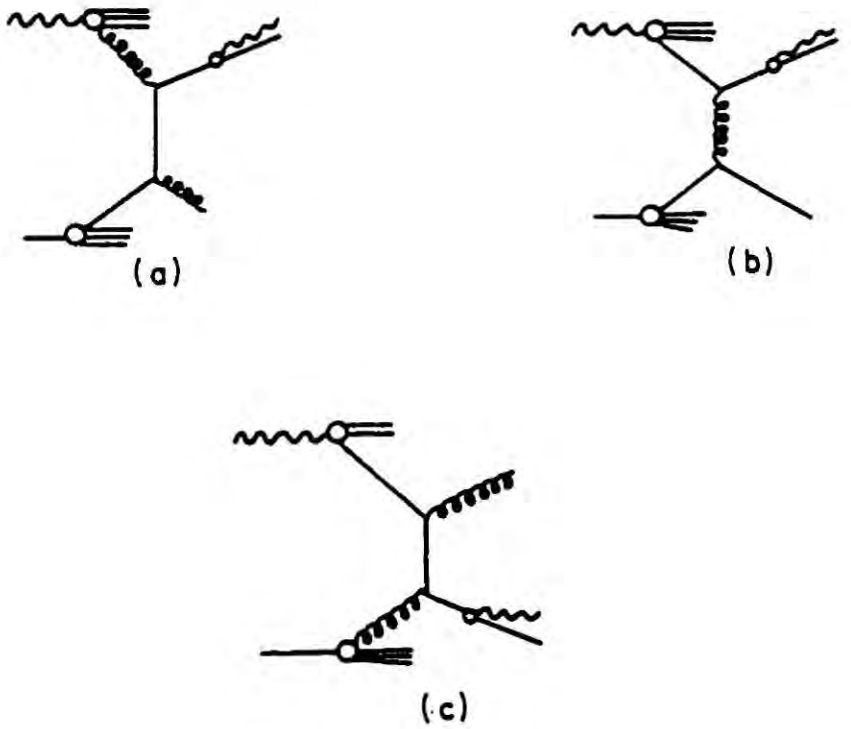

Figure 4.4 Leading-logarithm diagrams that contribute to $O(\alpha^2)$ with the hadronization of the initial-state photons AND the fragmentation of the final-state quark into a quark and a photon.

next-to-leading order and this indicates the usefulness of these initial-state and

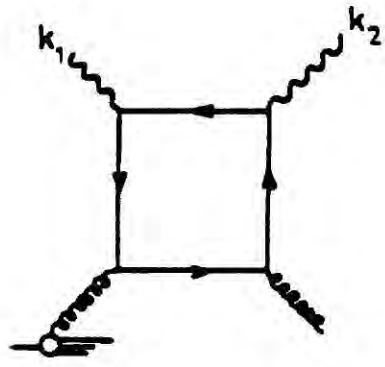

Figure 4.5 The box diagram $\gamma + gluon \rightarrow \gamma + gluon$.

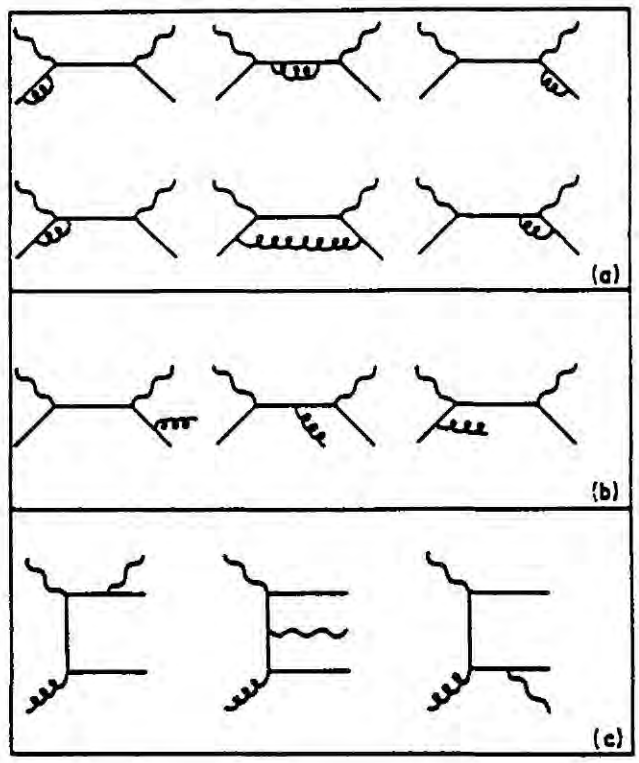

Figure 4.6 The diagrams that contribute to next-to-leading order in α_s.

final-state photon interactions. These graphs have been calculated by Duke and Owens [4] and by Aurenche *et al.* [5] and their results have been used in this study.

Aurenche *et al.* [5] have performed cross-section calculations of this process explicitly for HERA. However, they have used an average energy of 16 TeV for the photon beam. An alternate approach has been used in this study. The equivalent photon approximation is used to produce an energy spectrum of the photons for the kinematic parameters of HERA's experiments and the conclusions of the last chapter are utilized to provide some idea of the amount of uncertainty that this introduces.

The plan of this chapter is as follows. In section 4.2, the photon structure function is investigated and some idea of the validity of its application is presented. The $q \rightarrow q\gamma$ fragmentation function is also described in this section. The kinematics of the problem are dealt with in section 4.3, both for the leading and the next-to-leading order calculations. This is important because of the extremely asymmetrical nature of HERA's kinematics. In section 4.4, the subprocess matrix elements and the structure function definitions for the $O(\alpha_s)$ corrections are discussed. The numerical calculations are presented in section 4.5 and finally, some conclusions are drawn in section 4.6.

4.2 The Photon Structure Function

It is a well known fact that real photons, in most cases, behave as if they have hadronic properties; that is, the photons first hadronize and then interact with the partons in the proton. The corresponding Feynman diagrams are shown in figures 4.3 and 4.4 and it is clear that the final states are indistinguishable from that of the basic Compton subprocess if the photon beam fragments are of low energy and experimentally indistinguishable. This is true if the incident photon transfers a large fraction of its energy to the large-p_T final-state particles. This transfer is estimated to be in the region of 80-100% of the incoming photon's energy.

The hadronic properties of the photon are described by the QCD-improved parton model on condition that the photon is being investigated at large Q^2, which is usually the case when the final-state particles have a large invariant

mass or when final state has a large transverse momentum. In the case of any hadron the structure of the hadron is described by distribution functions $q_i(x, Q^2)$ which provide a measure of the probability of finding parton i in the hadron with momentum fraction x when the hadron is probed at scale Q^2. It is well known that in the hadronic case, the dependence of the q_i on the scale is described by the Altarelli-Parisi equations, which are solved with the requirement of an initial condition of the distribution at some scale Q_0^2 (obtained from experiment). x and Q^2 dependent parametrizations are then obtained for the parton structure of the hadron.

However, in the case of the photon structure function this procedure is somewhat more complicated. Witten [8] has shown that as $Q^2 \to \infty$, the quark and gluon distributions within a photon are exactly calculable. This deduction was continued to two-loop order by Bardeen and Buras [9]. DeWitt *et al.* [10] derived the leading-order evolution equations for the Q^2-evolution of these parton distributions and the asymptotic solutions to these equations lead to unphysical divergences at $x \to 0$, and it has been shown [9] that the degree of the pole increases with the order in perturbation theory. Gluck and Reya [11] suggested that, if distribution functions at some fixed Q_0^2 were introduced such that $F_2^\gamma(x, Q_0^2)$ were finite for all x, then the solution of the evolution equations would produce a finite F_2^γ at all values of Q^2. These functions at Q_0^2 are unknown and this implies that in QCD only the Q^2 dependence of the distribution functions will be known. It has been suggested [12] that the only parts of the distributions at Q_0^2 that should be retained are those parts that are necessary to regulate the divergences at small x. But the Q^2-dependence of this part of the distribution functions is small, it is not clear that this procedure will work. Theoretically, it is not yet determined whether the asymptotic solutions for the distributions are reliable. Gluck *et al.* [11] have indicated that they are unreliable if $x \leq 0.2$ or $Q^2 < 500\,GeV^2$ and for many applications one or both of these conditions are satisfied. Drees and Grassie [13] obtained new parametrizations using the full solution of the inhomogenous evolution equations, which are free of divergences.

The LL contributions are of the same order (in α and α_s) as the basic Compton subprocress since the photon structure function has a factor of $\alpha/\alpha_s(Q^2)$. In

this study only the asymptotic parton model solution and the Duke and Owens [4] parametrization are used for the parton distributions within the photon. The parton model prediction for this asymptotic quark distribution function is the following simple expression

$$G_{q/\gamma}(x,Q^2) = \ln(Q^2/\Lambda^2_{QCD})e_q^2\frac{\alpha}{2\pi}N_C \times [x^2 + (1-x)^2], \qquad (4.6)$$

where e_q is the electric charge of the quark and N_C is the number of colours. Of course, there is no analogous expression in the parton model for the gluon distribution in the photon. The Duke and Owens parametrizations for the quark and gluon distributions are presented in the appendix of reference [4].

The non-perturbative part of the photon structure function is usually described through the VDM (or vector dominance model). If this part of the photon structure function has to be taken into consideration a great amount of care should be taken since the constituent partons within the mesons have an intrinsic transverse momentum which will be of the order of 2 GeV/c. At SPS energies the VDM contribution is negligible [13] and it may be safely assumed that at HERA energies this effect is small enough to be ignored.

The $q \rightarrow \gamma$ fragmentation function has also been calculated in the naive parton model [8,14] and is given by

$$D_{\gamma/q}(z,Q^2) = \ln(Q^2/\Lambda^2_{QCD})e_q^2\frac{\alpha}{2\pi} \times \frac{1+(1-z)^2}{z}. \qquad (4.7)$$

Again, Duke and Owens [4] have performed a parametrization for this function and this is presented in the appendix of reference [8].

4.3 The Kinematics

The leading order case

The new *ep* collider at DESY examines the collisions between a 30 GeV electron beam and an 820 GeV proton beam and it is clear that the kinematics are very asymmetrical. For this reason, it was decided to perform the calculation in the laboratory system so that the rapidity distributions of the calculated cross-sections reflect this asymmetry. This discussion is divided into two parts: one for the $2 \to 2$ processes and the next for the $2 \to 3$ processes.

The general expression for the $2 \to 2$ differential cross-section is given by

$$\begin{aligned} & E\frac{d^3\sigma}{dk^3}(ep \to \gamma X) \\ & \quad = \sum_{a,b,c} \int dx_a dx_b \frac{dz_c}{z_c^2} dx_\gamma \times G_{\gamma/e}(x_\gamma) G_{b/p}(x_b, Q^2) G_{a/\gamma}(x_a, Q^2) D_{\gamma/q}(z_c, Q^2) \\ & \quad \times \frac{\hat{s}}{\pi}\frac{d\sigma}{d\hat{t}}(a+b \to c+d)\delta(\hat{s}+\hat{t}+\hat{u}), \end{aligned} \tag{4.8}$$

where $\hat{s}$, $\hat{t}$, and $\hat{u}$ are the partonic variables defined later in terms of the four-momenta of the external particles. As usual, $G_{b/p}(x_b, Q^2)$ represents the distribution function of parton b with momentum fraction x_b of the proton at momentum scale Q^2. $G_{a/\gamma}(x_a, Q^2)$ is the measure of the distribution of parton a within the initial-state photon with momentum fraction x_a of the photon momentum and $D_{\gamma/q}(z_c, Q^2)$ is the final-state quark to photon fragmentation function where z_c is the momentum fraction of the fragmented photon. Finally, $G_{\gamma/e}(x_d)$ is the electron 'structure function' based on the equivalent photon approximation, which has been studied in chapter 2.

There are four classes of subprocesses that must be included in (4.8).

(1). $a = c = \gamma$ and $b = q(\bar{q})$. This process is the Born Compton process at $O(\alpha^2)$. In this case, the photon structure function and the quark fragmentation function reduce to

$$G_{\gamma/\gamma}(x) = D_{\gamma/\gamma} = \delta(1-x). \tag{4.9}$$

(2). $a = \gamma$ and $b, c = q(\bar{q})$ or g. These processes involve the fragmenta-

tion of the final-state quark (or antiquark), into a quark (or antiquark) and a photon and are of $O(\alpha\alpha_s)$. However, the fragmentation functions $D_{\gamma/q,g}$ are of $O(\alpha/\alpha_s)$ leaving these processes with a net contribution of $O(\alpha^2)$. In this study the processes which depend on the gluon fragmentation are ignored.

(3). a and b=$q(\bar{q})$ or g. These processes involve the photon structure function which is at $O(\alpha/\alpha_s)$ and this again leaves the net contribution of these processes at $O(\alpha^2)$.

(4). a, b, and $c = q(\bar{q})$ or g. These processes involve convolution with both the photon structure functions and the fragmentation functions and are of order $\alpha_s^2 \times (\alpha/\alpha_s)^2$, giving $O(\alpha^2)$. Previous studies have indicated that these processes will possibly only be important at very small p_T and they have been ignored in this study. However, their contributions are considered in a study being carried out presently [15].

The discussion of the kinematics for the $2 \rightarrow 2$ processes is considered class by class. In the following, the generic process is given by

$$a + b \rightarrow c + d, \tag{4.10}$$

where a represents the photon or the photon-emitted parton, b is the proton-emitted parton and c is the final state photon or parton that fragments. The partonic variables are defined in the usual way as:

$$\begin{aligned} \hat{s} &= (p_a + p_b)^2 \\ \hat{t} &= (p_a - p_c)^2 \\ \hat{u} &= (p_b - p_c)^2. \end{aligned} \tag{4.11}$$

In the basic Compton process in class (1) (see figure 4.2), the relevant four-vectors are

$$\begin{aligned} p_a &= (0, x_e P_e; x_e P_e) \\ p_b &= (0, -x_p P_p; x_p P_p) \\ p_c &= (\mathbf{p_T^\gamma}, p_T^\gamma \sinh y^\gamma; p_T^\gamma \cosh y^\gamma), \end{aligned} \tag{4.12}$$

where x_e and x_p are the momentum fractions of the electron and proton carried away by the photon and parton, respectively. The partonic variables in terms of

(4.12) are

$$\begin{aligned}\hat{s} &= 4x_e x_p P_p P_e \\ \hat{u} &= -2x_e P_e p_T^\gamma \exp(-y^\gamma) \\ \hat{t} &= -2x_p P_p p_T^\gamma \exp(y^\gamma),\end{aligned} \tag{4.13}$$

where P_e and P_p are the energy of the electron and proton, respectively. Substituting these into the delta function in the cross-section expression (4.8) produces lower limits for x_e and x_p and upper and lower limits for y^γ in terms of the energies of the electron and proton and p_T^γ. These limits are:

$$\begin{aligned}\frac{2P_pP_e - \sqrt{4P_p^2P_e^2}}{2P_p p_T^\gamma} \leq \exp(y^\gamma) \leq \frac{2P_pP_e + \sqrt{4P_p^2P_e^2}}{2P_p p_T^\gamma} \\ \frac{P_e p_T^\gamma \exp(-y^\gamma)}{2P_pP_e - P_p p_T^\gamma \exp(y^\gamma)} \leq x_p \leq 1 \\ \frac{x_p P_p p_T^\gamma \exp(y^\gamma)}{2x_pP_pP_e - P_e p_T^\gamma \exp(-y^\gamma)} \leq x_e \leq 1.\end{aligned} \tag{4.14}$$

This δ function in (4.8) also produces a factor in the denominator of the cross-section expression given by

$$\frac{1}{4x_pP_pP_e - 2P_e p_T^\gamma \exp(-y^\gamma)}. \tag{4.15}$$

The kinematic limits for the contributions in class (2) are obtained in a similar fashion. However, the additional fragmentation parameter, z has to be taken into consideration and this is demonstrated now. In this case the relevant four-vectors are

$$\begin{aligned}p_a &= (0, 0, x_e P_e; x_e P_e) \\ p_b &= (0, 0, -x_p P_p; x_p P_p) \\ p_c &= (0, p_T, \frac{p_T \sinh y}{z}; \frac{p_T \cosh y}{z}).\end{aligned} \tag{4.16}$$

This leads to the following for the partonic variables:

$$\begin{aligned}\hat{s} &= 4x_e x_p P_e P_e \\ \hat{t} &= \frac{-2x_e P_e p_T \exp(-y)}{z} \\ \hat{u} &= \frac{-2x_p P_p p_T \exp(y)}{z}.\end{aligned} \tag{4.17}$$

Substituting (4.17) into the δ function in (4.8) produces exactly the same upper

and lower limits for the rapidity and for x_p. For z and x_e they are

$$\begin{aligned} \frac{x_p P_p p_T \exp(y) + P_e p_T \exp(-y)}{2 x_p P_e P_p} \leq & z \leq 1 \\ \frac{x_p P_p p_T \exp(y)}{2 x_p z P_e P_p - P_e p_T \exp(-y)} \leq & x_e \leq 1, \end{aligned} \tag{4.18}$$

where in this case the rapidity and transverse momentum refer explicitly to the rapidity and transverse momentum of the parton c which fragments into a nearly collinear parton and photon. As in the previous case, the δ function in (4.8) produces a factor in the denominator of the cross-section expression given by

$$\frac{1}{4 x_p P_p P_e - 2 P_e p_T \exp(-y)/z}. \tag{4.19}$$

Class (3) contributions are slightly more complicated. In these diagrams three momentum fractions appear, the two which have been introduced in classes (1) and (2) and the momentum fraction of the parton in the photon, designated as x_γ. The effective parton content of the electron (which produces the hadronizing photon) is given by

$$\begin{aligned} G_{q/e}(x) &= \int_0^1 dx_\gamma dx_e G_{\gamma/e}(x_e) G_{q,g/\gamma}(x_\gamma) \delta(x - x_\gamma x_e), \\ &= \int_x^1 \frac{dx_\gamma}{x_\gamma} G_{\gamma/e}(\frac{x}{x_\gamma}) G_{q,g/\gamma}(x_\gamma), \end{aligned} \tag{4.20}$$

where

$$x_e = \frac{x}{x_\gamma} \leq 1 \tag{4.21}$$

and the lower limit of the $x_\gamma-$integration is given by $x_\gamma \geq x$. x is some function f of the other kinematic variables. The full expression for the differential cross-section for the terms in class (3) is given by

$$\frac{d\sigma}{dp_T^2 dy} \sim \int_{x_p^{min}}^1 dx_p G_{q,g/p}(x_p, Q^2) \int_0^1 dx G_{q,g/e}(x, Q^2) \delta(\hat{s} + \hat{u} + \hat{t}) .... \tag{4.22}$$

By substituting (4.20) into (4.22) and by performing the $x-$integral the following

expression for the cross-section may be obtained

$$\frac{d\sigma}{dp_T^2 dy} \sim \int_{x_p^{min}}^{1} dx_p G_{q,g/p}(x_p, Q^2) \int_{f(x_p,..)}^{1} \frac{dx_\gamma}{x_\gamma} G_{\gamma/e}(x_e = g(x_p, x_\gamma, ...)) G_{q,g/\gamma}(x_\gamma, Q^2)....$$
(4.23)

The implementation of a Monte-Carlo simulation program, with VEGAS, is straightforward for the terms in classes (1) and (2). However, in the case of class (3) care has to be taken. The delta function in (4.20) produces the relationship

$$x_e = \frac{f(x_p, ..)}{x_\gamma}.$$
(4.24)

If further, the fraction $x_\gamma \equiv f^r$, where r is a VEGAS random number between 0 and 1, then (4.24) may be written as

$$\begin{aligned} x_e &= \frac{f(x_p, ...)}{x_\gamma} \\ &= f(x_p, ...)^{1-r}. \end{aligned}$$
(4.25)

This change in variable produces the Jacobian $dx_\gamma/x_\gamma = d\ln x_\gamma = \ln f dr$. The limits for x_γ, x_p and the rapidity are identical to the limits for the calculation in class (1).

The phase space configuration for the box diagram is identical to that for the basic $2 \rightarrow 2$ Compton diagram.

The next-to-leading order case

There are $2 \rightarrow 2$ and $2 \rightarrow 3$ processes that contribute to the cross-section at order-$\alpha^2\alpha_s$ and the general expression for the cross-section is

$$\begin{aligned} E_\gamma \frac{d\sigma}{dK_\gamma} =& \frac{1}{\pi} \int dx_a \int dx_b \frac{\alpha_s(Q^2)}{2\pi} \frac{1}{\hat{s}} \\ & [G_{q/p}(x_b, Q^2) K(\hat{s}, \hat{t}, \hat{u}, Q^2) + G_{g/p}(x_b, Q^2) \times K'(\hat{s}, \hat{t}, \hat{u}, Q^2)] \\ & \times G_{\gamma/e}(x_a) \times \theta(\hat{s} + \hat{t} + \hat{u}), \end{aligned}$$
(4.26)

where K and K' are the next-to-leading order matrix elements and Q^2 is the

QCD scale which we discuss in section 4.5. The treatment of the $2 \rightarrow 3$ body kinematics here follows closely that of Aurenche *et al.* [5].

The kinematics for the two-body phase space are as for case of the basic Compton term. Now consider the process

$$p_a + p_b \rightarrow p_c + p_d + p_e, \tag{4.27}$$

where p_a and p_c are the momenta of the initial- and final-state photons, respectively. If s_2 is the invariant mass of the system recoiling against the photon in the final state, then the partonic variables may be described as

$$\begin{aligned} \hat{s} &= (p_a + p_b)^2 \\ \hat{t} &= (p_a - p_c)^2 \\ \hat{u} &= s_2 - \hat{s} - \hat{t}. \end{aligned} \tag{4.28}$$

Then it is possible to introduce rescaled variables

$$\begin{aligned} v &= 1 + \frac{\hat{t}}{\hat{s}} \\ V &= 1 + \frac{T}{S} \\ w &= \frac{-\hat{u}}{\hat{s} + \hat{t}} \\ W &= \frac{-U}{S + T}, \end{aligned} \tag{4.29}$$

where S, T and U are the usual hadronic variables.

The momentum fractions, x_e and x_p may be restated as

$$\begin{aligned} x_e &= \frac{VW}{vw} \\ x_p &= \frac{1 - V}{1 - v}, \end{aligned} \tag{4.30}$$

which permits (4.26) to be rewritten as

$$E_c\frac{d\sigma}{dp_c} = \frac{1}{\pi}\frac{S}{p_T^4}\int_{VW}^{V} dv \int_{VW/v}^{1} dw x_e^2 x_p^2 v[v(1-v)w] \times \left[G_{q/p}(x_p,Q^2)\times K(\hat{s},\hat{t},\hat{u},Q^2) + G_{g/p}(x_p,Q^2)\times K'(\hat{s},\hat{t},\hat{u},Q^2)\right] \times G_{\gamma/e}(x_e). \tag{4.31}$$

This expression has been checked against the corresponding expression in reference [16] (for $p\bar{p}$ $2 \rightarrow 3$ cross-sections) and found to be identical. The integration limits in (4.31) are obtained in the usual manner by utilizing the θ–function in (4.26) :

$$\hat{s} + \hat{t} + \hat{u} \geq 0$$

and this produces the relevant limits. The implementation of the program VEGAS in this case is straightforward.

4.4 The Matrix Elements

The full set of matrix elements (except that for the box diagram) are given by Aurenche *et al.* [5] and these have been checked against those of Duke and Owens [4]. In the former, these matrix elements are calculated in n-dimensions and in this summary they are presented only as functions of $\hat{s}, v$ and w. To make contact with (4.8) it is noted that

$$\frac{d}{dv} = \frac{1}{\hat{s}}\frac{d}{d\hat{t}}.$$

The Born diagram

The hard-process cross-section for the Born term (shown in figure 4.2) is

$$\frac{d\sigma}{dv} = \frac{2\pi\alpha^2 e_q^4}{\hat{s}} \times \frac{1+v^2}{v}, \tag{4.32}$$

where e_q is the charge of the quark. The fact that this process couples to the

fourth power of the charge of the quark means that it may be used to determine the charge of the quarks.

The quark fragmentation diagrams

These processes, shown in figure 4.3a,b involve a photon and a parton in the initial channel. The hard-process in diagram (a) is

$$\gamma + g \rightarrow q + \bar{q}, \tag{4.33}$$

where the quark (antiquark) may fragment into a quark (antiquark) and a photon. The matrix elements for the hard-process are given by

$$\frac{d\sigma}{dv}(\hat{s}, v) = \frac{\pi\alpha\alpha_s e_q^2}{\hat{s}} \times [\frac{v}{1-v} + \frac{1-v}{v}] \tag{4.34}$$

The hard-process in diagram (b) is

$$\gamma + q(\bar{q}) \rightarrow q(\bar{q}) + g, \tag{4.35}$$

This process appears to be identical to the basic Born process with the final-state photon replaced by a gluon. However, this is not true. A $t \leftrightarrow u$ transformation is required since in the Born diagram the final-state photon corresponds to particle c in $a + b \rightarrow c + d$ whereas in this diagram the gluon corresponds to the particle d. The hard-process cross-section is then given by

$$\frac{d\sigma}{dv}(\hat{s}, v) = \frac{2\pi\alpha\alpha_s e_q^2}{\hat{s}} C_F \times [\frac{1+(1-v)^2}{1-v}]. \tag{4.36}$$

(4.34) and (4.36) are then convoluted with the proton structure functions (or the structure functions of the isoscalar target in the case of the NA14 data), with the electron 'structure function' and with the $quark \rightarrow quark + \gamma$ fragmentation function. In this study, the $gluon \rightarrow gluon + \gamma$ fragmentation processes have been left out as they are only expected to contribute at at very small p_T.

The photon structure function diagrams

The hard-processes for these terms, shown in figure 4.3c-e, involve a parton derived from a photon (particle (a)) and a parton derived from a proton (particle (b)). The process indicated in diagram (c) is

$$q + \bar{q} \rightarrow \gamma + g. \tag{4.37}$$

This process is the time-reversed reaction of (4.33) and, up to colour factors, has the identical matrix elements, given by

$$\frac{d\sigma}{dv}(\hat{s}, v) = \frac{2C_F}{N_C}\frac{\pi\alpha\alpha_s e_q^2}{\hat{s}} \times [\frac{v}{1-v} + \frac{1-v}{v}] \tag{4.38}$$

The process in diagram (d) is

$$q(\bar{q}) + g \rightarrow \gamma + q(\bar{q}). \tag{4.39}$$

This is the time-reversed process of (4.35) and again simply requires an adjustment to the colour factors. The hard-process cross-section is given by

$$\frac{d\sigma}{dv}(\hat{s}, v) = \frac{\pi\alpha\alpha_s e_q^2}{N_C\hat{s}} \times [\frac{1+(1-v)^2}{1-v}], \tag{4.40}$$

where N_C is the number of colours.

Finally, the process in diagram (e) is

$$g + q(\bar{q}) \rightarrow q(\bar{q}) + \gamma. \tag{4.41}$$

As in previous cases this process is identical to the Born diagram up to colour factors and a $t \leftrightarrow u$ change. It is given by

$$\frac{d\sigma}{dv}(\hat{s}, v) = \frac{\pi\alpha\alpha_s e_q^2}{N_C\hat{s}} \times [\frac{1+(1-v)^2}{1-v}] \tag{4.42}$$

As usual, these contributions are folded in with the proton (or isoscalar target) structure functions the electron 'structure function' and the photon structure functions. As has been mentioned previously, those diagrams that contain both the photon hadronization and quark fragmentation have been ignored in this study.

The box diagrams

The hard-process cross-section for the box diagram is given by

$$\frac{d\sigma}{dv} = \frac{1}{16\pi\hat{s}}\frac{1}{4}[\sum_{\lambda}|\mathcal{M}_{c,\lambda}|^2] \times C \times F, \tag{4.43}$$

where the sum runs over all particle helicities and C, F are the associated colour and flavour factors for the subprocess. The factor of $\frac{1}{4}$ is a result of averaging over the initial-state helicities.

The relevant subprocess for this study is

$$\gamma + g \rightarrow \gamma + g, \tag{4.44}$$

via a quark box (see figure 4.6). For this diagram the C in (4.43) is given by

$$\begin{aligned} C =& \frac{1}{16} Tr(\lambda^a\lambda^b) Tr(\lambda^a\lambda^b) \\ =& \frac{1}{16} \times 2\delta_{ab} \times 2\delta_{ab} \\ =& 2. \end{aligned} \tag{4.45}$$

A factor of 1/8 must be included to average over the initial gluons. The flavour factor F in (4.43) arises out of the coherent sum over the different flavour loops and this is given by

$$F = [\sum_{N_f} e_q^2]^2. \tag{4.46}$$

Putting (4.45) and (4.46) into (4.42) the following expression is obtained for $N_f = 4$

$$\frac{d\sigma}{dv} = \frac{1}{16\pi\hat{s}}\frac{1}{4}[\sum_{\lambda}|\mathcal{M}_{c,\lambda}|^2] \times \frac{2}{8} \times \frac{100}{81}, \tag{4.47}$$

In this study, the matrix element squared has been constructed from the basis of linear polarisation states [7,17]. In the following '1' refers to the polarisation direction perpendicular to the scattering plane and by '2' is meant the direction

of the vector $\mathbf{2} = \mathbf{k} \times \mathbf{1}/k$, where $\mathbf{k}$ is the 3-momentum of the photon. The matrix element squared for the box diagram is given by

$$\sum_{\lambda} |\mathcal{M}_{\lambda}|^2 = |\mathcal{M}_{11\to 11}|^2 + 2|\mathcal{M}_{11\to 22}|^2 + |\mathcal{M}_{22\to 22}|^2 + 2|\mathcal{M}_{12\to 12}|^2 + 2|\mathcal{M}_{12\to 21}|^2. \tag{4.48}$$

Fontannaz and Schiff [17] obtain this expression by invoking time-reversal invariance and symmetry relations. The various helicity amplitudes are given by Combridge in reference [7], except for the $12 \to 21$ contribution which is easily obtained from symmetry arguments to be

$$\mathcal{M}_{12\to 21}(\hat{s}, \hat{t}, \hat{u}) = \mathcal{M}_{12\to 12}(\hat{s}, \hat{u}, \hat{t}).$$

This completes the hard-process cross-section, which as usual is convoluted with the gluon distribution function within the proton and the photon distribution within the electron.

The $O(\alpha_s)$ contribution

In this section a short description of the calculation performed by Aurenche *et al.* [5] is given. Much of this discussion follows and supplements the discussion on the $O(\alpha_s^2)$ calculation of Ellis *et al.* [18] and Arnold and Reno [19] in chapter 1. The generic forms of the processes that contribute to the $O(\alpha_s)$ cross-section are

$$\begin{aligned} \gamma + q &\to \gamma + X, \\ \gamma + g &\to \gamma + X, \end{aligned} \tag{4.49}$$

and the cross-section expression that is used is

$$\begin{aligned} E_\gamma \frac{d\sigma}{d^3\mathbf{k}_\gamma} = \int dx_e G_{\gamma/e}(x_e) \sum_q \int dx_p \Big[& G_{q/p}(x_p) \\ & \times \Big(\frac{\hat{s}}{\pi} \frac{d\sigma}{d\hat{t}}(\gamma + q \to \gamma + q) \delta(\hat{s} + \hat{t} + \hat{u}) + \frac{\alpha_s}{2\pi} \frac{1}{\pi} \frac{k(\hat{s}, \hat{t}, \hat{u})}{\hat{s}} \theta(\hat{s}, \hat{t}, \hat{u}) \Big) \\ & + G_{g/p}(x_p) \frac{\alpha_s}{2\pi} \frac{1}{\pi} \frac{k'(\hat{s}, \hat{t}, \hat{u})}{\hat{s}} \theta(\hat{s}, \hat{t}, \hat{u}) \Big]. \end{aligned} \tag{4.50}$$

k refers to the $O(\alpha_s)$ QCD-improved hard cross-section with $\gamma + q$ in the incoming

channel. The contributions to k are twofold. The $O(\alpha_s^2)$ diagrams in figure 4.6 interfere with the zeroth-order basic Compton term to produce the virtual $O(\alpha_s)$ contribution to (4.50). The real diagrams in figure 4.6 constitute the rest of k and they are of the form

$$\gamma + q \rightarrow \gamma + q + g. \tag{4.51}$$

The diagrams that contribute to k' are also shown in figure 4.6 and they have the form

$$\gamma + g \rightarrow \gamma + q + \bar{q}. \tag{4.52}$$

Diagrams that are of higher order in α_s but which contribute to order α_s when convoluted with the photon structure function are ignored. It has been argued [4,5] that these contributions are small.

In (4.50) k and k' are calculated perturbatively. To extract the full $O(\alpha_s)$ corrections from k and k' the factorization theorem (discussed in chapter 1) has to be invoked. This involves defining the choice of parton distribution functions (with which the hard-process perturbative cross-sections are convoluted) since k and the genuine $O(\alpha_s)$ corrections are related through the bare, scale-independent distribution functions $G(x_p)$ and the dressed, scale-dependent distribution functions, $G(x, Q^2)$. For completion, the description of the parton distribution function definitions is repeated here.

As was shown in chapter one, all higher order corrections to deep inelastic scattering are included in the definition of the parton distribution functions. So, for instance

$$\frac{F_2(x,Q^2)}{x} = \sum_q e_q^2 G_{q/p}(x,Q^2), \tag{4.53}$$

with (see chapter 1)

$$\begin{aligned} G_{q/p}(x,t) =& G_{q/p}(x) + \int \frac{dy}{y}\Bigg[\left(\frac{\alpha_s}{2\pi} t P_{qq}(\frac{x}{y}) + \alpha_s f_{qq}(\frac{x}{y})\right) \times G_{q/p}(y) \\ & \left(\frac{\alpha_s}{2\pi} t P_{qg}(\frac{x}{y}) + \alpha_s f_{qg}(\frac{x}{y})\right) \times G_{g/p}(y)\Bigg]. \end{aligned} \tag{4.54}$$

In this expression the usual definitions hold for t and the Altarelli-Parisi splitting functions, P_{qq} and P_{qg}. The form of the functions f depends on the manner in

which the mass singularities in the hard-process are dealt with. In [5] the mass singularities are handled with dimensional regularization and in this case the form of the function f_{qq} is

$$\alpha_s f_{qq}(z) = \alpha_s f'_{qq}(z) + \frac{\alpha_s}{2\pi}\left[-\frac{1}{\epsilon} + \gamma_E - \ln 4\pi\right] P_{qq}(z). \tag{4.55}$$

The form of $\alpha_s f'_{qq}(z)$ and P_{qq} have already been given in chapter 1. The form of f_{qg} is very similar,

$$\alpha_s f_{qg}(z) = \alpha_s f'_{qg}(z) + \frac{\alpha_s}{2\pi}\left[-\frac{1}{\epsilon} + \gamma_E - \ln 4\pi\right] P_{qg}(z). \tag{4.56}$$

and, again, α_s, f_{qg} and P_{qg} are given in chapter 1.

Another convention for the definition of the parton distributions is provided in [20] and [21]. In this convention none of the higher order terms to $O(\alpha_s)$ appear in the Altarelli-Parisi equations. Instead, they are included, for each parton subprocess, in the hard process cross-section and this alters the relationship between G and F_2 in (4.53). In this case $f'_{qq} = f'_{qg} = 0$. This is the so-called universal, process independent definition of the parton distribution functions.

To $O(\alpha_s)$, these two definitions lead to the same physical cross-section. The connection between the full $O(\alpha_s)$ and the perturbative $O(\alpha_s)$ corrections is presented in equation (25) of reference [5].

The same choices exist for the photon structure function and the quark fragmentation function. The photon structure functions of Duke and Owens [4] are a result of a leading log analysis of the available data and this leads to a non-universal choice for the definition of parton distribution functions in the photon. The expressions for $f_{q/\gamma}$ are obtained from the relevant gluon expressions for these functions [22,23].

The $O(\alpha_s)$ elastic diagrams, that is, the interference between the basic Compton diagram and the virtual corrections to this diagram, have been calculated in [5] in the Feynman gauge and the ultraviolet and infrared divergences are handled with dimensional regularization. The full expression for the $O(\alpha_s)$ matrix elements are presented in the appendix of the Aurenche *et al.* paper [5] and they have been used in this calculation.

4.5 Numerical Results

In the cross-section calculations that follow the nucleon structure functions of Martin, Roberts and Stirling [24], which have been discussed in chapter 1, have been used. For the photon structure functions and the quark fragmentation function, the leading log analysis of Duke and Owens [4] is utilised. For the entire calculation, the QCD scale is set at $Q = p_T^\gamma$. The universal definition for the parton distribution functions (discussed in the last section) has been implemented; that is the functions f'_{qq} and f'_{qg} have been set to zero, in accordance with the choice made in [24].

The first experimental results on the inclusive photoproduction of prompt photons at high transverse momenta were presented by the NA14 collaboration at CERN [25]. This experiment was performed at the CERN SPS in the E12 $e - \gamma$ beam. The bremsstrahlung photon beam results from an electron beam of average energy 140 GeV. The mean energy of the photon beam is 80 GeV. The data were collected off an isoscalar Li^6 target and a $y \geq -1.0$ rapidity cut is made. For this particular calculation, the electron 'structure function', is switched off, the initial photon energy is set at 80 GeV and the rapidity cut is included. The dashed curve in figure 4.7 is the cross-section of the basic Compton process, $\gamma + q \rightarrow \gamma + q$ and it lies consistently below the data points. However, there is good agreement between the data and the $O(\alpha_s)$ calculations, providing some confidence to extend this study to HERA energies.

As has been indicated in section 4.3, the cross-section calculations for HERA have been performed in the ep laboratory frame. The first quantity considered is the differential cross-section $d\sigma/dp_T^\gamma$, where p_T^γ is the transverse momentum of the final-state photon. This quantity was calculated with the MRS1 set of structure functions and the differential cross-section is shown in figure 4.8. One purpose of this study was to determine if the study of the deep inelastic Compton processes were experimentally feasible at HERA and this involves the calculation of an expected event rate. If an integrated luminosity of 100 pb^{-1} per year is assumed, the cross-section in figure 4.8 indicates that it will be measurable (meaning about one event per 1 GeV/c bin) out to a $p_T^\gamma = 50$ GeV/c. The corresponding upper limit for a measurable cross-section at the NA14 experiment is $p_T^\gamma = 4.5$ GeV/c.

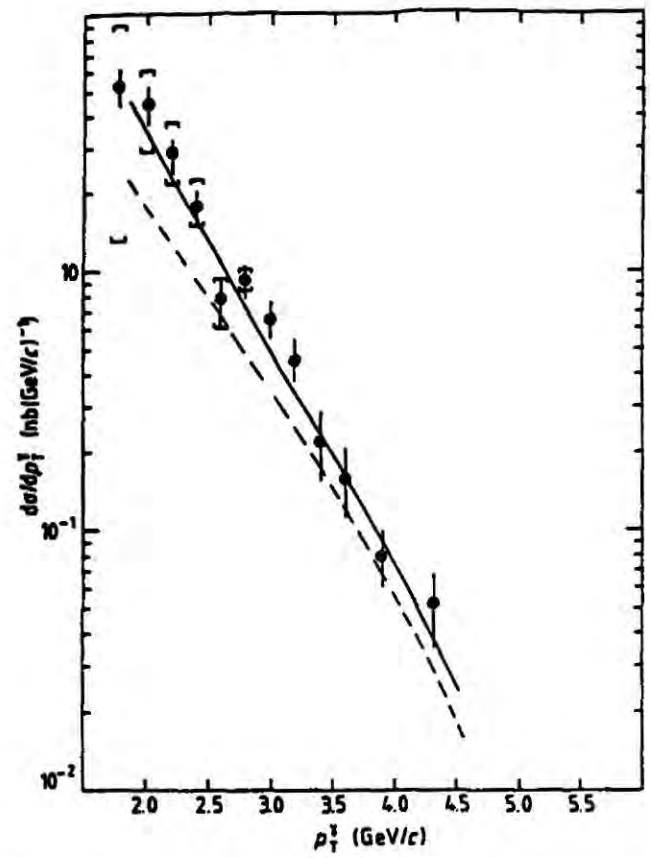

Figure 4.7 Comparison with data from the NA14 experiment: $d\sigma/dpt^\gamma$ as a function of p_T^γ for $\gamma + isoscalar\ \ target \rightarrow \gamma + X$, $E_\gamma = 80\ GeV$ and $y \geq -1.0$ in the centre-of-mass frame. The square error brackets indicate the systematic errors. The broken curve is the QED Compton contribution while the full curve is the fully corrected QCD cross-section.

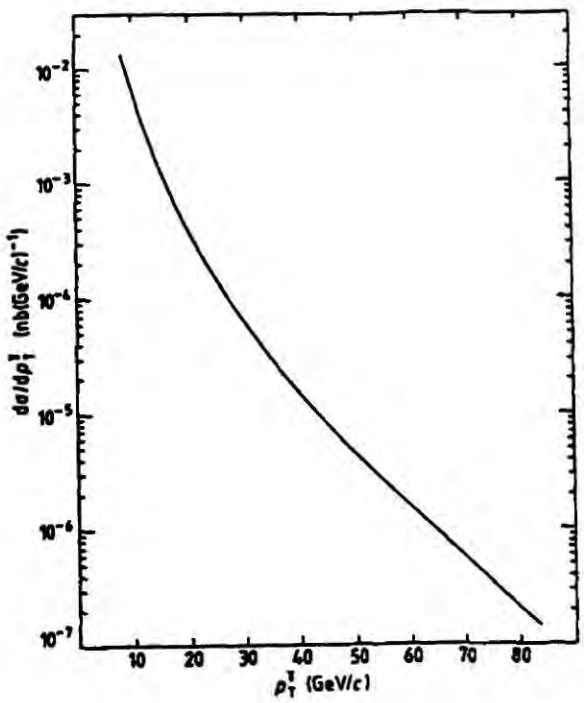

Figure 4.8 The complete next-to-leading-order prediction for $d\sigma/dp_T^\gamma$ as a function of p_T^γ at HERA, as described in the text. $\sqrt{S} = 314$ GeV.

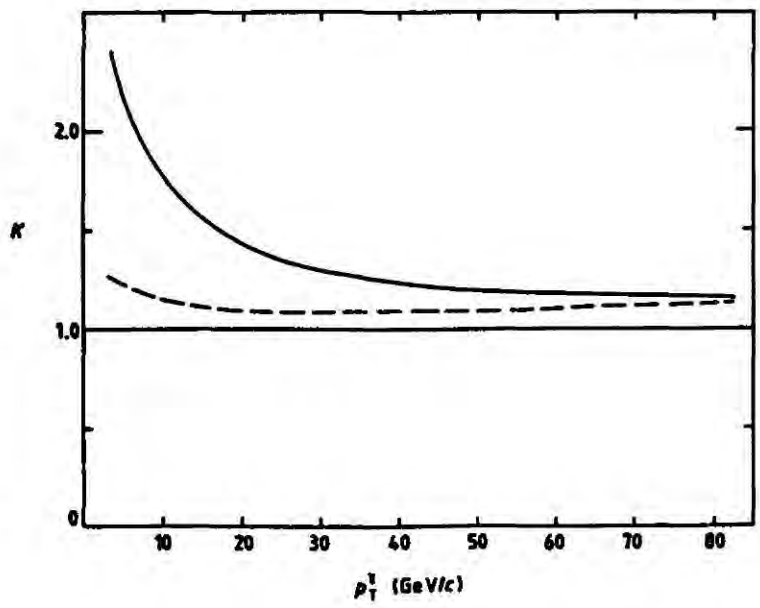

Figure 4.9 Contributions to the photon p_T^γ distribution normalized to the leading-order QED Compton contribution. The full curve represents the sum of the Compton, leading logarithm, box and $O(\alpha_s)$ contributions and the broken curve represents the sum of the Compton and $O(\alpha_s)$ contributions.

The relative importance of the leading log corrections and the higher order corrections are given in figure 4.9. The quantities plotted are the ratios

$$K_1 = \frac{d\sigma/dp_T^\gamma\left[\text{ Compton term + LL terms + box terms + } O(\alpha_s)\right]}{d\sigma p_T^\gamma\left[\text{Compton term}\right]}$$
$$K_2 = \frac{d\sigma/dp_T^\gamma\left[\text{Compton term + } O(\alpha_s)\right]}{d\sigma/dp_T^\gamma\left[\text{Compton term}\right]}, \tag{4.57}$$

plotted against p_T^γ. These curves indicate that the higher order processes are particularly important at small p_T^γ. At large p_T^γ their contribution is fairly constant and of the order of 20% and under control.

As has been described in chapter 1, MRS1 is the soft gluon set of structure functions with $\Lambda_{QCD}(\equiv \Lambda_{\overline{MS}}) = 107\ MeV$. The calculation has been repeated with other structure function sets. However, on the logarithmic-scale of figure 4.8 the sensitivity of the differential cross-section, $d\sigma/dp_T^\gamma$, to the structure functions cannot be demonstrated. This dependence on the different MRS parton distributions is shown in figures 4.10 and 4.11. The MRS2 set, which has $\Lambda_{QCD} = 250$

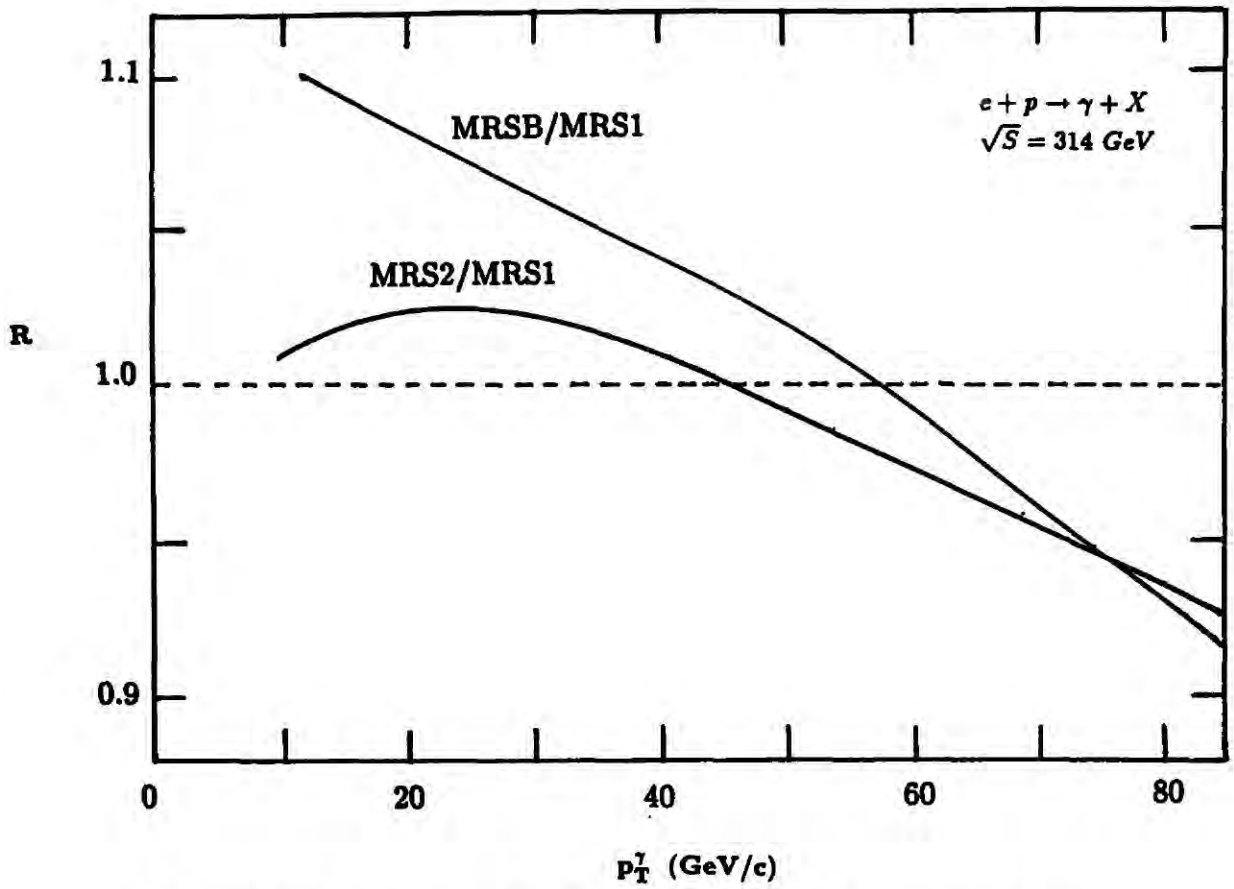

Figure 4.10 Dependence of the Born term differential cross-section on the choice of parton distributions MRS1, MRS2 and MRS3 normalized to the MRS1 prediction.

MeV, is a hard gluon set while the MRS3 set has $\Lambda_{QCD} = 178\ MeV$ with a $1/\sqrt{x}$ gluon distribution. Figure 4.10 shows the dependence of the Born term on the structure functions. The Born contribution to the cross-section is dependent purely on the quark distributions in the proton. In fact, since the quark charges enter the cross-section expressions in the fourth power, it is the up-quark distribution that dominates this dependence. The $x-$values that are probed in this process are $O(10^{-1})$. In this range the valence quark distributions in MRS1 and MRS2 are very similar and so the Born contributions to the cross-section with these distributions are very similar.

In figure 4.11, the structure function dependence of the corrected cross-section is demonstrated. When the leading log and higher-order corrections are switched-on, the gluon contribution to the cross-section is $O(35\%)$. At an x-value of $\sim 10^{-2}$ (corresponding to $p_T^\gamma \sim 10\ GeV/c$), the MRS2/MRS1 gluon ratio is about 0.8 and at an x-value of $\sim 10^{-1}$, (corresponding to $p_T^\gamma \sim 30\ GeV/c$) this ratio is $\simeq 2$. This is mirrored in figure 4.11 by the sharp decrease in the ratio (of the fully-corrected cross-section) at small p_T^γ and by the peak in the ratio at $\simeq 25$ GeV/c, which is larger than the peak in the corresponding Born term ratio by a

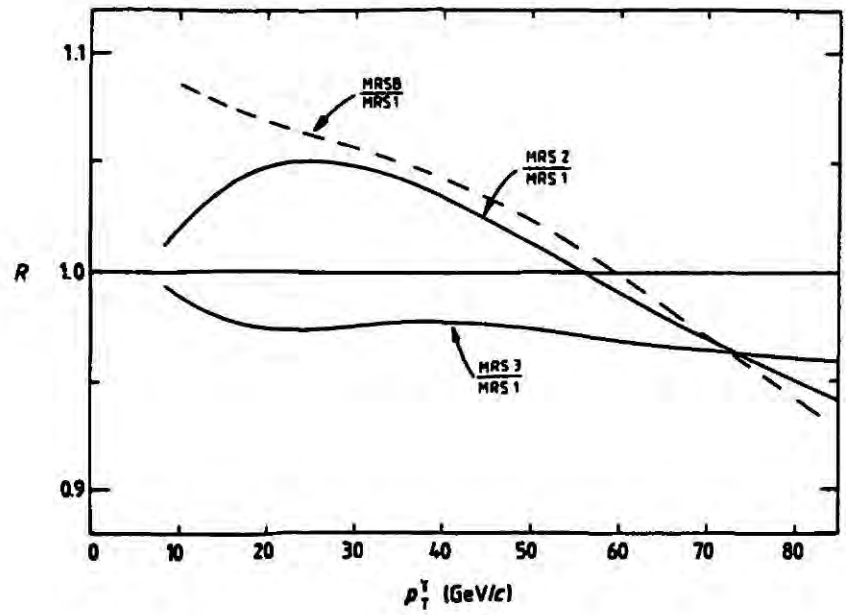

Figure 4.11 Dependence of the fully corrected differential cross-section on the choice of parton distributions MRS1, MRS2 and MRS3 normalized to the MRS1 prediction.

factor of about 2.

Since the three distribution sets, MRS1,2 and 3, are fitted to the same deep inelastic scattering data, it is not surprising that they give similar cross-sections. However, recent deep inelastic scattering data presented by the BCDMS collaboration [26] differs significantly from the deep inelastic muon-proton scattering data produced by the EMC collaboration [27], in the small x region. For example, the measured value of F_2 at an $x-$value of $\simeq 0.1$ is larger in the BCDMS case by $10-15\%$. This new set of data has been incorporated into a new distribution fit by Martin *et al.* [24] and an alternative set of distributions, MRSB, became available. This new set has a up quark distribution which is 10-15% larger in the $x-$region of interest. The dependence of the Born cross-section on the MRSB quark distribution is shown in figure 4.10. Again, the cross-section ratio MRSB/MRS1 is plotted and the ratio is no larger than 5%. The contribution of the gluon to the higher-order contribution has a compensating effect since the MRSB gluon is some 10-15% smaller than the MRS1 gluon in this range. This dilutes the enhancement in the Born term.

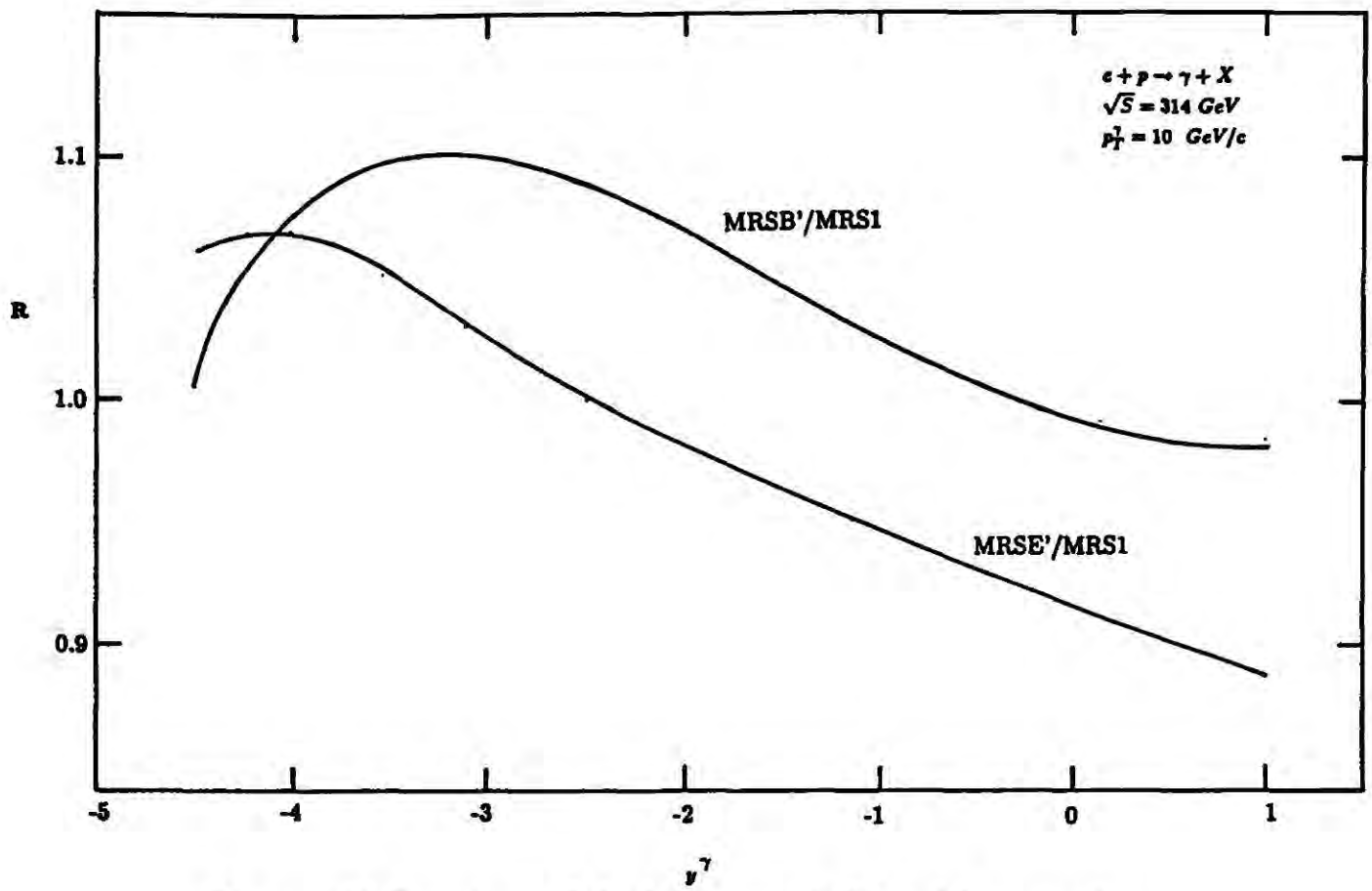

Figure 4.12 Dependence of the fully corrected differential cross-section $d\sigma/dp_T^\gamma dy^\gamma$ as a function of rapidity on the choice of parton distributions MRS1, MRS2 and MRS3 normalized to the MRS1 prediction. The p_T^γ is fixed at 10 GeV/c.

To further probe the sensitivity of this process to the structure functions, a similar study was made of its rapidity distributions at a fixed p_T^γ of 10 GeV/c. For the cross-section ratios MRSB'/MRS1 and MRSE'/MRS1 (see figure 4.12) the sensitivity increases to about 10% and this is because a rapidity distribution probes the x parameter-space. The MRS2/MRS1 ratio is in the region of 20% and this process might be suitable to distinguish between parameter sets that contain hard and soft gluons.

The total cross-section, as a function of p_T^{min}, is given by

$$\sigma(p_T^{min}) = \int_{p_T^{min}}^{\sqrt{S}/2} \frac{d\sigma}{dp_T^\gamma} dp_T^\gamma.$$

This cross-section is presented in figure 4.13, calculated with the MRS1 set of structure functions.

The asymmetry in the photon rapidity distributions reflects the asymmetry in the kinematics at HERA. In figure 4.14, the differential cross-section $d\sigma/dp_T^\gamma dy^\gamma$

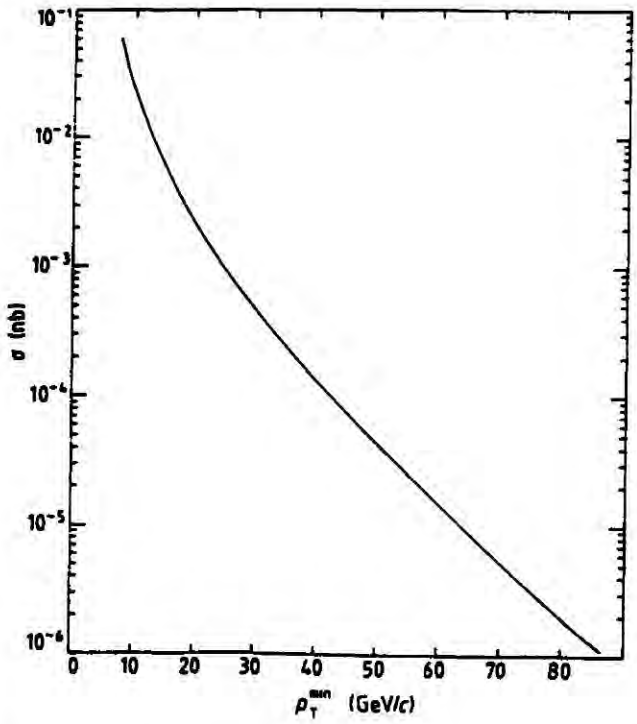

Figure 4.13 The fully corrected 'total' (ie. p_T^γ integrated) cross-section σ againt p_T^{min} using the MRS1 parton distributions.

is presented for the three values of $p_T^\gamma = 10, 20, 30\ GeV/c$ as a function of the rapidity of the final-state photon. The plots at each p_T^γ are the rapidity spectra of the fully-corrected cross-section up to $O(\alpha_s)$, again with the MRS1 parton distributions. As p_T^γ increases, the rapidity distribution shifts to more negative values and this reflects the fact that more and more of the subprocess energy enters through the quarks, rather than the initial-state photon.

4.6 Conclusions

It is clear that the process $e + p \rightarrow \gamma + X$ should be observable at HERA up to $p_T^\gamma = 50\ GeV/c$. At $p_T^\gamma = 20\ GeV/c$ a rate of 40 events per year per GeV/c may be expected while the p_T^γ–integrated cross-section indicates 220 events per year above $p_T^{min} = 20\ GeV/c$ and 1 event per year above $p_T^{min} = 65\ GeV/c$.

The hope that this process will be a 'clean' probe for the proton structure function was unfounded. As can be seen in figure 4.11, four recent sets of parton distributions give cross-sections which differ by less than 10% in the relevant

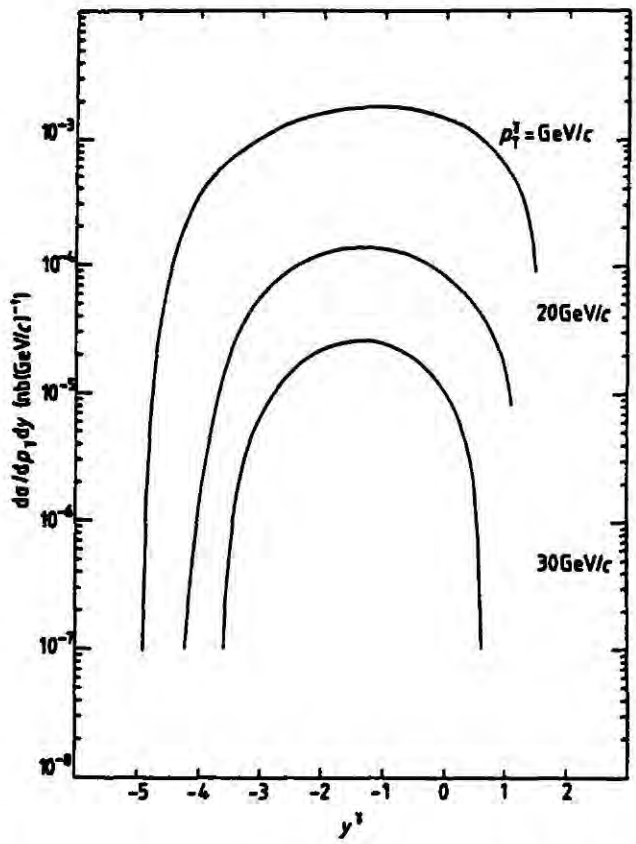

Figure 4.14 Rapidity spectra $d\sigma/dp_T^\gamma dy^\gamma$ against y^γ for p_T^γ =10, 20, 30 *GeV/c*. Note that negative rapidity corresponds to the incoming proton direction.

kinematic region. This similarity in cross-section is due to a partial cancellation between the leading-order quark and leading log, next-to-leading-order gluon contributions.

The $O(\alpha_s)$ corrections seem well under control since the corrections to the Born term are approximately 40% at $p_T^\gamma = 20$ GeV/c and then reduce to $\sim 20\%$ at $p_T^\gamma = 40$ GeV/c. This makes optimisation (with respect to the QCD scales) of the higher-order cross-sections less urgent. In any case, it will first be necessary to obtain the cross-section to $O(\alpha_s^2)$.

The weak dependence of the process under investigation on the structure functions means that cross-sections will have to be measurable to within 5% for it to be used as a probe of the proton. This translates into the need for $\pm 1\%$ resolution in the momentum of the final-state photon if it has a transverse momentum of ~ 30 *GeV/c*. It will be extremely difficult to achieve this level of statistical and systematic precision in the experiments.

However, the photoproduction of prompt photons will provide an accurate 'benchmark' for the standard model, and any significant deviation from the above

theoretical predictions could signal new physics.

REFERENCES

1. J.D. Bjorken and E.A. Paschos: Phys. Rev. **185**, (1970) 1975.
2. M. Fontannaz, *et al.*: Z. Phys. **C6** (1980) 241,357.
3. K. Iguchi and A. Niegawa: Z. Phys. **C9** (1981) 135; T.S. Tu and C.M. Wu: Nucl. Phys. **B156** (1979) 493.
4. D.W. Duke and J.F. Owens: Phys. Rev. **D26** (1982) 1600; erratum: Phys. Rev. **D28** (1983) 1227.
5. P. Aurenche, *et al.*: Z. Phys. **C24** (1984) 309.
6. J.J. Engelen: Proceedings of the Workshop Experimentation at HERA, June 9-11, 1983.
7. B.L. Combridge: Nucl. Phys. **B174** (1980) 243.
8. E. Witten: Nucl. Phys. **B120** (1977) 189.
9. W.A. Bardeen and A.J. Buras: Phys. Rev. **D19** (1979) 166; Erratum: Phys. Rev. **D21** (1980) 2041.
10. R.J. DeWitt *et al.*: Phys. Rev. **D19** (1979) 2046.
11. M. Gluck and E. Reya: Phys. Rev. **D28** (1983) 2749.
12. I. Antoniadis and G. Grunberg: Nucl. Phys. **B213** (1983) 445.
13. M. Drees and K. Grassie: Z. Phys. **C28** (1985) 451.
14. C.H. Llewellyn-Smith: Phys. Lett. **B79** (1978) 83.
15. A.C. Bawa, M. Krawczyk and W.J. Stirling: In progress.
16. R.K. Ellis, *et al.*: Nucl. Phys. **B173** (1980) 397.
17. M. Fontannaz and D. Schiff: Z. Phys. **C14** (1982) 151.
18. R.K. Ellis *et al.*: Nucl. Phys. **B211** (1983) 106.
19. P.B. Arnold and M Hall Reno: FERMILAB-PUB-88/168-T.
20. L. Beaulieu and C. Kounnas: Nucl. Phys. **B141** (1978) 423.
21. I. Kodaira and T. Uematsu: Nucl. Phys. **B141** (1978) 497.

22. G. Altarelli, *et al.*: Nucl. Phys. **B153** (1978) 521.

23. G. Altarelli, *et al.*: Nucl. Phys. **B160** (1979) 301.

24. A.D. Martin, R.G. Roberts and W.J. Stirling: Phys. Rev. **D37**, 1161 (1988).

25. P. Astbury, *et al.*: Phys. Lett. **B152** (1985) 149.

26. A.C. Benvenuti, *et al.*: Phys. Lett. **B223** (1989) 485.

27. J.J. Aubert *et al.*: Nucl. Phys. **B259** (1985) 189.

5. Production of Charged Higgs Bosons at the TEVATRON and SSC

5.1 Introduction

The standard model of electroweak interactions has been highly successful in reproducing all experimentally observed electroweak phenomena. However, the standard model is incomplete in certain respects. At the present time the mechanism of symmetry breaking remains a source of great speculation. The discovery of the intermediate vector bosons, the $W^{\pm}$ and Z^0, at the CERN collider confirmed that the electroweak interactions are based on an $SU(2) \times U(1)$ gauge symmetry, which is spontaneously broken to $U(1)_{EM}$. The discovery of the mechanism via which this spontaneous symmetry breaking occurs is perhaps the most important project in particle theory today.

Several theoretical mechanisms have been proposed for this spontaneous symmetry breaking. The Higgs model is a satisfactory technique for generating masses for the intermediate vector bosons and for the fermions, but the mechanism is not very well understood. One feature of the Higgs mechanism is that it guarantees the renormalizability of the electroweak theory. The most economic version of the standard model has just one complex doublet with four scalar degrees of freedom associated with the four generators of the $SU(2) \times U(1)$ gauge group. On breaking the symmetry three of these degrees of freedom are absorbed as longitudinal components by the $W^{\pm}$ and Z^0 and are responsible for the generation of the intermediate vector boson (and the fermion) masses, while the remaining degree of freedom corresponds to a physical, electrically-neutral, CP-even scalar; commonly referred to as the Higgs boson of the minimal standard model. There appear to be no theoretical constraints on the number of Higgs doublets that may be introduced into the electroweak Lagrangian and this study concerns the phenomenological implications that result from an increase in the Higgs sector from one to two complex doublets. Both in minimal and nonminimal models, the Higgs bosons are elementary. To fully understand spontaneous symmetry breaking via the Higgs mechanism it will be essential to perform a

complete spectroscopy of the Higgs sector, both neutral and charged. More complicated mechanisms have been proposed for spontaneous symmetry breaking, such as technicolor and compositeness, both of which contain composite Higgs scalars.

If the electroweak theory is embedded in a larger gauge group (which will be characterised by a large energy scale, for example the Planck scale) then due to radiative corrections, the Higgs scalar (or scalars) will attain a mass of the order of this large scale. In order to prevent this in the minimal model one is forced to 'fine-tune' the parameters of the theory at every order of perturbation theory in an unnatural way. The minimal standard model, which has only a single, neutral Higgs boson, cannot lift the 'fine tuning' problem. Theoretically, supersymmetry (SUSY) may be invoked to overcome this problem. A minimal SUSY model, which can deal with the hierarchy problem, contains a complex two-doublet Higgs sector. It is for this reason that the nonminimal model that has attracted most attention is the two-doublet Higgs extension of the standard model which has a Higgs sector that is the same as that of the minimal SUSY model.

The extension of the minimal Higgs sector is a reasonable theoretical step since there is a total lack of any experimental verification for this minimal model. This step increases the size of the Higgs sector and gives rise to Higgs bosons that are charged, thus increasing the scope of the experimental searches. The existence or nonexistence of these charged and neutral Higgses may be determined in the next generation of colliders. For light Higgs bosons (that is, $m_H \leq M_Z/2$) a complete search will be possible at the existing colliders; at the SLC and at LEP. At LEP II, this search capability will be extended to $m_H \simeq 85GeV$. Several recent studies have been made concerning the theory and phenomenology of these charged Higgs bosons [1-4]. This study is a part of a larger study [5] that extends this phenomenology, particularly at the TEVATRON and the SSC. This is a report of charged Higgs production accompanied by a brief study of the QCD-background and the background due to the production of $W^{\pm}$. In section 5.2, a theoretical overview is presented of the non-minimal standard model and the Feynman rules that govern the production and decay of the charged Higgs

bosons. In section 5.3, the zeroth- and first-order contributions to the process $A+B \to H^{\pm}+X$, (A,B protons or antiprotons) is considered. This is followed in section 5.4 by a discussion of the matrix element calculations of the subprocess $g+b \to t+b+\bar{t}$ where the final-state $b+\bar{t}$ are produced through an intermediate W or H. This calculation is done with the formalism of the Kleiss-Stirling spinor techniques [7]. Some details of the numerical calculations are given.

5.2 The Nonminimal Higgs Model

As far as is known, there is no compelling reason to believe that the minimal Higgs model is the correct one. It is therefore important to investigate the implications of nonminimal Higgs models, both as an extension of the standard model and as a minimal version of supersymmetry. The two-doublet version of the standard model is of phenomenological interest because it increases the number of observable Higgses. However, it does this with only a small increase in the number of arbitrary parameters. Theoretically, it is satisfying because it maintains the constraint on the value of the ρ parameter, which has been found experimentally to be very close to 1. In addition, it does not introduce any flavour-changing neutral currents, as long as the Higgs-fermion couplings are chosen appropriately.

Consider a model in which the Higgs sector comprises 2 doublets, ϕ_1 and ϕ_2, both complex $SU(2)_L$ scalar fields. These may be written as

$$\begin{aligned} \phi_1 &= \begin{pmatrix} \phi_1^{0*} \\ -\phi_1^- \end{pmatrix} \\ \phi_2 &= \begin{pmatrix} \phi_2^+ \\ \phi_2^0 \end{pmatrix}. \end{aligned} \tag{5.1}$$

In supersymmetry, this two doublet structure is required to cancel out the additional contributions to the triangle anomalies due to the Higgsino. In (5.1) the ϕ_1 doublet ($Y=-1$) generates masses for the $T_{3L}=-1/2$ quarks and charged leptons, while the ϕ_2 doublet ($Y=+1$) gives mass to the $T_{3L}=+1/2$ quarks.

In this case the most general Higgs potential that leads to the spontaneous symmetry breaking of $SU(2)_L \times U(1)_Y$ to $U(1)_{EM}$ is [4]

$$\begin{aligned} V(\phi_1,\phi_2) =& \lambda_1(\phi_1^\dagger\phi_1 - v_1^2)^2 + \lambda_2(\phi_2^\dagger\phi_2 - v_2^2)^2 \\ &+ \lambda_3[(\phi_1^\dagger\phi_1 - v_1^2) + (\phi_2^\dagger\phi_2 - v_2^2)] \\ &+ \lambda_4[(\phi_1^\dagger\phi_1)(\phi_2^\dagger\phi_2) - (\phi_1^\dagger\phi_2)(\phi_2^\dagger\phi_1)] \\ &+ \lambda_5[Re(\phi_1^\dagger\phi_2) - v_1v_2]^2 \\ &+ \lambda_6[Im(\phi_1^\dagger\phi_2)]^2. \end{aligned} \tag{5.2}$$

In (5.2) the λ_i are real parameters and for a large range of them the correct form of electroweak breaking is guaranteed. The $v_{1,2}$ are the vacuum expectation values of the neutral members of the doublets. The sum of the squares of vacuum expectation values is defined by

$$m_W^2 = g^2(v_1^2 + v_2^2),$$

where g is the weak coupling. If the λ_i are non-negative, the minimum of the potential is given by

$$< \phi_1 >= \begin{pmatrix} 0 \\ v_1 \end{pmatrix}, \quad < \phi_2 >= \begin{pmatrix} 0 \\ v_2 \end{pmatrix}. \tag{5.3}$$

The required constraints on the λ_i are less stringent than mentioned above. To produce the necessary symmetry breakdown, the requirement that has to be met is that all the Higgs bosons should have positive mass-squared.

As usual the degeneracy of the ground state after spontaneous symmetry breaking produces additional scalars, called the Goldstone bosons. (In this model there are eight degrees of freedom; three Goldstone bosons and five Higgses.) In the charged sector they are given by

$$G^\pm = \phi_1^\pm \cos\beta + \phi_2^\pm \sin\beta, \tag{5.4}$$

where β is given by

$$\tan\beta = v_2/v_1. \tag{5.5}$$

The physical, charged Higgs states that are orthogonal to these Goldstone bosons

are

$$H^{\pm} = -\phi_1^{\pm} \sin\beta + \phi_2^{\pm} \cos\beta. \tag{5.6}$$

The masses of these physical, charged Higgs bosons are $m_{H^{\pm}}^2 = \lambda_4(v_1^2 + v_2^2)$. In this treatment [4] CP-invariance of the Higgs sector is assumed and this leads to a decoupling of the imaginary and real parts in the neutral scalar field. The neutral, Goldstone boson in the imaginary, CP-odd sector, is given by

$$G^0 = \sqrt{2}(Im\,\phi_1^0 \cos\beta + Im\,\phi_2^0 \sin\beta)$$

and the orthogonal, neutral Higgs boson is

$$A^0 = \sqrt{2}(-Im\,\phi_1^0 \sin\beta + Im\,\phi_2^0 \cos\beta), \tag{5.7}$$

and $m_{A^0}^2 = \lambda_6(v_1^2 + v_2^2)$. This CP-odd scalar is usually called a pseudoscalar. On the other hand, the real part of the Higgs sector (that is, the CP-even part) contains two physical scalars which are neutral. They mix through the squared mass matrix

$$M = \begin{pmatrix} 4v_1^2(\lambda_1 + \lambda_3) + v_2^2\lambda_5 & (4\lambda_3 + \lambda_5)v_1v_2 \\ (4\lambda_3 + \lambda_5)v_1v_2 & 4v_2^2(\lambda_2 + \lambda_3) + v_1^2\lambda_5 \end{pmatrix}. \tag{5.8}$$

The corresponding orthogonal physical states are

$$\begin{aligned} H^0 &= \sqrt{2}[(Re\phi_1^0 - v_1)\cos\alpha + (Re\phi_2^0 - v_2)\sin\alpha] + \\ h_0 &= \sqrt{2}[-(Re\,\phi_1^0 - v_1)\sin\alpha + (Re\,\phi_2^0 - v_2)\cos\alpha]. \end{aligned} \tag{5.9}$$

α is defined below. The corresponding masses are given (in terms of the elements of (5.8)) by

$$m_{H^0,h^0}^2 = 1/2\left[M_{11} + M_{22} \pm \sqrt{(M_{11} - M_{22})^2 + 4M_{12}^2}\right].$$

Note that this expression sets the following condition

$$m_{H^0} \geq m_{h^0}.$$

The mixing angle α used in (5.9) is given by

$$\begin{aligned}\sin 2\alpha &= \frac{2M_{12}}{\sqrt{(M_{11}-M_{22})^2+4M_{12}^2}} \\ \cos 2\alpha &= \frac{M_{11}-M_{22}}{\sqrt{(M_{11}-M_{22})^2+4M_{12}^2}},\end{aligned} \tag{5.10}$$

where M_{ij} are the elements of the matrix M of (5.8), and so ultimately α depends on the parameters in the Higgs potential.

Instead of the single free parameter of the standard minimal Higgs model, the mass of the scalar boson, this nonminimal model contains six free parameters. Without loss of generality these may be chosen to be the four Higgs masses, the ratio of the vacuum expectation values β and the mixing angle α. α and β are chosen such that

$$\begin{aligned}-\pi/2 \le \alpha \le 0 \\ 0 \le \beta \le \pi/2.\end{aligned} \tag{5.11}$$

These parameters are independent of each other in the most general model. However, in minimal supersymmetry the number of free parameters reduces to three; for example, $m_W, v_2/v_1$ and $m_{H^\pm}$.

The relevant terms in the Lagrangian for the different couplings are presented now [6]:

Term for VHH interactions

$$\begin{aligned}\mathcal{L}_{VHH} = &-\frac{ig}{2}W_\mu^+ H^- \overleftrightarrow{\partial^\mu}\left[H^0\sin(\alpha-\beta)+h^0\cos(\alpha-\beta)+iA^0\right]+h.c. \\ &-\frac{ig}{2\cos\theta_W}Z_\mu\Big[iA^0\overleftrightarrow{\partial^\mu}\left(H^0\sin(\alpha-\beta)+h^0\cos(\alpha-\beta)\right) \\ &-(2x_W-1)H^-\overleftrightarrow{\partial^\mu}H^+\Big]\end{aligned} \tag{5.12}$$

where as usual

$$X\overleftrightarrow{\partial^\mu}Y = X(\partial^\mu Y) - Y(\partial^\mu X)$$

The ZH_iH_i vertices are excluded by Bose statistics.

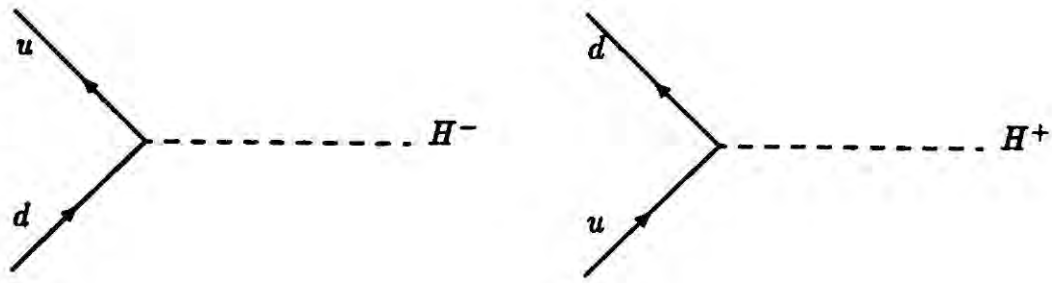

Figure 5.1 The quark-charged Higgs vertices.

Term for VVH interactions

$$\mathcal{L}_{VVH} = \left(g m_W W_\mu^+ W^{-\mu} + \frac{g m_Z}{2\cos\theta_W} Z_\mu Z^\mu \right) \left[H^0 \cos(\beta-\alpha) + h^0 \sin(\beta-\alpha) \right]. \tag{5.13}$$

The elusive nature of the Higgs bosons is due in large part to their extremely weak coupling to light fermions. Therefore, the interesting processes to consider phenomenologically will be those which contain the W^+ZH^- vertex. Unfortunately, as can be seen from (5.13), at tree level the W^+ZH^- vertex is absent in an $SU(2) \times U(1)$ model [1].

Term for Higgs boson interactions with u and d type quarks

This term is given by

$$\begin{aligned}
\mathcal{L}_{udH} = &- \frac{g m_u}{2 m_W \sin\beta} \left[u\bar{u}\left(H^0 \sin\alpha + h^0 \cos\alpha\right) - i\cos\beta \bar{u}\gamma_5 u A^0 \right] \\
&- \frac{g m_d}{2 m_W \cos\beta} \left[d\bar{d}\left(H^0 \cos\alpha - h^0 \sin\alpha\right) - i\sin\beta \bar{d}\gamma_5 d A^0 \right] \\
&+ \frac{g}{2\sqrt{2} m_W} \Big[H^+ V_{ud} \bar{u} \left[(m_d \tan\beta + m_u \cot\beta) \right. \\
&\qquad \left. + (m_d \tan\beta - m_u \cot\beta)\gamma_5 \right] d + h.c. \Big].
\end{aligned} \tag{5.14}$$

For the Higgs boson couplings to the leptons, (u,d) are replaced by (ν, e^-).

In figure 5.1 the vertices between up and down type quarks and the charged Higgs bosons are shown. From the relevant terms in the electroweak Lagrangian

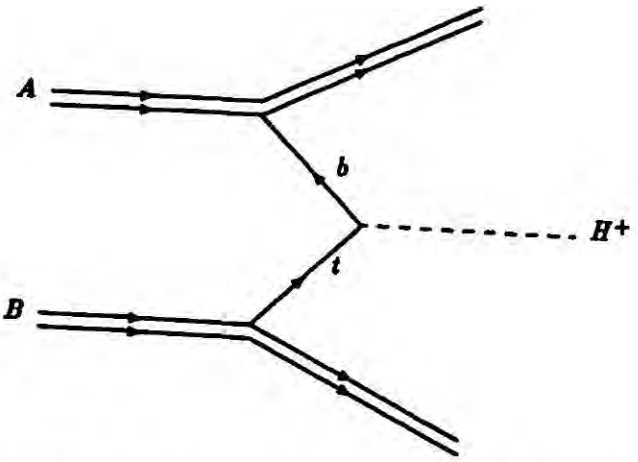

Figure 5.2 The hadronic production of charged Higgs bosons.

above, the vertex (a) may be written as

$$\frac{ig}{2\sqrt{2}m_W}\left[(m_d\tan\beta + m_u\cot\beta) + (m_d\tan\beta - m_u\cot\beta)\gamma_5\right] \qquad (5.15)$$

and the vertex (b) as

$$\frac{ig}{2\sqrt{2}m_W}\left[(m_d\tan\beta + m_u\cot\beta) - (m_d\tan\beta - m_u\cot\beta)\gamma_5\right]. \qquad (5.16)$$

5.3 THE PROCESS $A + B \to H^{\pm} + X$

The fully inclusive production of charged Higgs scalars at hadron colliders has been studied before [1],[8] and in this study the formalism of [8] is followed. The process is shown schematically in figure 5.2, where A, B are protons and X stands for anything. As usual, the most general expression for a hadronic cross-section is given by

$$\sigma(A+B \to H^{\pm}) = \sum_{a,b} G_{a/A}(x_a, Q^2) \otimes \hat{\sigma}_{ab \to H^{\pm}} \otimes G_{b/B}(x_b, Q^2) + (A \leftrightarrow B), \quad (5.17)$$

where a, b are partons and the G's are distribution functions of the partons within hadrons. $\hat{\sigma}$ is the hard process cross-section.

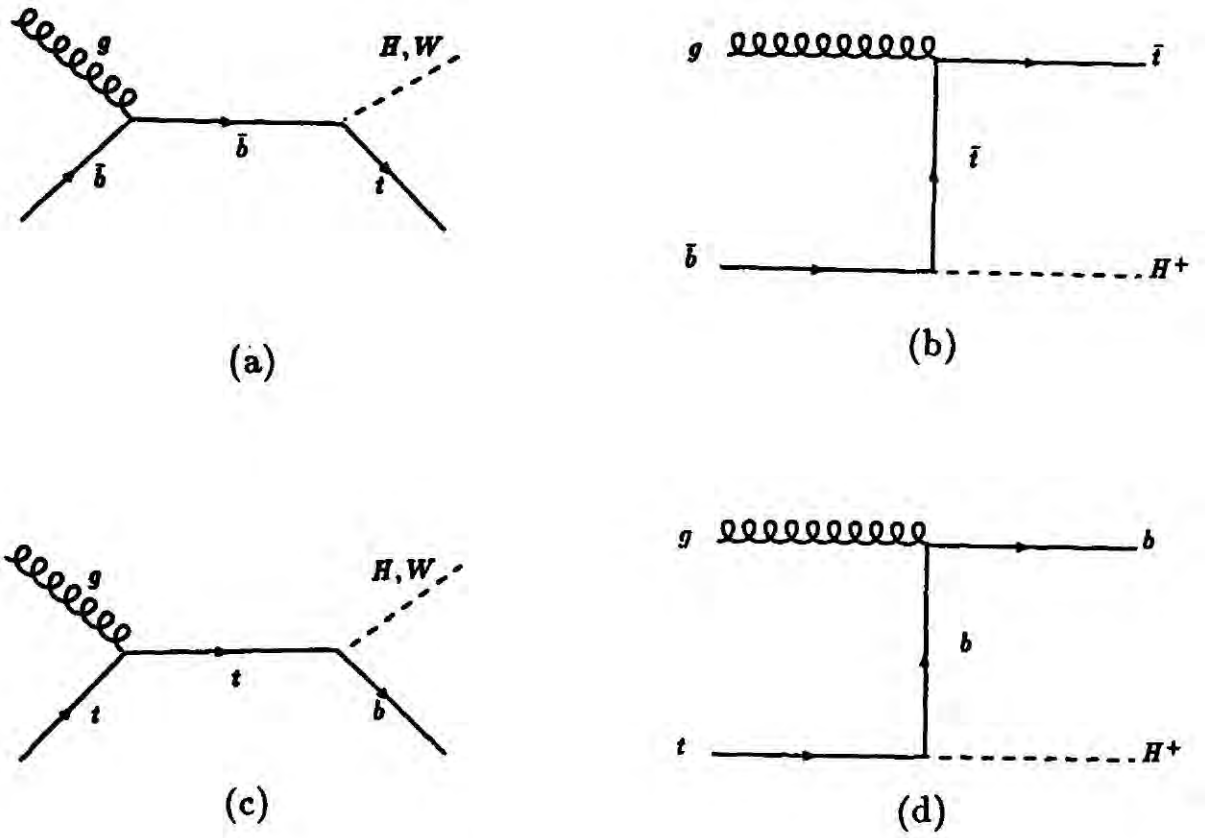

Figure 5.3 The next-to-leading order contributions to charged Higgs production in hadronic interactions.

To the zeroth-order in α_s the dominant diagrams that contribute to the fully inclusive cross-section are those of the type shown in figure 5.1 with $d \to b$ and $u \to t$ and the couplings for these vertices are

$$\begin{aligned} &\frac{ig}{2\sqrt{2}m_W}[m_b \tan\beta(1-\gamma_5) + m_t \cot\beta(1+\gamma_5)] \times |V_{tb}| \\ &\frac{ig}{2\sqrt{2}m_W}[m_b \tan\beta(1-\gamma_5) - m_t \cot\beta(1+\gamma_5)] \times |V_{tb}|. \end{aligned} \tag{5.18}$$

It is clear that the hard-process cross-section depends on the mass-squared of the fermions in the couplings and hence the dominant couplings of the charged Higgs in the minimally extended standard model are those to the top and bottom quarks.

In figure 5.3 the four diagrams that contribute to the next order in α_s are shown and these are the subprocesses

$$\begin{aligned} g + \bar{b} &\to \bar{t} + H^+ \\ t + g &\to b + H^+. \end{aligned} \tag{5.19}$$

For a heavy top quark, the parton distribution function is, to a good approximation, derived from the $O(\alpha_s)$ splitting of the gluon. This is true until the full QCD evolution of the parton distribution functions occurs at an energy which is at least some orders of magnitude larger than the mass of the top quark. This qualitative argument makes the parton distribution function of the top quark an $O(\alpha_s)$ effect and so, of the four diagrams in figure 5.3, diagrams (c) and (d) may be neglected in practice. Here the bottom quark is considered to be a light quark.

However, on examining the leading-order diagram, $t + \bar{b} \rightarrow H^+$, and the next-to-leading-order diagram (b) it is clear that the latter contributes partially to the distribution function of the top quark and this leads to double counting since the top quark distribution function is included in the zeroth-order diagram [8]. This double counting occurs when the intermediate top quark line is on mass-shell and collinear with the gluon, that is, when it is a real parton. This condition also gives rise to mass singularities. In perturbative QCD calculations these mass-singularities must be removed from the hard-process cross-section.

Following Olness and Tung [8], it will be shown that the removal of these mass singularities leads to the removal of the double counting. The full partonic cross-section is given by

$$\sigma(a + b \rightarrow H^{\pm}) = \sum_{c,d} G_{c/a}(x_a, Q^2) \otimes \hat{\sigma}_{cd \rightarrow H^{\pm}} \otimes G_{d/b}(x_b, Q^2), \qquad (5.20)$$

where $G_{c/a}$ is the distribution of the c-parton in the a-parton. $\hat{\sigma}$ for these partonic processes may be obtained by inverting (5.20) since the calculation of $\sigma(ab \rightarrow H)$ and G's are well established in perturbative QCD (assuming that the factorisation theorem holds order by order).

To zeroth-order in α_s, the c-parton distribution within an a-parton is simply given by

$$G^{(0)}_{c/a}(x, Q^2) = \delta^c_a \delta(x - 1).$$

Then (5.20) gives the relation

$$\hat{\sigma}^{(0)}(ab \rightarrow H) = \sigma^{(0)}(ab \rightarrow H). \qquad (5.21)$$

To $O(\alpha_s)$ the expression for the partonic cross-section is a combination of the

zeroth- and first-order hard processes, given by

$$\sigma^{(1)}(ab \to H) = \hat{\sigma}^{(1)}(ab \to H) + G^{(1)}_{d/b} \otimes \hat{\sigma}^{(0)}(ad \to H) + G^{(1)}_{c/a} \otimes \hat{\sigma}^{(0)}(cb \to H). \tag{5.22}$$

The superscripts in these expressions refer to the order in α_s. Inverting this equation and substituting (5.21) the following expression for the hard process may be obtained

$$\hat{\sigma}^{(1)}(ab \to H) = \sigma^{(1)}(ab \to H) - \sigma^{(0)}(ad \to H) \otimes G^{(1)}_{d/b} - \sigma^{(0)}(cb \to H) \otimes G^{(1)}_{c/a}. \tag{5.23}$$

The terms on the right of (5.23) are all calculable and this gives $\hat{\sigma}^{(1)}$.

Now if the process $\hat{\sigma}(g\bar{b} \to H^+)$ is considered, in terms of (5.23) the expression for the hard-process cross-section may be written as

$$\hat{\sigma}^{(1)}(g\bar{b} \to H) = \sigma^{(1)}(g\bar{b} \to H) - G^{(1)}_{t/g} \otimes \sigma^{(0)}(t\bar{b} \to H), \tag{5.24}$$

since there is no zeroth-order contribution from a gluon in the initial state. Olness and Tung [8] call the second term in (5.24) the *subtraction* term and it is clear that this term has exactly the right form for the collinear configuration that leads to the double counting (see figure 5.3). However, the removal of this term also leads to the removal of the mass-singularity in the $O(\alpha_s)$ cross-section in the limit that the mass of the top quark goes to zero.

To obtain a complete expression for the production of a positively-charged Higgs scalar from a collision of a hadron A and a hadron B, (5.21) and (5.24) are substituted into (5.17). This gives

$$\begin{aligned} \sigma(AB \to H^+) = &\left[G_{t/A} - G'_{t/A}\right] \otimes \sigma^{(0)}(t\bar{b} \to H^+) \otimes G_{\bar{b}/B} + \\ &G_{\bar{b}/B} \otimes \sigma^{(1)}(g\bar{b} \to H^+) \otimes G_{g/A} + (A \leftrightarrow B), \end{aligned} \tag{5.25}$$

where $G'_{t/A} = G_{g/A} \otimes G^{(1)}_{t/g}$. (5.25) shows clearly that the subtraction term removes from the zeroth-order term the potential source of double counting.

The matrix element squared for the process $t + \bar{b} \rightarrow H^+$ is obtained readily. If the momentum of the top quark is p_1 and that of the bottom quark p_2 (in figure 5.2), then the Feynman diagram gives

$$\mathcal{M}_{t\bar{b}}(p_i, \lambda_i) = \bar{v}(p_2, \lambda_2)\Big[\frac{ig}{2\sqrt{2}m_W}(C_1 + C_2\gamma_5)\Big]u(p_1, \lambda_1), \tag{5.26}$$

where C_1 and C_2 may be obtained from (5.18). Then

$$\begin{aligned}\overline{\mathcal{M}^2_{t\bar{b}}}(p_i) &= \frac{g^2}{8m_W^2}\sum_{\lambda=1}^{2}\big[\bar{v}(p_2, \lambda_2) \\ &\qquad (C_1 + C_2\gamma_5)u(p_1, \lambda_1)\bar{u}(p_1, \lambda_1)(C_1 - C_2\gamma_5)v(p_2, \lambda_2)\big] \\ &= \frac{g^2}{8m_W^2}Tr\left[\not{p}_2(\not{p}_1 + m_t)(C_1 + C_2\gamma_5)^2\right] \\ &= \frac{g^2}{8m_W^2}\left[4p_2.p_1(C_1^2 + C_2^2)\right]\end{aligned} \tag{5.27}$$

For this $2 \rightarrow 1$ process,

$$(p_1 + p_2)^2 = m_t^2 + 2p_1.p_2 = m_H^2$$

and so

$$\begin{aligned}\overline{\mathcal{M}^2_{t\bar{b}}}(p_i) &= \frac{g^2}{8m_W^2}\left[2(m_H^2 - m_t^2) \times (C_1^2 + C_2^2)\right] \\ &= \frac{g^2}{8m_W^2}\left[2(m_H^2 - m_t^2) \times 2(m_b^2\tan^2\beta + m_t^2\cot^2\beta)\right],\end{aligned} \tag{5.28}$$

where (5.18) has been used. This expression has to be spin- and colour-averaged and this means multiplying (5.28) by $(4 \times 3)^{-1}$. This expression has been checked by C.S. Kim [5].

The matrix element squared for the associated $2 \rightarrow 1$ $W^{\pm}$ production graph is obtained similarly and the final expression that is used in the computation is

$$\overline{\mathcal{M}^2_{t\bar{b}}}(p_i) = \frac{g^2}{24m_W^2}|V_{tb}|^2\left[(m_W^2 - m_t^2)(m_t^2 + 2m_W^2)\right]. \tag{5.29}$$

As a check, on setting the mass of the top quark to zero this reduces to the

well-known expression for the matrix element squared of the process $q\bar{q}' \rightarrow W^+$

$$\overline{\mathcal{M}^2_{t\bar{b}}}(p_i) = \frac{g^2}{12} \times m_W^2.$$

For the associated $2 \rightarrow 2$ processes, the matrix elements of C.S. Kim *et al.* [16] were used.

For the total cross-section with n-particles in the final-state the number of integrals is given by $3n-4$ plus 2 (for the convolution integrals over the momentum fractions of the partons within the protons). Hence, in the $2 \rightarrow 1$ case there is just one integral and a suitable one is the rapidity of the final-state particle. The upper and lower limits of this integral are given by

$$-\ln\frac{\sqrt{S}}{m_H} \leq y_H \leq \ln\frac{\sqrt{S}}{m_H}$$

and x_a and x_b are determined as

$$\begin{aligned} x_a &= \frac{m_H}{\sqrt{S}} e^{y_H} \\ x_b &= \frac{m_H}{\sqrt{S}} e^{-y_H}. \end{aligned} \tag{5.30}$$

For the $2 \rightarrow 2$ case, the kinematics will be the same as that discussed in the $2 \rightarrow 2$ case in chapters 1 and 3.

The expression for the total cross-section is, usual,

$$\sigma^{tot}_{AB}(s,...) = \int dx_a dx_b G_{a/A}(x_a,Q^2) G_{b/B}(x_b,Q^2) \hat{\sigma}_{ab}(\hat{s},....) + (A \leftrightarrow B). \tag{5.31}$$

The parton distribution functions that were used in this study are those of W-K. Tung *et al.* [9]. They have been generated by a QCD evolution program with variable heavy top-quark mass. The usual parton distribution functions (the so-called fixed-parameter sets) [10-12] are not suitable as they do not take into consideration the variable heavy top-quark mass. The evolution of the distributions with six quark flavours (all of which come into play above their thresholds) is performed with the scheme of Collins and W-K. Tung [13] and the top-quark mass that enters these evolution equations enters the hard partonic cross-sections as well. The initial parton distributions at $Q_0 = 2.25$ GeV are those of the EHLQ set 1 [12] with $\lambda_{QCD} = 200$ MeV.

The W vector boson and the charged Higgs have identical decay modes and so it is important to estimate the size of this background. The branching fraction of the charged Higgs to anything is dependent on the mass of the top quark, the mass of the scalar itself and on the parameter $\tan\beta$. If the top quark is lighter than the charged Higgs then the scalar will decay dominantly via $H^+ \rightarrow t\bar{b}$, suppressing all other decay modes. In this case the dominant background is the QCD one. However, if this particular decay mode is kinematically forbidden, then the decays that matter are those via $H^+ \rightarrow c\bar{s}$ and $H^+ \rightarrow \tau^+\nu$. Setting $\tan\beta = 1$, these branching fractions are given by Barger and Phillips [3] as 64% and 31%, respectively. The $\tan\beta$ dependence of these branching fractions is demonstrated by the fact that if $\tan\beta = 2$ then these numbers change to 13% and 82%, respectively. (These branching fractions have been checked in the present study). The corresponding branching fractions for the W bosons to the $\tau\nu$ decay mode is of the order of 10% and so it is clear that if the mass of the top quark is greater than the mass of the charged Higgs boson, then the $\tau\nu$ decay mode may offer a possibility for the detection of these charged scalars above the W background, even if the W production cross-section is greater than the corresponding cross-section for the Higgs scalrs.

For the set of curves presented in figure 5.4 the factorisation and renormalisation scales are both set at m_t in the case of the calculation of the Higgs boson production, and at m_W in the case of W^+ production. In addition, the arbitrary parameter $\tan\beta$, defined in (5.5) has to be stipulated. The total cross-sections for positively-charged Higgs and W^+ production are presented for different values of m_H and m_t and for $\tan\beta = 1$ at $\sqrt{S} = 40$ TeV. The total cross-section is of the order of tens of picobarns. It is clear from the curves in figure 5.4 that for this value of $\tan\beta$, the background to fully inclusive charged Higgs production from W production at the SSC may be too large except at very large values of m_t; that is, for $m_t > 160$ GeV the signal of a light Higgs ($m_H \simeq 40\ GeV/c^2$) will be observable. However, the cross-sections are very dependent on the parameter $\tan\beta$ and in figure 5.5, the identical calculation is performed with $\tan\beta = 0.1$. It is clear that in this case the region of visibility of the charged Higgs above the W background improves dramatically.

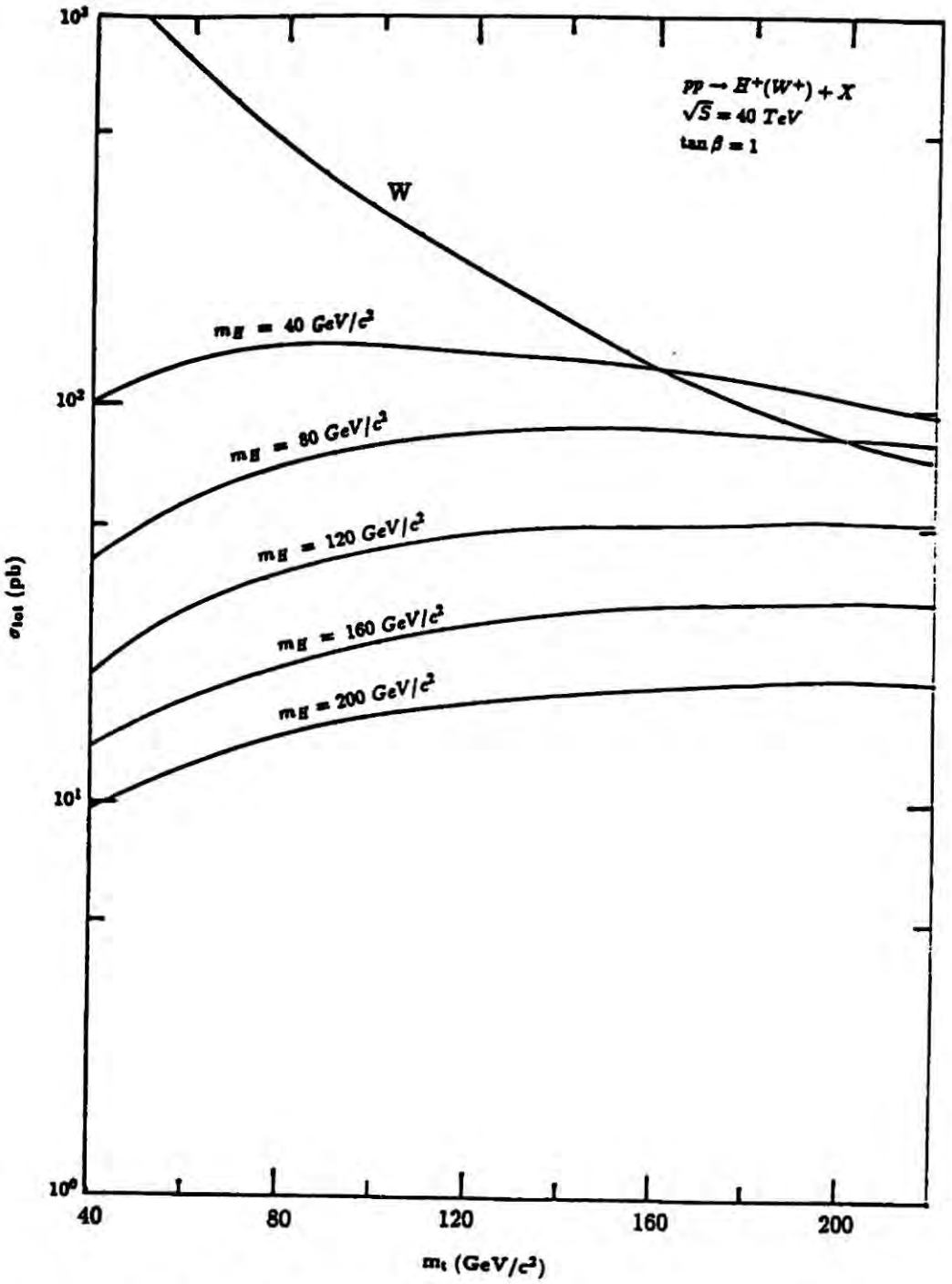

Figure 5.4 The total cross-section for charged Higgs production at the SSC.

The calculation is repeated for the energies at which the Tevatron is operating and with $\tan\beta = 1$. The results are presented in figure 5.6 and it is clear that the window of visibility is wider in this case. This interesting feature arises through the particular nature of the Higgs-fermion couplings. These are proportional to the mass of the fermions, while the corresponding W-fermion couplings are independent of these masses. For a light Higgs, $m_H = 40\ GeV/c^2$ the signal is certainly above the W background if $m_t > 95\ GeV/c^2$. However, the W production cross-section is larger than that of the charged Higgs with $m_H = 80\ GeV/c^2$ if the mass of the top quark is less than $170\ GeV/c^2$. A more complete

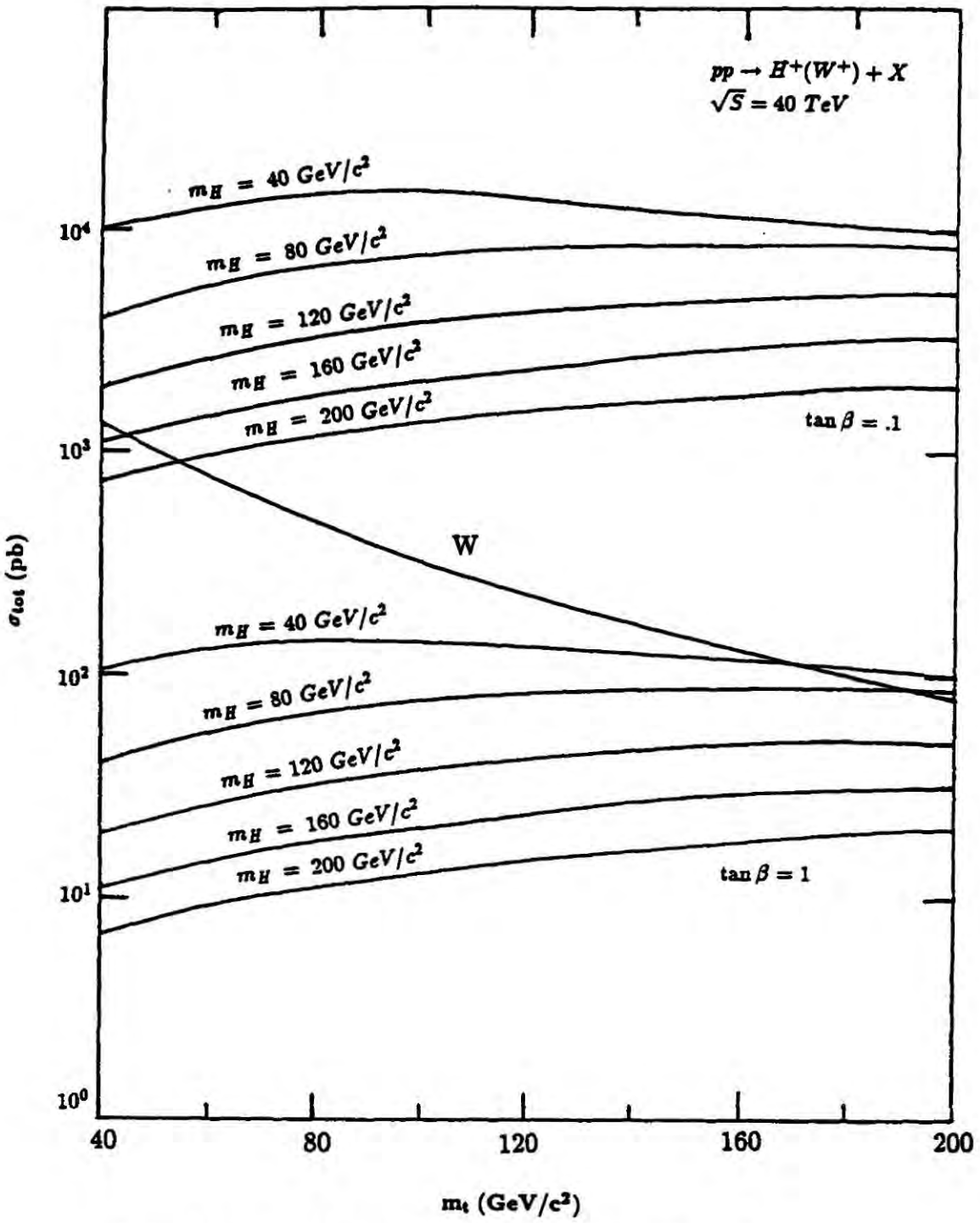

Figure 5.5 Charged Higgs production at the SSC with $\tan\beta = 0.1$

study of this is being prepared [5].

This scenario seems bleak, since the discovery of the charged Higgs bosons at the colliders depends on the observation of the decay modes of the scalars above the backgrounds due to, firstly W decay and then secondly and more seriously, by the usual QCD processes. However, it is important to recall that the dominant decay mode of the scalar boson is $H^+ \to t + \bar{b}$ and since the Higgs couplings in this decay mode go as the mass of the top quark, this presents some incentive to explore these $2 \to 3$ processes. This is done in section 5.4.

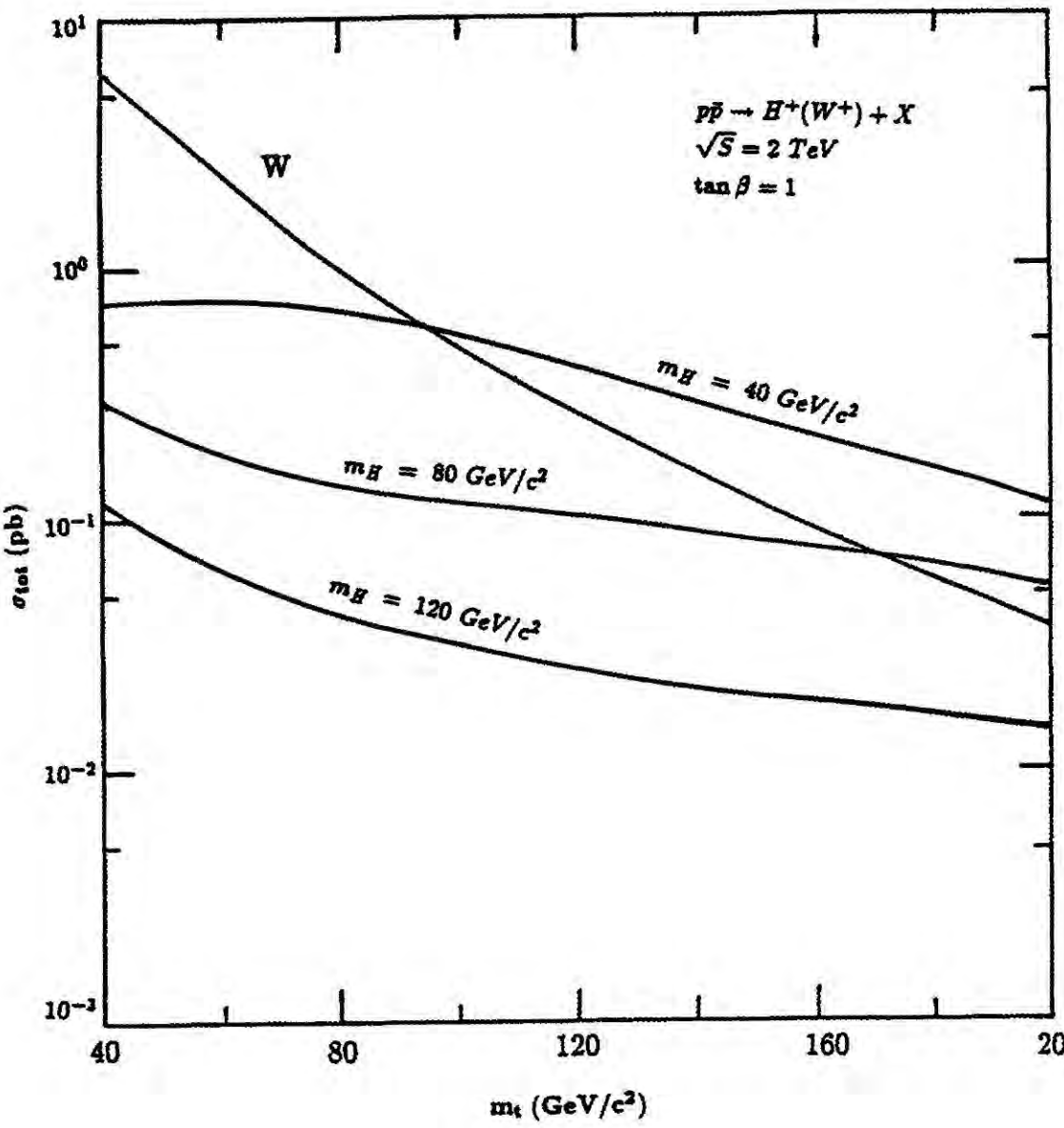

Figure 5.6 Total cross-section for charged Higgs production at the Tevatron.

5.4 The generic process: $g + \bar{b} \rightarrow \bar{t} + t + \bar{b}$

This generic process is studied here, and is shown in figure 5.7, where in the final state $\bar{t} + b$ may be produced via the decay of the positively-charged Higgs scalars, H^+, or via the competing W^+ decay (*eg.* see figure 5.8) or the usual background QCD processes (see figure 5.9). The matrix elements for the QCD processes were calculated by Ellis and Sexton [15]. The other two processes are discussed below.

However, it must be made clear that the dominant production mode at the SSC is the gluon-gluon one. This process (shown in figure 5.10), for single charged

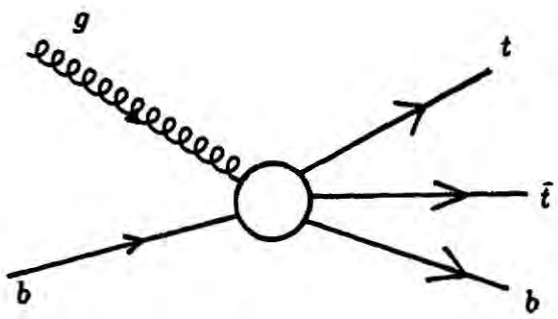

Figure 5.7 The generic process: $g + \bar{b} \rightarrow \bar{t} + t + \bar{b}$.

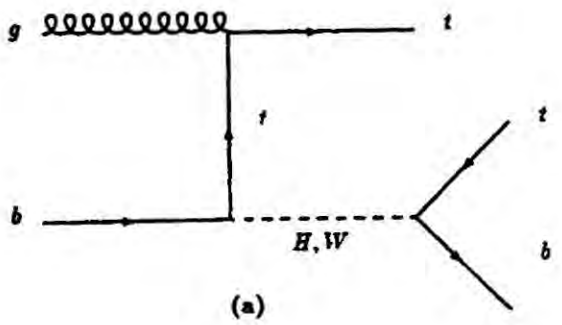

Figure 5.8 The process: $g + \bar{b} \rightarrow \bar{t} + t + \bar{b}$ with an intermediate charged Higgs or $W^{\pm}$.

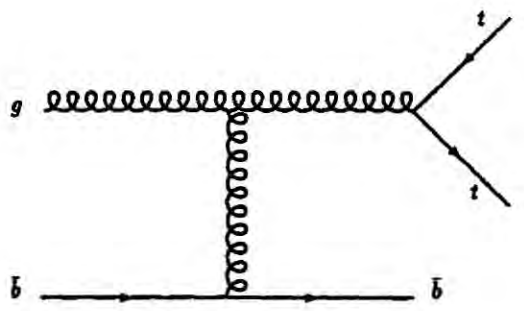

Figure 5.9 The competing QCD processes: $g + \bar{b} \rightarrow \bar{t} + t + \bar{b}$.

Higgs production is,

$$g + g \rightarrow t + \bar{b} + H^{-}$$

It can be efficiently approximated [6] by the internal process

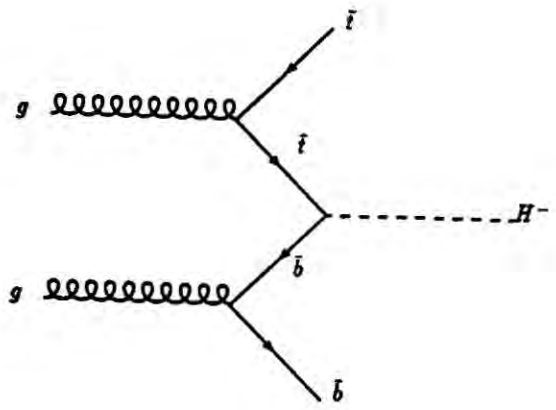

Figure 5.10 The dominant production mode for charged Higgs at the SSC $g + g \rightarrow \bar{t} + b + H^+$.

$$g + b \rightarrow t + H^-$$

where the b quark distribution is, as usual, generated by the Altarelli-Parisi evolution equations. This alternative process is shown in figure 5.8.

Four Feynman diagrams contribute to the process

$$g + b \rightarrow \bar{t} + t + b, \tag{5.32}$$

with an intermediate negatively charged Higgs boson. These diagrams are shown in figure 5.11. In figure 5.11(b) the gluon has momentum q, the incoming b quark has momentum p_1, and the final state t, b and $\bar{t}$ have momenta p_2, p_3 and p_4 respectively.

Then the Feynman diagram in figure 5.11(b) may be written as

$$\begin{aligned}\mathcal{M}_a =& \bar{u}(p_3,\lambda_3)\left[\frac{ig}{2\sqrt{2}m_W}\left(m_b \tan\beta(1-\gamma_5) - m_t \cot\beta(1+\gamma_5)\right)|V_{tb}|\right]u(p_4,\lambda_4) \\ & \times \left[(p_3+p_4)^2 - m_H^2 + im_H\Gamma_H\right]^{-1} \\ & \times \bar{u}(p_2,\lambda_2)\left[\frac{ig}{2\sqrt{2}m_W}\left(m_b \tan\beta(1-\gamma_5) + m_t \cot\beta(1+\gamma_5)|V_{tb}|\right)\right]\frac{i}{\not p_1 + \not q} \\ & \times u(p_1,\lambda_1)\left[-ig_s T^c_{ab}\gamma^\tau\right]\epsilon^c_\tau(q,\lambda_g),\end{aligned} \tag{5.33}$$

Following the prescription of Kleiss and Stirling [7] the polarisation vector

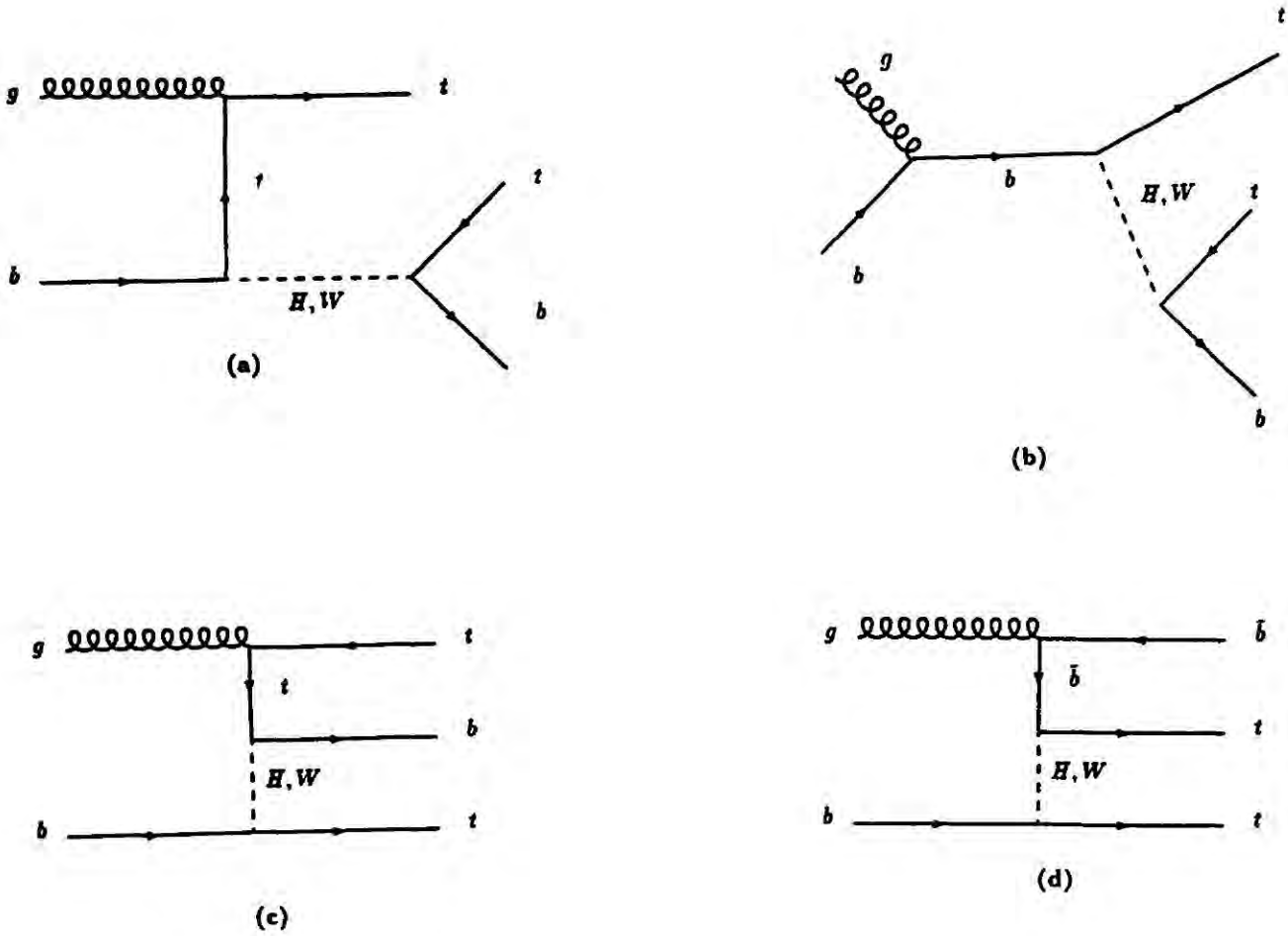

Figure 5.11 The full gauge-invariant set of Feynman diagrams for the process: $g + \bar{b} \rightarrow \bar{t} + t + \bar{b}$.

for the gluon is given by

$$\epsilon_\tau^c(q, \lambda_g) = N \times \bar{u}(q, \lambda_g)\gamma^{\tau c} u(p_0, \lambda_g), \tag{5.34}$$

where the vector p_0 specifies gauge for the gluon and

$$N = [4(q.p_0)]^{-1/2}.$$

p_0^μ can be any light-like vector not collinear to q^μ. The helicity amplitude $\mathcal{M}_a$ is a function of the different momenta and helicities in figure 5.11(a). These polarization vectors correspond to states of definite helicity, denoted by $\epsilon_\pm^\mu$. In addition, since they carry physical, transverse polarizations the calculation of the matrix element squared does not require the introduction of ghost terms to cancel the extra degrees of freedom that enter through unphysical polarization states.

Using the spinor techniques procedure [7] outlined in chapter 2, this Feynman structure is rewritten in terms of the spinor products defined in chapter 2. In

the expression below, the following notation for the spinor products is used:

$$S_{\lambda_i,\lambda_j}(p_i,p_j) = S(i,j,\lambda_i,\lambda_j).$$

The expression expands to

$$\begin{aligned}
\mathcal{M}_a = \sum_{i=1,5} & G_1^H C_1^H D_1^H \Big\{ m_b^2 \tan^2\beta S(3,4,\lambda_3,-1) \\
& \Big\{ \Big[S(2,1,\lambda_2,-1)S(1,6,-1,\lambda_5) + S(2,5,\lambda_2,-1)S(5,6,-1,\lambda_5\Big] S(5,1,\lambda_5,\lambda_1) \\
& + \Big[S(2,1,\lambda_2,-1)S(1,5,-1,-\lambda_5) + S(2,5,\lambda_2,-1)S(5,5,-1,-\lambda_5\Big] S(6,1,-\lambda_5,\lambda_1) \Big\} \\
& + m_b m_t \tan\beta\cot\beta S(3,4,\lambda_3,+1) \\
& \Big\{ \Big[S(2,1,\lambda_2,-1)S(1,6,-1,\lambda_5) + S(2,5,\lambda_2,-1)S(5,6,-1,\lambda_5\Big] S(5,1,\lambda_5,\lambda_1) \\
& + \Big[S(2,1,\lambda_2,-1)S(1,5,-1,-\lambda_5) + S(2,5,\lambda_2,-1)S(5,5,-1,-\lambda_5\Big] S(6,1,-\lambda_5,\lambda_1) \Big\} \\
& + m_t m_b \cot\beta\tan\beta S(3,4,\lambda_3,-1) \\
& \Big\{ \Big[S(2,1,\lambda_2,+1)S(1,6,+1,\lambda_5) + S(2,5,\lambda_2,+1)S(5,6,+1,\lambda_5\Big] S(5,1,\lambda_5,\lambda_1) \\
& + \Big[S(2,1,\lambda_2,+1)S(1,5,+1,-\lambda_5) + S(2,5,\lambda_2,+1)S(5,5,+1,-\lambda_5\Big] S(6,1,-\lambda_5,\lambda_1) \Big\} \\
& + m_t^2 \cot^2\beta S(3,4,\lambda_3,+1) \\
& \Big\{ \Big[S(2,1,\lambda_2,+1)S(1,6,+1,\lambda_5) + S(2,5,\lambda_2,+1)S(5,6,+1,\lambda_5\Big] S(5,1,\lambda_5,\lambda_1) \\
& + \Big[S(2,1,\lambda_2,+1)S(1,5,+1,-\lambda_5) + S(2,5,\lambda_2,+1)S(5,5,+1,-\lambda_5\Big] S(6,1,-\lambda_5,\lambda_1) \Big\} \Big\}
\end{aligned} \tag{5.35}$$

In (5.35) the colour factor, C_1^H, is given by summation/averaging over final/initial colours. In this case this is 12/24. The denominator, D_1^H is given by

$$D_1^H = [(p_3+p_4)^2 - m_H^2 + im_H\Gamma_H]^{-1}[(p_1+q)^2]^{-1}[4p_0.q]^{-1/2},$$

and finally, the couplings and normalisation constants are given by

$$G_1^H = 2ig^2 g_s/2m_H^2.$$

The rest of the diagrams in figure 5.11 are treated in the same fashion. The helicity amplitudes depend on the external momenta and on the helicities of

the internal and external particles. The external quarks are massive and so the conservation of helicity at the vertices is broken. To obtain the final matrix element squared the following procedure is used:

(a) For each set of momenta p_j the value for each of the $\mathcal{M}_i^H(p_j, \lambda_j)$ is calculated for a particular combination of helicities.

(b) These values are then summed over i to obtain an helicity amplitude. i runs over the full set of diagrams in figure 5.11, which is gauge-invariant.

(c) Each helicity amplitude is then squared and summed over all helicity combinations, thus producing the matrix element squared, which has been checked to be independent of the choice of gauge p_0.

The calculation of the diagrams in figure 5.11, with the Higgs bosons replaced by $W^{\pm}$ bosons is performed using the same techniques but with the following changes. The Htb vertex used in (5.33) is replaced by the Wtb vertex

$$-i\frac{g}{2\sqrt{2}}\gamma^{\mu}(1-\gamma_5)|V_{tb}|,$$

where as usual $g = 8m_W^2 G_F/\sqrt{2}$ and the W-boson propagator is given by

$$\frac{-i\left[g_{\mu\nu} + (\xi-1)p_\mu p_\nu/(p^2 - \xi m_W^2)\right]}{p^2 - m_W^2 + im_W\Gamma_W}. \tag{5.36}$$

$\xi = 1$ specifies the Feynman-'t Hooft gauge, while $\xi = 0$ specifies the Landau gauge and it is the latter one that is used in this study. Again, the helicity amplitudes are checked for gauge invariance.

This hadronic cross-section calculation was performed with a Monte-Carlo simulation program. Initially, the phase space configurations were generated with the 'democratic' phase space generator, RAMBO [14]. Although this helped to simplify the program considerably, the method proved to be unsuccessful. The reason for this is that in both sets of diagrams the propagators of the scalar and vector bosons are strongly peaked when the momentum squared of the bosons are close to $m_{W,H}^2$ (see (5.36)). The Monte-Carlo program that was used has the built-in facility to readjust its grid as it progresses from iteration to iteration,

so as to focus on regions which are peaked. This leads to the vast majority of phase space points in the configuration to fall within this strongly-peaked region, making the Monte-Carlo simulation extremely unrealistic and inefficient.

In terms of the momenta specified in figure 5.11(a) the 3-particle phase space integral is

$$\int \frac{d^3p_2}{(2\pi)^3 2E_2}\frac{d^3p_3}{(2\pi)^3 2E_3}\frac{d^3p_4}{(2\pi)^3 2E_4}(2\pi)^4\delta^{(4)}(p_1+q-p_2-p_3-p_4).$$

The integral can be rewritten (as in chapter 2) in terms of an intermediate final-state compound system with an invariant-mass squared of M_{34}^2, energy E_{34} and momentum $P_{34}=p_3+p_4$ as (ignoring constant factors)

$$\begin{aligned}&\int \frac{d^3p_2}{E_2}\delta^{(4)}(p_1+q-p_2-P_{34})\\ &\times\int_{S_0}^{S} dM_{34}^2\int d^4P_{34}\delta(P_{34}^2-M_{34}^2)\\ &\times\int\frac{d^3p_3}{E_3}\int\frac{d^3p_4}{E_4}\delta^{(4)}(p_3+q+p_4-P_{34}).\end{aligned}\tag{5.37}$$

It is easily be shown that (5.37) may finally be written as

$$\begin{aligned}&\int\frac{d^3p_2}{E_2}\int\frac{d^3P_{34}}{E_34}\delta^{(4)}(p_1+q-p_2-P_{34})\times\int_{S_0}^{S}dM_{34}^2\\ &\times\int\frac{d^3p_3}{E_3}\int\frac{d^3p_4}{E_4}\delta^{(4)}(p_3+q+p_4-P_{34}).\end{aligned}\tag{5.38}$$

And the integral over M_{34}^2 can be performed analytically. The rest of the phase space is performed analogously to that performed in chapter 2 and this works very well.

As has been mentioned previously, the production of a final state consisting of a top quark, a bottom quark and an anti-top quark can proceed via three routes. The first is the pure QCD path (see figure 5.9) and this is a very threatening

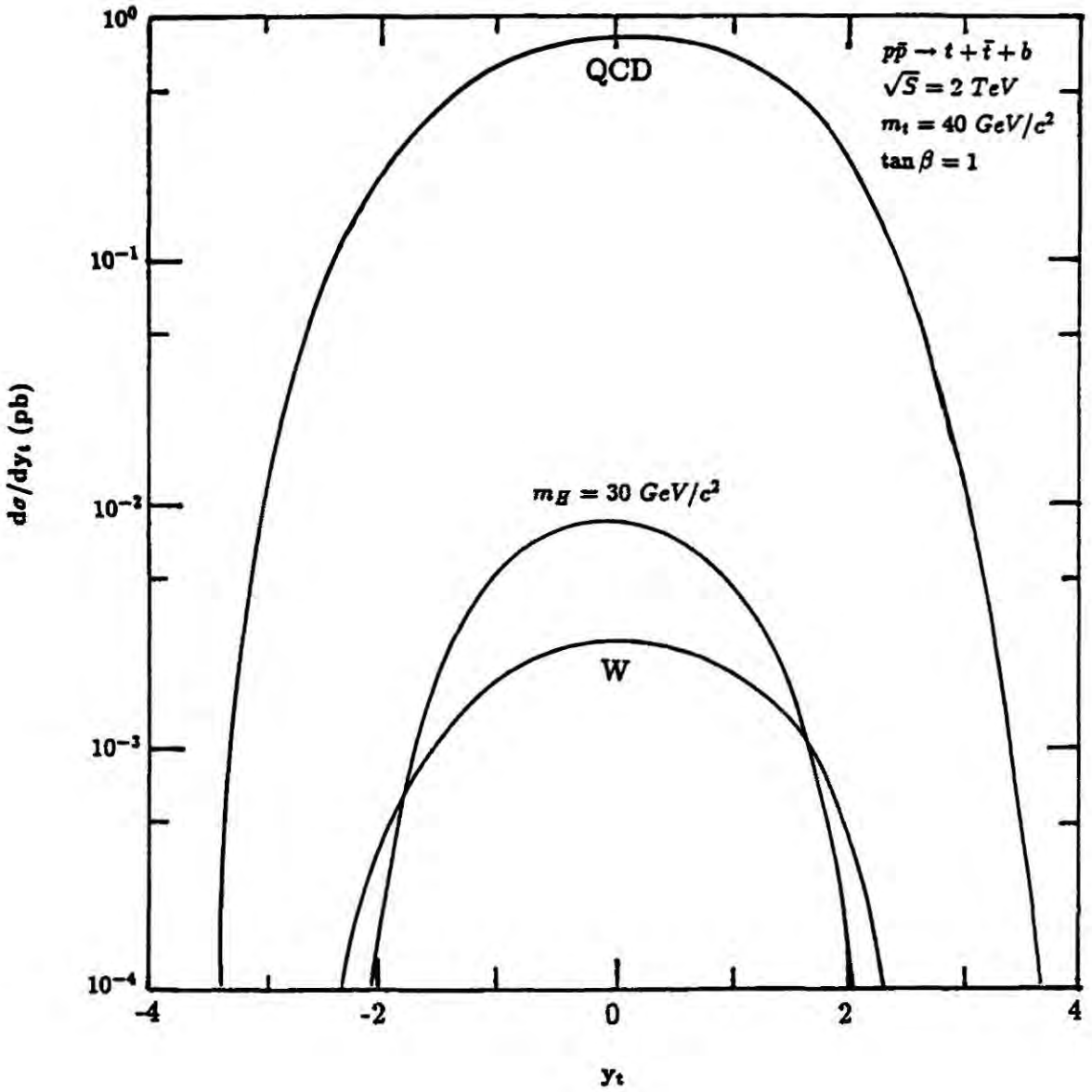

Figure 5.12 The rapidity distribution of the the three competing processes; QCD, intermediate charged Higgs and intermediate W bosons. $\sqrt{S} =$ 2000 GeV and $m_t = 40\ GeV/c^2$

background in the hadron colliders. Some indication is presented of the size of this background.

The parton distributions that have been used in this study are those of Eichten *et al.*[12], the EHLQ set 1. This next-to-leading order set has $\Lambda_{QCD} =$ 200 MeV and is stable to $x \sim 10^{-4}$. As in the previous calculation the factorisation scale has been set at m_t for all the calculations, except for the weak vector boson case. In these calculations minimal cuts were employed to protect the infrared singularities that appear and $\tan\beta$ is set at 1.

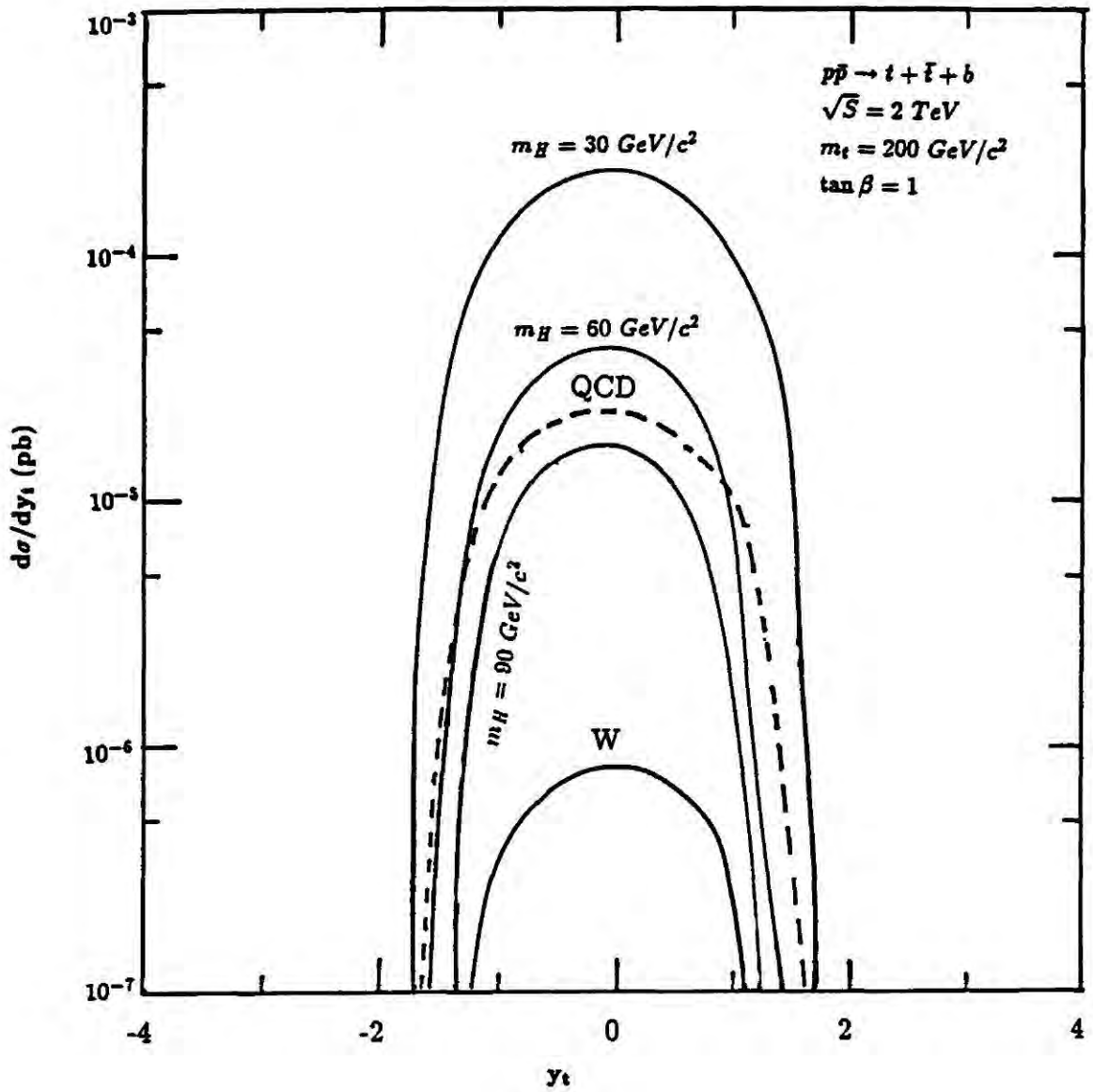

Figure 5.13 The rapidity distribution of the the three competing processes; QCD, intermediate charged Higgs and intermediate W bosons. $\sqrt{S} =$ 2000 GeV and $m_t = 200\ GeV/c^2$

In this project several distributions were studied to search for suitable windows within which the charged Higgs cross-sections might be visible above the backgrounds. The most suitable one is the rapidity distribution of the top quark with momentum p_2. The case for $\sqrt{S} = 2000\ GeV$ and $m_t = 40$ and 200 GeV/c^2 are presented in figures 5.12 and 5.13, respectively. In figure 5.12, it is clear that the charged Higgs signal for m_H is observable above the W cross-section, but is completely swamped by the QCD process. This situation worsens in the case $m_H > 40\ GeV/c^2$ However, in figure 5.13 it is clear that for the case of a heavy

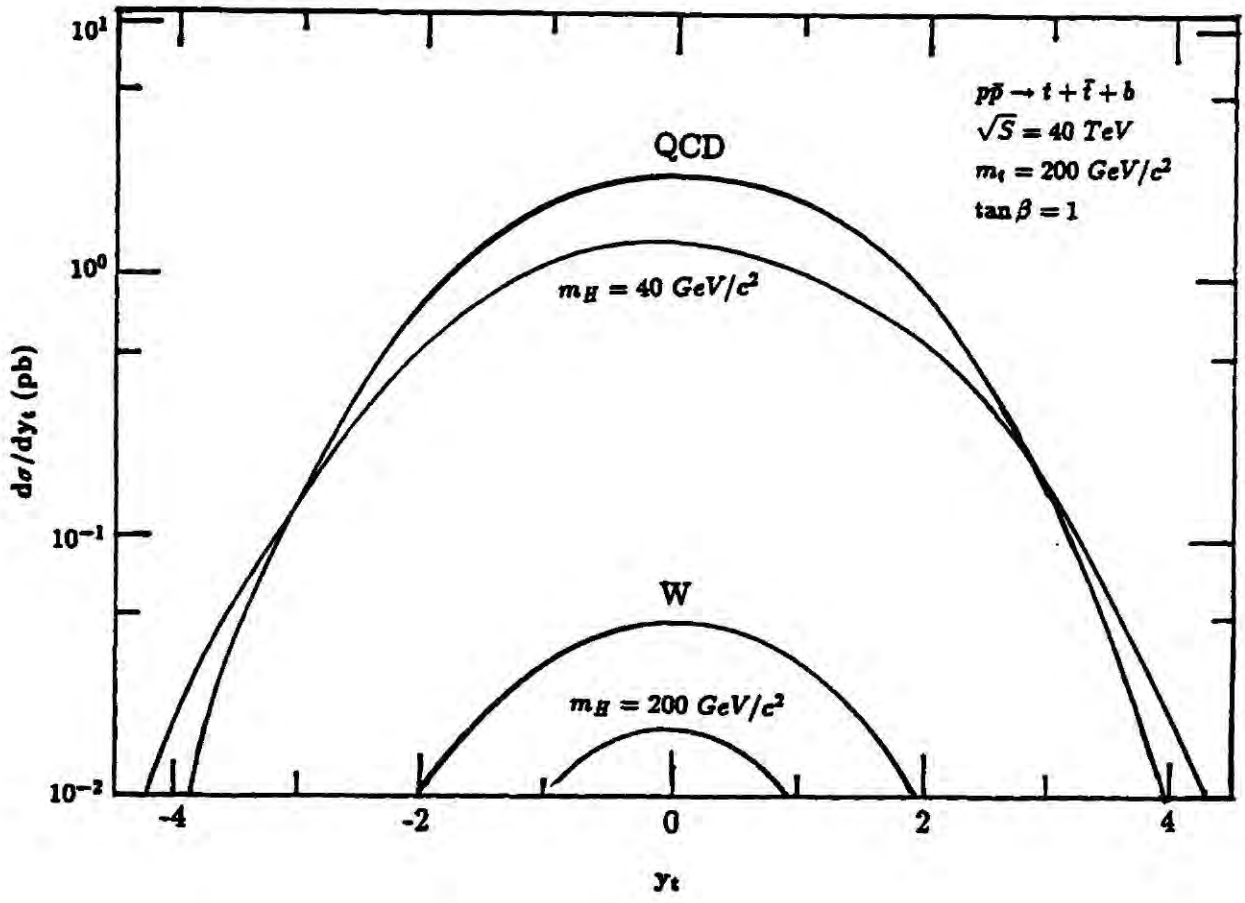

Figure 5.14 The rapidity distribution of the the three competing processes; QCD, intermediate charged Higgs and intermediate W bosons. $\sqrt{S} = 40\ TeV$ and $m_t = 200\ GeV/c^2$

top quark the situation improves dramatically. The charged Higgs signal is larger than the QCD background for $m_H < 70\ GeV/c^2$.

As has been mentioned earlier, this calculation has been repeated for for the SSC, at $\sqrt{S} = 40\ TeV$. In this case, (see figure 5.14) the QCD cross-section dominates the charged Higgs signal for ($m_H > 40\ GeV/c^2$) even for $m_t = 200\ TeV$.

Again, to draw any conclusions a study must be made of the decay widths and braching fractions of the top quarks in the final-state. This part of the study

is incomplete and will be presented in [5].

5.5 Conclusions.

The total charged Higgs fully-inclusive cross-sections have been calculated and compared with the production cross-section of the charged intermediate vector bosons. The cross-section is extremely model-sensitive, depending strongly on the value of the parameter $\tan\beta$. Not very much may be said about the possibility of observation. For the particular value of $\tan\beta$ chosen it is clear that for a light Higgs and heavy top quark, the fully-inclusive charged Higgs cross-section at hadronic colliders competes with that of the W bosons. For the Tevatron, there appears to be a window available for the observation of a light charged Higgs, though this window is small; and if detector details are considered, it may be insufficient. However, conclusions may only be drawn after these production cross-sections are folded in with the relevant branching fractions. It appears that in the case where $m_t > m_H$, the decay mode $W, H \to \tau\nu$ is a very hopeful one.

The second part of the calculation prepares the way for some exploration of the production of the charged Higgs and their subsequent decay to fermions ($H^+ \to t + \bar{b}$ or $H^+ \to \bar{\tau} + \nu_\tau$ or any other) both for real and virtual Higgses. In the results presented in the last section it is clear that, except for a small window for light Higgses at the Tevatron, the QCD background is overwhelming. A complete study of this is presently under way [5].

REFERENCES

1. J.F. Gunion, G.L. Kane and J. Wudka, Nucl. Phys. **B299** (1988) 231.
2. J.F. Gunion and H.E. Haber, Nucl. Phys. **B278** (1986) 449.
3. J.F. Gunion, *et al.*, Nucl. Phys. **B294** (1987) 621; Y.S. Tsai, SLAC-PUB-5003, July 1989; V. Barger and R.J.N. Phillips, MAD/PH/484, April 1989; V. Barger and R.J.N. Phillips, MAD/PH/497, May 1989; C-C Chen, CTP-TAMU-12/89, February 1989.
4. H.E. Haber, SCIPP-89/18, April, 1989.
5. A.C. Bawa, C.S. Kim and A.D. Martin, in preparation.
6. V. Barger and R.J.N. Phillips, Collider Physics, Addison-Wesley (1987).
7. R. Kleiss and W.J. Stirling, Phys. Lett. **B179** (1986) 159.
8. F.I. Olness and Wu-Ki Tung, Nucl. Phys. **B308** (1988) 813.
9. Wu-Ki Tung, *et al.*, FERMILAB-CONF-89/26.
10. A.D. Martin, R.G. Roberts and W.J. Stirling, Phys. Rev. **D37** (1988) 1161.
11. D.W. Duke and J.F. Owens, Phys. Rev. **D30** (1984) 49.
12. E. Eichten *et al.*, Rev. Mod. Phys. **56** (1984) 579.
13. J. Collins and Wu-Ki Tung, Nucl. Phys. **B278** (1986) 934.
14. R. Kleiss, W.J. Stirling and S.D. Ellis, Comput. Phys. Commun. **40** (1986) 359.
15. R.K. Ellis and J.C. Sexton, Nucl. Phys. **B282** (1987) 642.
16. E.L. Berger, F.Halzen, C.S. Kim and S. Willenbrok, Phys. Rev. **D40** (1989) 83.